Alaska Department of Transportation & Public Facilities
Alaska University Transportation Center

Seasonally Frozen Soil Effects on the Seismic Performance of Highway Bridges

Prepared By:
J. Leroy Hulsey, Jacob E. Horzdovsky, and Duane Davis
Institute of Northern Engineering, University of Alaska Fairbanks

Zhaohui Joey Yang and Qiang Li
School of Engineering, University of Alaska Anchorage

December 2011

Prepared For:

Alaska University Transportation Center
Duckering Building Room 245
P.O. Box 755900
Fairbanks, AK 99775-5900

Alaska Department of Transportation
Research, Development, and Technology Transfer
2301 Peger Road
Fairbanks, AK 99709-5399

INE/AUTC 12.06

FHWA-AK-RD-10-02

REPORT DOCUMENTATION PAGE

Form approved OMB No.

1. AGENCY USE ONLY (LEAVE BLANK) FHWA-AK-RD-10-02	2. REPORT DATE December 2011	3. REPORT TYPE AND DATES COVERED Final (7/15/2007-6/30/2011)

4. TITLE AND SUBTITLE

Seasonally Frozen Soil Effects on the Seismic Performance of Highway Bridges

5. FUNDING NUMBERS

T2-07-15

AUTC #107014

DTRT06-G-0011

G00003238-239252-12072

G00004542-591098-68069

6. AUTHOR(S)

J. Leroy Hulsey, Jacob E. Horzdovsky, Duane Davis, Zhaohui Joey Yang, Qiang Li

7. PERFORMING ORGANIZATION NAME(S) AND ADDRESS(ES)
Alaska University Transportation Center
P.O. Box 755900
Fairbanks, AK 99775-5900

8. PERFORMING ORGANIZATION REPORT NUMBER

INE/AUTC 12.06

9. SPONSORING/MONITORING AGENCY NAME(S) AND ADDRESS(ES)
Alaska Department of Transportation and Public Facilities
Research, Development, and Technology Transfer
2301 Peger Road
Fairbanks, AK 99709-5399

10. SPONSORING/MONITORING AGENCY REPORT NUMBER

FHWA-AK-RD-10-02

11. SUPPLENMENTARY NOTES

12a. DISTRIBUTION / AVAILABILITY STATEMENT

12b. DISTRIBUTION CODE

13. ABSTRACT (Maximum 200 words)

Permafrost degradation in regions of high seismic activity increases the potential for soil liquefaction, which can be a serious threat to transportation and utility infrastructure, as many professionals observed during the November 2002 Denali Earthquake (magnitude Mw 7.9). This project conducted laboratory studies to investigate the liquefaction resistance of frozen and seasonally frozen ground. Researchers examined how soil liquefaction is influenced by freeze-thaw cycles throughout the year, and how liquefaction is influenced by temperature distribution in degrading permafrost. The results of this study will help establish criteria for liquefaction susceptibility in melting permafrost and soils that regularly undergo freeze-thaw cycles.

14- KEYWORDS:

15. NUMBER OF PAGES

16. PRICE CODE

N/A

17. SECURITY CLASSIFICATION OF REPORT Unclassified	18. SECURITY CLASSIFICATION OF THIS PAGE Unclassified	19. SECURITY CLASSIFICATION OF ABSTRACT Unclassified	20. LIMITATION OF ABSTRACT N/A

NSN 7540-01-280-5500

STANDARD FORM 298 (Rev. 2-98)
Prescribed by ANSI Std. 239-18 298-1

Notice

Quality Assurance Statement

Author's Disclaimer

SI* (MODERN METRIC) CONVERSION FACTORS

APPROXIMATE CONVERSIONS TO SI UNITS

Symbol	When You Know	Multiply By	To Find	Symbol
LENGTH				
in	inches	25.4	millimeters	mm
ft	feet	0.305	meters	m
yd	yards	0.914	meters	m
mi	miles	1.61	kilometers	km
AREA				
in^2	square inches	645.2	square millimeters	mm^2
ft^2	square feet	0.093	square meters	m^2
yd^2	square yard	0.836	square meters	m^2
ac	acres	0.405	hectares	ha
mi^2	square miles	2.59	square kilometers	km^2
VOLUME				
fl oz	fluid ounces	29.57	milliliters	mL
gal	gallons	3.785	liters	L
ft^3	cubic feet	0.028	cubic meters	m^3
yd^3	cubic yards	0.765	cubic meters	m^3
NOTE: volumes greater than 1000 L shall be shown in m^3				
MASS				
oz	ounces	28.35	grams	g
lb	pounds	0.454	kilograms	kg
T	short tons (2000 lb)	0.907	megagrams (or "metric ton")	Mg (or "t")
TEMPERATURE (exact degrees)				
°F	Fahrenheit	5 (F-32)/9 or (F-32)/1.8	Celsius	°C
ILLUMINATION				
fc	foot-candles	10.76	lux	lx
fl	foot-Lamberts	3.426	candela/m^2	cd/m^2
FORCE and PRESSURE or STRESS				
lbf	poundforce	4.45	newtons	N
lbf/in^2	poundforce per square inch	6.89	kilopascals	kPa

APPROXIMATE CONVERSIONS FROM SI UNITS

Symbol	When You Know	Multiply By	To Find	Symbol
LENGTH				
mm	millimeters	0.039	inches	in
m	meters	3.28	feet	ft
m	meters	1.09	yards	yd
km	kilometers	0.621	miles	mi
AREA				
mm^2	square millimeters	0.0016	square inches	in^2
m^2	square meters	10.764	square feet	ft^2
m^2	square meters	1.195	square yards	yd^2
ha	hectares	2.47	acres	ac
km^2	square kilometers	0.386	square miles	mi^2
VOLUME				
mL	milliliters	0.034	fluid ounces	fl oz
L	liters	0.264	gallons	gal
m^3	cubic meters	35.314	cubic feet	ft^3
m^3	cubic meters	1.307	cubic yards	yd^3
MASS				
g	grams	0.035	ounces	oz
kg	kilograms	2.202	pounds	lb
Mg (or "t")	megagrams (or "metric ton")	1.103	short tons (2000 lb)	T
TEMPERATURE (exact degrees)				
°C	Celsius	1.8C+32	Fahrenheit	°F
ILLUMINATION				
lx	lux	0.0929	foot-candles	fc
cd/m^2	candela/m^2	0.2919	foot-Lamberts	fl
FORCE and PRESSURE or STRESS				
N	newtons	0.225	poundforce	lbf
kPa	kilopascals	0.145	poundforce per square inch	lbf/in^2

*SI is the symbol for the International System of Units. Appropriate rounding should be made to comply with Section 4 of ASTM E380.
(Revised March 2003)

Table of Contents

List of Figures

List of Tables

Acknowledgments

This research was performed under AUTC Project #107014 by the Department of Civil Engineering, University of Alaska Fairbanks, and the Department of Civil Engineering, University of Alaska Anchorage. This project was jointly funded by the Alaska University Transportation Center and the State of Alaska Department of Transportation and Public Facilities.

Dr. J. Leroy Hulsey, Professor of Civil Engineering, University of Alaska Fairbanks, was the principal investigator (PI). Dr. Zhaohui Yang, Associate Professor of Civil Engineering, University of Alaska Anchorage, was the Co-PI. Dr. Feng Xiong, former Assistant Professor of Civil Engineering, University of Alaska Anchorage, now Professor, Sichuan University, China, contributed to this project in its early stage. Messrs. Jacob Horazdovsky and Duane Davis, former graduate students of the University of Alaska Fairbanks, and Messrs. Qiang Li, Gang Xu, and Ruel Binonwangan, former graduate students of the University of Alaska Anchorage, worked as Research Assistants on this project. Mr. Elmer E. Marx, Bridge Engineer, Bridge Section, and Mr. Clint Adler, Chief, Research Development and Technology Transfer, both with the State of Alaska Department of Transportation and Public Facilities, and Mr. Billy G. Connor, Director of the Alaska University Transportation Center, among others, have provided invaluable technical advice.

Abstract

Evidence has shown that seasonally frozen soil significantly affects the seismic response of bridges. In this project, a comprehensive study of the effects of seasonally frozen soil on a highway bridge is carried out in order to provide recommendations on how to plan for these effects in the seismic design of highway bridges in cold regions. This project consists of two field experiments: monitoring of a bridge during seismic events and large deformation experiments of test piles embedded in frozen soils. A bridge in Anchorage was instrumented to monitor its seismic performance and assess the impact of seasonally frozen soil on the overall performance of the bridge. Two test piles were constructed and tested to failure in both summer and winter conditions to assess the effects of seasonally frozen soils on the lateral performance of single piles. Finite element models were created for the bridge and test piles by using the OpenSees simulation platform to analyze seasonally frozen soil impact.

We found that the transverse first modal frequency of the bridge increases about 200% for frozen conditions versus thawed. Simplified design parameters based on the equivalent cantilever approach, including depth of fixity, depth-to-maximum bending moment, and length of plastic hinge, were identified based on pile test data, and recommendations were made for soil profiles with varying seasonally frozen soil depth. In addition, frozen silt *p*-*y* values were back-calculated by using the lateral response data obtained from the pile test, and recommendations were made for constructing a *p*-*y* curve for frozen silt. Recommended simplified design parameters for the equivalent cantilever approach and the frozen silt *p*-*y* curve provide tools for pile foundation design when seasonally frozen soil–pile interaction in a seismic event must be considered.

Summary of Findings

Based on this comprehensive study, the following major conclusions or recommendations are made:

1. The deepest frost penetration at the bridge site occurs around the end of March and reaches about 5 feet.
2. Frost penetration estimation, using the modified Berggren formula, agrees well with field observations. The modified Berggren formula with calibrated parameters can be used to predict frost depth for the bridge site when field measurement is not available.
3. Modal frequency increases with frost penetration. Specifically, when the site is unfrozen, the first transverse modal frequency is 2.5 Hz. As the frost thickness remains around 4 feet, the modal frequency oscillates around 7.5 Hz, representing a 200% increase. This indicates that the bridge is substantially stiffer when frozen than when unfrozen.
4. The three-dimensional FE model of the bridge captures the measured dynamic response of the bridge in terms of the first transverse modal frequency and shape in various thickness of frozen ground. This model is suitable for predicting fundamental frequency in extreme conditions (e.g., when the frost depth reaches 6 feet or more).
5. We found that, for this study, single-pile test data correlated well with a 7.8-foot frost depth for establishing design parameters, using the depth-of-fixity approach. As part of this comparison, depth-to-maximum moment, depth of fixity, and analytical plastic hinge length were evaluated.
6. Where piles are embedded in Alaska silts, we recommend when designing for frozen conditions that a depth of 8-foot of frozen soil be used for the depth-of-fixity approach.
7. We found by back-calculation the *p*-*y* values of frozen silts based on the experimental data obtained from the Fairbanks lateral pile test program.
8. We propose *a p*-*y* curve based on back-calculated *p*-*y* values. Comparison of pile behavior predicted by using the proposed *p*-*y* curve agrees well with field test results obtained from Fairbanks and Canada, and can be used for the analysis of laterally loaded piles embedded in frozen silt in design practices.

CHAPTER 1. INTRODUCTION

1.1 Background

In March of 1964, Alaska experienced one of the largest earthquakes in recorded history. Much damage occurred because of an earthquake-generated a tsunami and soil liquefaction that resulted from ground shaking. Some bridge damage appeared to be directly attributable to the occurrence of frozen ground and ice formation. Recent research in Alaska and Iowa has identified the significance of frozen ground effects on seismic response of bridge foundations and has validated the need for design guidelines that consider the effects of seasonally frozen ground (Sritharan et al. 2004; Suleiman et al. 2006; Yang et al. 2007a, 2007b).

Current American Association of State Highway and Transportation Officials design codes (AASHTO 2010) do not provide for the influence of seasonally frozen ground effects. Consider the following:

1. How much does soil–foundation–structure interaction change the seismic response of bridges in winter versus summer?
2. How would a bridge structure designed according to current AASHTO standards respond to a seismic event during winter?
3. Is it possible that spring and fall seasons are also a problem, as soft layers may overlay an adjacent stiff layer?

Currently, some research data suggest that highway bridges respond differently to seismic effects, depending upon whether the season is winter or summer (Suleiman et al. 2006; Yang et al. 2007a, 2007b). However, no data are available to provide engineers with the necessary tools for designing bridges that mitigate or take advantage of these effects.

1.2 Problem Statement

Seasonally frozen ground across the State of Alaska is significantly stiffer than unfrozen ground. For bridges supported on deep foundations, the overall bridge stiffness measurably increases in winter months (Yang et al. 2005, 2007a, 2007b). As bridge stiffness increases, seismic demand increases (Sritharan et al. 2004; Suleiman et al. 2006). Significant changes in bridge pier boundary conditions require additional knowledge of the subsurface, and extra detailing is needed to address a bridge’s ductile performance during a design earthquake event. Currently, no design guidelines are available to account for the effects of seasonally frozen ground in a seismic analysis.

The Bridge Section of the Alaska Department of Transportation & Public Facilities (ADOT&PF) has been using a rule-of-thumb approach for analyzing the effects of seasonally frozen ground. This method has not been evaluated analytically or experimentally, but anecdotal information suggests that it is at least a reasonable estimate (Marx, personal communication, 2003).

A study of the effects of seasonally frozen ground is needed and should consist of experimentation, field-testing in known soil conditions, in situ testing of a short-spanned bridge, and analytical modeling. Such an approach is required to produce guidelines for accurate and consistent implementation of bridge design details by all designers. Two studies concerning typical Alaska soil conditions are needed to complete the work. The first study should determine how pile stiffness is influenced by the freezing of ice-rich materials (silts). The second study should determine if changes in pile stiffness occur in winter months where granular materials with various moisture content and compaction energies are present.

1.3 Literature Review

The engineering properties of frozen soil have been studied both by laboratory and field methods. The properties of frozen soil depend not only on temperature but also on water or ice content, loading rate, and duration of load. Andersland and Ladanyi (2004) reported that the strength and modulus of frozen soil decrease as water content decreases. Young's modulus of frozen soil is one or two orders of magnitude larger than that of unfrozen soil (Tsytovich 1975). For temperature change from 68°F (20°C) to 28°F (-2°C) in clay soils, an eight-fold increase in shear strength was found (Tsytovich 1975), while a fifty-six-fold increase in shear modulus was reported (Al-Hunaidi et al. 1996) when temperature dropped from 72°F (22°C) to 16°F (-9°C).

Several studies have been performed to evaluate the effects of frozen soil on soil–foundation–structure interaction. Suleiman et al. (2006) and Sritharan et al. (2004) reported a large increase in the stiffness of the bridge column-foundation-soil system in frozen condition when compared with unfrozen condition. Suleiman et al. (2006) showed that compared with the unfrozen condition, the seasonally frozen condition introduced the following changes to the lateral load response of the bridge column-foundation system:

1. increased the effective elastic stiffness by 170%.
2. increased the lateral load resistance and thus the column shear by 44%.
3. shifted the location of the maximum moment upward by approximately 33 inches (0.84 m).
4. reduced the length of the plastic region in the foundation shaft by 64%.
5. reduced the opening of the gap at the column base by 60%.

Seasonally frozen ground also can alter the overall dynamic properties of structures (Alampalli 1998; Sohn et al. 1999; Peeters and De Roeck 2001). The University of Alaska Anchorage (UAA) School of Engineering has conducted systematic research on the effects of seasonal frost on the seismic response of structures (Bai 2007; Yang et al. 2007a, 2007b; 2008; 2010; Xiong and Yang 2008; Dutta et al. 2008; Binonwangan 2009; Xu 2009). After a year of dynamic performance monitoring of the Port Access Bridge in Anchorage, Alaska, Yang et al. (2007a, 2007b) reported that modal frequencies of the bridge varied because of seasonal freezing and thawing of ground. The results of their study showed that variations in modal frequencies of the first two transverse modes between summer and winter are about 12% and 20%, respectively.

1.4 Objective

We proposed forming a team of researchers from the University of Alaska Fairbanks (UAF) and UAA to investigate the problem of seasonally frozen soil effects on the seismic performance of highway bridges. Researchers from Iowa State University (ISU) provided technical input to this project and received testing data that resulted from it. Bridge design engineers from the Bridge Design Section of ADOT&PF played a technical advisory role.

The objectives of this project were to (1) gain an in-depth understanding of seasonally frozen ground effects on the seismic response of bridges, and (2) help establish design guidelines for including effects of frozen soil conditions typical of Alaska in bridge seismic analysis. Item 1 has been studied through laboratory testing, with full-scale bridge tests and by conducting a sensitivity analysis of the boundary conditions through the use of computer modeling. Item 2 has been evaluated by modeling and analyzing, by coordination of findings between the three research teams, and finally, through detailing bridge structures.

1.5 Scope of Work

This research was carried out in two parts. Part I focused on testing and modeling a bridge foundation system, and on evaluating the behavior of a single pile embedded in soil and subjected to lateral load. Strains, displacements, and ground temperatures were measured and compared with predictive models. This portion of the study provided the basis for analyzing the frozen ground effects on a bridge and for proposing guidelines for designing bridge foundations. Part II focused on field testing and modeling a short-spanned bridge under the influence of seasonally frozen ground. The results obtained from Part II were used to partially verify the findings that resulted from Part I and to form the basis for recommending design guidelines for bridge structures in Alaska as well as other cold regions.

CHAPTER 2. SINGLE-PILE EXPERIMENTS

Specific details not presented in this chapter may be found in two master’s degree theses presented at UAF (Davis 2010; Horazdovsky 2010).

2.1 Types of Tests

This study was conducted by performing two types of field tests on 25-foot-long 16-inch-diameter steel-jacketed reinforced concrete piles embedded approximately 20 feet in silt. The pile tops were a free end. The purpose of this study was to evaluate pile behavior during winter months; that is, to determine depth of fixity (fixed-free), a simplification that is often used to approximate this complicated structure–soil problem.

The two types of tests were (1) measurements to determine natural frequency and damping for two test piles and a reaction pile during summer and winter; and (2) measurements to determine lateral behavior (lateral load versus displacement) for cyclically applied static loads that were ramped from zero to failure for a summer test and a winter test (two-test pile tests).

2.2 Site Selection and Geotechnical Investigation

The criteria for selecting a test site included the following:

1. A thick layer of seasonally frozen soil
2. Silty soil with high moisture content
3. Proximity of location to the UAF campus
4. Permafrost lower than the bottom of the test piles
5. Easily accessible by pile-driving equipment

Several sites throughout the Fairbanks area were explored as possible test sites. Initially the permafrost depth for each site was evaluated to ensure that the test site met the criteria that piles not be embedded in permafrost. The site selected for pile testing was the Farmers Loop Permafrost Research Site. Prior to selecting this location, the site was hand-probed to ensure that the depth of permafrost was below the bottom tip of the pile. This test site is owned and operated by the U.S. Army Corps of Engineers Cold Regions Research and Engineering Laboratory (CRREL); it is also an ASCE-dedicated research site. The test site is located in Fairbanks, Alaska, at mile 0.9 Farmers Loop Road, approximately 8 miles from the UAF campus.

An exhaustive geotechnical report of mechanical soil properties was not within the scope of this document to include, except to note the type of soil as relevant to this specific study. The mechanical properties of soil at the test site (Fairbanks silt) are documented in published CRREL research reports (Zhu and Carbee 1987). The test pile locations and test configuration are shown in Figures 2.1 and 2.2.

As part of the selection of the test site on Farmers Loop Road, a preliminary soil investigation was completed. Shallow test holes were dug, and the permafrost table was located at several places at the site. Shallow holes were dug by hand and the permafrost table was found by working a half-inch-diameter rod into the soil until refusal of the rod was reached. The location that was selected is 64°52.52′ N, 147°40.391′ W, approximately 75 feet from the CRREL test site meteorological station. Preliminary investigation revealed a thin layer of gravel overlaying silt and a permafrost table located 20 to 22 feet below ground surface. A drill rig was used to take soil borings at the proposed location for the two test piles and the reaction pile.

Borehole samples were logged by Mikhail Kanevskiy, Ph.D., from the Department of Civil and Environmental Engineering at UAF. Split-spoon, blow count, and moisture samples were taken during each investigation. Sieve analysis and hydrometer tests were conducted in a laboratory.

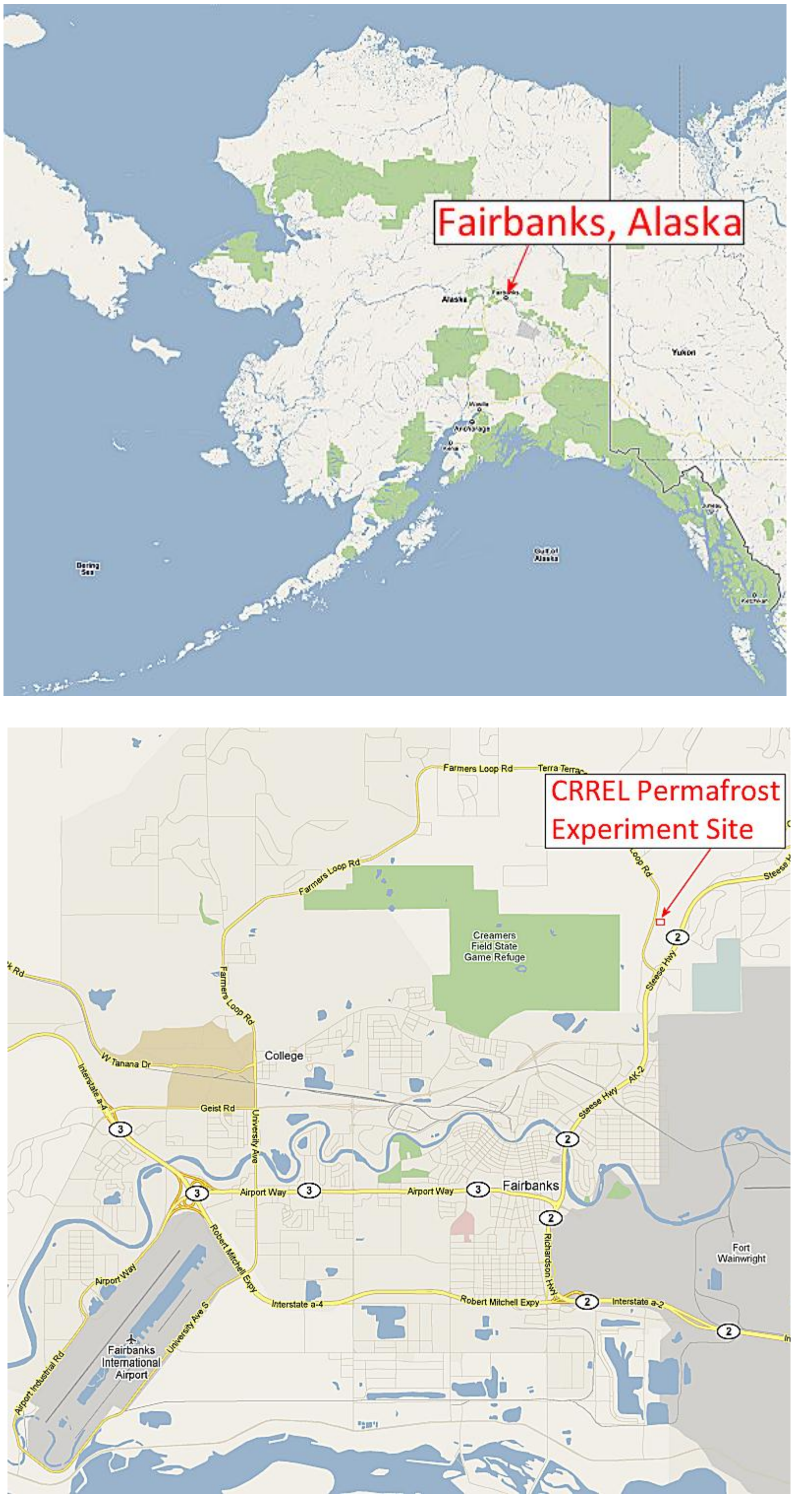

Figure 2.1: Test site location (Google n.d.).

Figure 2.2: Test pile location and layout plan view (Google n.d.).

2.3 Design and Construction of the Reaction and Test Piles

The test piles were designed to simulate steel-jacketed, reinforced concrete piles commonly used by ADOT&PF. The idea was to have experimental results analogous to field performance data. The ADOT&PF design recommendations for this test year are based on “Guide Specifications for LRFD Seismic Bridge Design, 1st edition, with 2010 Interim Revisions, Single User Digital Publication” (AASHTO 2010). The test piles were designed to meet the needs of two related studies: structure–soil interaction to small lateral loads and dynamic free vibration (test type 1), and structure–soil interaction to large lateral loads wherein the piles are loaded to failure (test type 2).

The two test piles and the reaction pile were 25-feet long. Each test pile had a 20-foot embedment design length. Figure 2.3 shows a cross-section of a typical 16-inch-diameter test pile. Eight Number 6 ASTM A706 reinforcing bars provided 1.93% of the cross-sectional area. Similarly, the 24-inch-diameter steel-jacketed reaction pile was provided with ten Number 8 ASTM A615 reinforcing bars that provided 1.9% of the cross-sectional area.

At the recommendation of ADOT&PF, we specified Schedule 40 for the 16-inch pipe piles (the jacket-diameter-to-wall-thickness ratio should be nearly 48:1). Similarly, for the 24-inch reaction pile, a 0.5-inch nominal wall thickness was specified. After installation, however, we discovered that the material supplier sent 0.375-inch wall thickness pipe instead. Since this pile was intended for use as reaction force only, the deviation was not considered critical.

Shear reinforcement consisted of Number 3 reinforcing bars bent into rings (or hoops) and spaced on 12-inch centers outside of the longitudinal reinforcing bars. The outside diameter of each hoop was 1 inch less than the inside diameter of the steel pipe jacket.

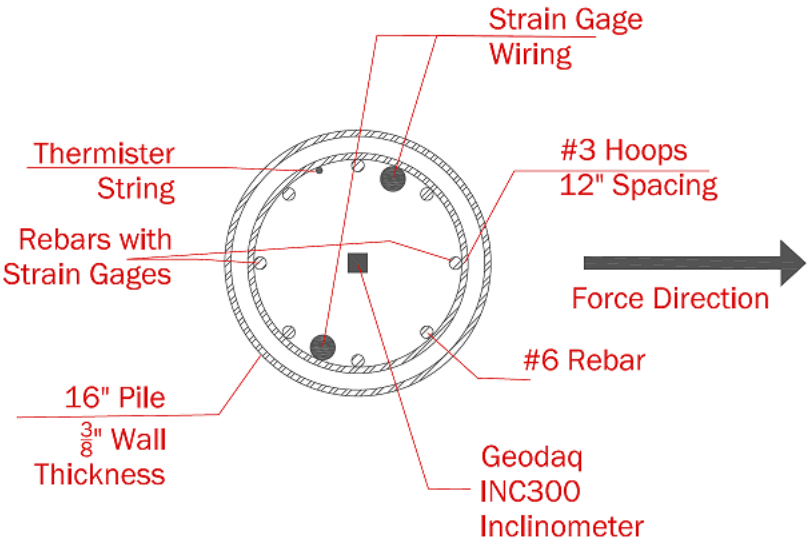

Figure 2.3: Test pile configuration.

2.4 Instrumentation and Test Configurations

On the reinforcing bars, we installed 30 full-bridge strain gages manufactured by Hitec Products, Inc. (HPI), Models HBWF-35-125-6-30GP-SS and HBWF-35-125-6-50GP-SS (the difference being the length of supplied cable). The gage factor was 4.15.

Two reinforcement bars directly in the line of force (see Figure 2.3) were milled at the planned location of the strain gages, providing a flat surface for the spot weld but reducing the reinforcing bar cross-sectional by approximately 12% over about 1½ inches (slightly more than the length of the strain gage). After spot welding, each strain gage (sensor) was covered in silicone and caulked to protect the sensor from water infiltration and to decouple the sensor housing from concrete during use (see Figures 2.4 and 2.5). Wires from each strain gage were run along the reinforcing bar to the nearest hoop, and then to a 1-inch PVC conduit that led to the top of the pile. All pile reinforcing bars (with and without sensors) were placed in a cage. The cage was secured using six jigs evenly spaced along its length. The jigs were manufactured in the shape of a clamshell and designed for easy removal during lowering of the cage into the steel-pipe pile at the test site. Figure 2.6 shows jigs in place on a test pile reinforcing bar cage under construction in the laboratory.

An inclinometer (using tilt sensors) was installed at the center of the rebar cage. This inclinometer was used to measure the three-dimensional location of the deformed pile at a given point in time. That is, by multiplying sensor slope by spacing, the deformed shape can be calculated along the length of the pile. We used a Model INC300 series inclinometer and a GCM 1200 control module to read the sensor data. Both the inclinometer and the control module were manufactured by Geodaq Automated Instrumentation and Data Acquisition Services (Geodaq 2010). The inclinometer is accurate for the measurement range used during pile testing; that is, the accuracy of any point is ± 0.03 inch (Geodaq 2006). See Figures 2.7 and 2.8 for pictures of the inclinometer as installed in the rebar cage before concrete was poured.

Figure 2.4: Strain gage after spot welding.

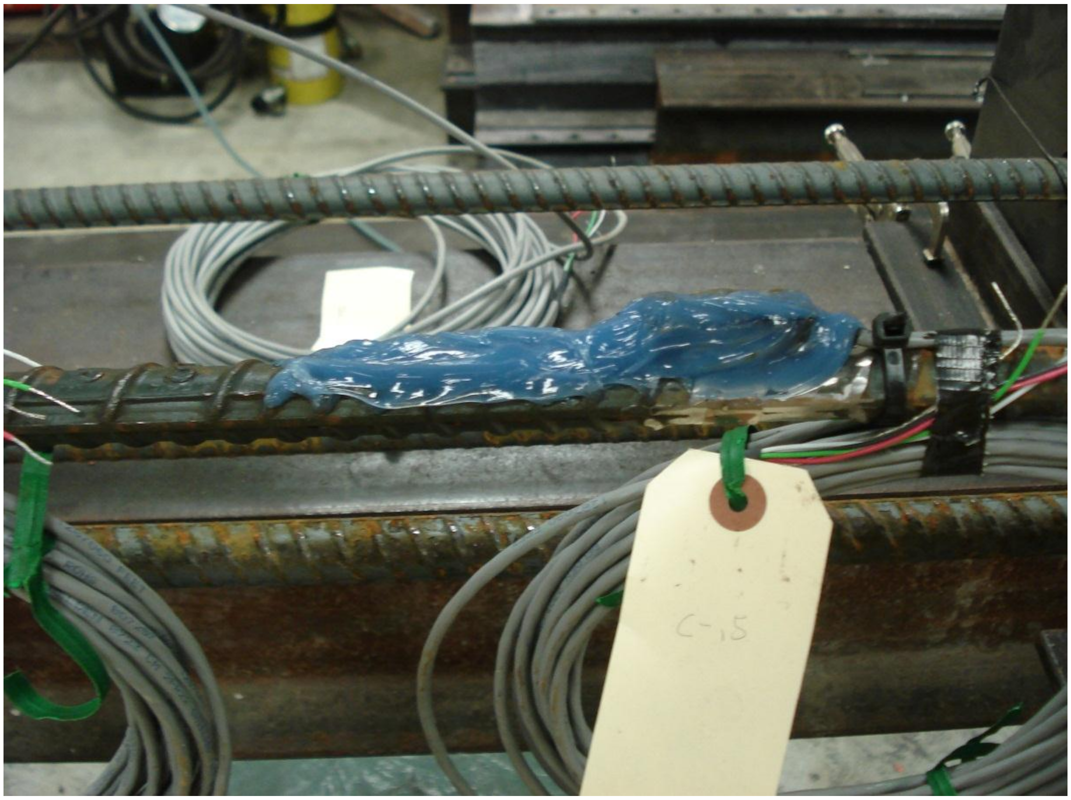

Figure 2.5: Strain gage mounting after moisture sealing.

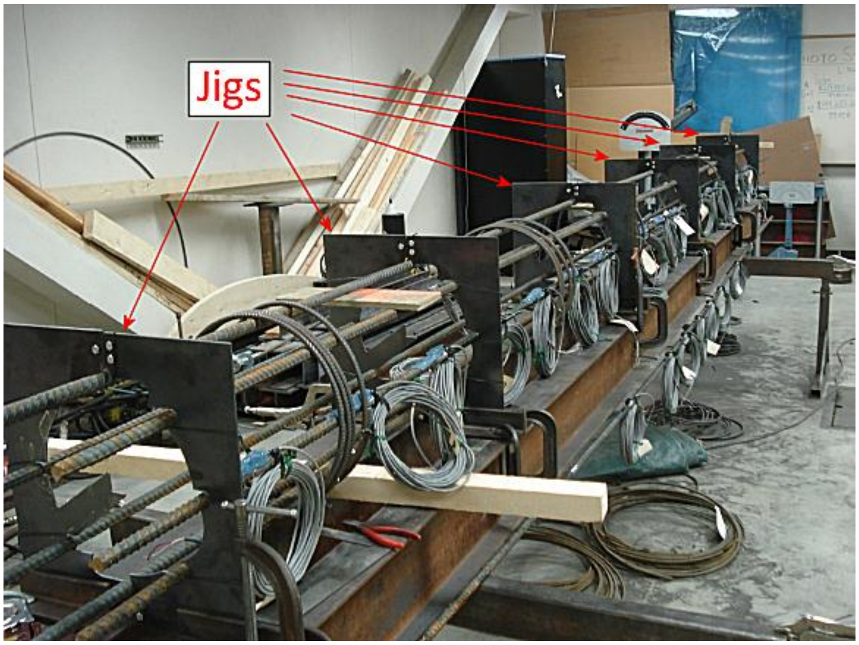

Figure 2.6: Jigs used during construction of reinforcing bar cages.

Figure 2.7: Inclinometer as installed in the test pile.

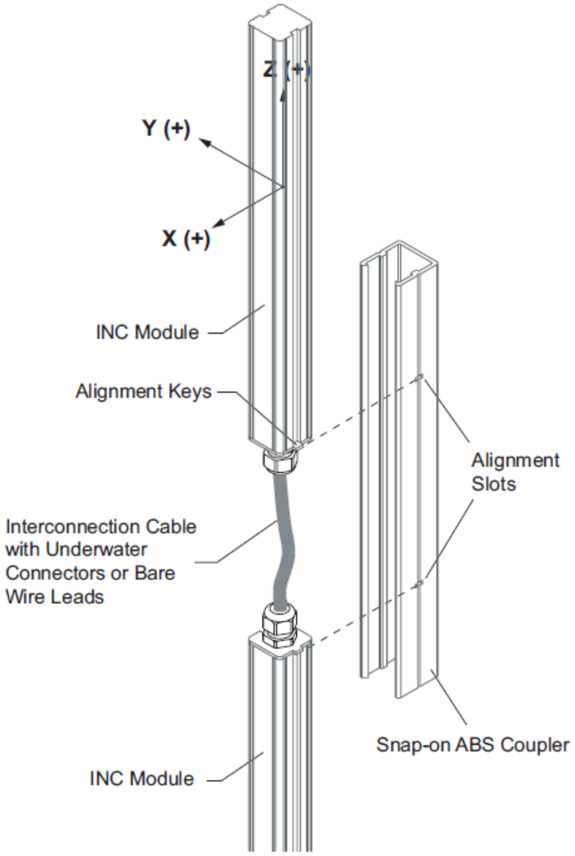

Figure 2.8: Setup for inclinometer measurements.

In addition to strain and deformation (tilt) sensors installed in the test piles, soil subsurface and test pile temperatures were recorded using thermistors Model YSI 44033, with a reported 0.1°C interchangeability, which means variation in measurement from one sensor to the next is less than 0.1°C.

We manufactured thermistor strings for the test piles; each pile had 22 thermistors located inside but near the steel jacket. An additional thermistor sensor cable was installed in soil between 20 and 30 feet from the test piles. This sensor cable was purchased from and installed by Geo-Watersheds Scientific, a local consulting firm that specializes in soil temperature measurement. The readings from the sensor cable were used as a control to determine whether the temperatures reported in the piles were reasonable when compared with the temperature reported in the soil. In addition to these data sets, wind direction and temperature were monitored at a CRREL-maintained weather station approximately 100 feet from the test piles.

Due to limited work space between pile instrumentation, pile, and reinforcing, a self-consolidating concrete was used. With this concrete, use of a vibrator was not required. This project required 7.5 cubic yards of concrete. The mix consisted of

- 10,700 pounds of 3/8-inch gravel with 1.26% moisture content;
- 13,000 pounds of sand with 3.19% moisture content;
- 4,576 pounds of type-one Portland cement;
- 140 gallons of water;
- 320 ounces of Glenium admixture; and
- 4 ounces of air entrainment admixture.

A 4-inch PVC pipe with smooth sides and the same length as the reinforcing cage was installed to protect the sensors from becoming dislodged or damaged during concrete placement. The concrete pump truck hose (2-inch diameter) fit inside the PVC pipe, and as the level of concrete rose in the pile, the PVC pipe and the pump truck hose were extracted together. All instrumentation except the inclinometer were read and powered by a Campbell Scientific CR9000X data acquisition system. Locations of installed sensors for each test pile are presented in Table 2.1.

Table 2.1: Pile Sensor Initial Elevations (as constructed)

				Thermistors	
Elevation [in]	Strain A	Strain B	INC300	Test Piles	Soil
48	---	---	1	1	---
36	---	---	1	1	---
24	---	---	1	1	---
12	---	---	1	1	---
0	1	1	1	1	1
-12	1	---	1	1	1
-24	1	1	1	1	1
-36	1	---	1	1	1
-45	---	---	---	1	1
-48	1	1	---	---	---
-54	---	---	1	1	1
-60	1	1	---	---	---
-66	---	---	1	1	1
-72	1	1	---	---	---
-78	---	---	1	1	1
-84	1	1	---	---	---
-90	---	---	1	1	1
-96	1	1	---	---	---
-102	---	---	1	1	1
-108	1	---	---	---	---
-114	---	---	1	1	1
-120	1	1	---	---	---
-126	---	---	1	1	1
-132	1	---	---	---	---
-138	---	---	1	1	1
-144	1	1	---	---	---
-150	---	---	---	1	1
-156	1	---	1	---	---
-168	1	---	1	1	1
-180	1	1	1	---	---
-192	1	---	1	1	1
-204	1	---	1	---	---
-216	1	---	1	1	1
-228	1	---	1	---	---
-240	---	---	1	1	1

No sensors were installed in the reaction pile. Negative numbers indicate subsurface depth. The ground surface at installation was zero elevation, and that is the primary reference datum for sensor position.

2.5 Installation of Piles at the Field Test Site

The original contract to install piles at the test site called for driving the steel pipe jackets into the soil, either post- or pre-drilled at the contractor’s option. The contractor asked if the steel pipe jackets could be vibrated in place, since that equipment was immediately available.

The contractor was given the go-ahead, with the provision that the company would be responsible for any negative consequences of deviating from the original intent. The contractor used a vibrating head, as shown in Figure 2.9, to install the steel pipe jackets for the piles; these were open-ended steel pipes. Once the depth was reached, the contractor removed the soil inside the pile. In this case, the contractor chose to remove the soil by vibrating a 12-inch-diameter pipe with a trapdoor plate at the toe (similar in operation to a check valve) down through the center of the pile. Soil pushed into the 12-inch pipe as it was vibrated down, but was prevented from sliding back out by the trapdoor.

The vibration from the vibrating head, used to drive the pile jacket and clean out soil inside the jacket, appeared to cause surrounding soil to liquefy. The following day, a vacuum truck was hired to remove heaved soil and excess water inside the pipe jackets to provide for placement of reinforcing cages and concrete.

The new soil continued to heave after it was removed by the vacuum truck. Therefore, a decision was made to remove soil beyond the toe of the pile to give sufficient time for installing the reinforcing bar cage and concrete. The jigs installed on the reinforcing cage (used to keep bars and sensors in position) were removed as the cage was lowered into the pile jacket (see Figure 2.10). To ensure that zero elevation datum was achieved for the reference sensors, each reinforcing bar cage was suspended onto the pipe jacket using prefabricated, carefully measured S-shaped hooks. Three S-shaped hooks were used to suspend each pile's reinforcing bar cage.

After the reinforcing-bar cages were hung on their respective pipe jackets, a concrete pump truck delivered concrete. The hose from the pump truck was lowered into the 4-inch PVC pipe until near the bottom of the pile, and the concrete was placed. The pump truck hose and the PVC pipe were extracted together as concrete filled the pile. Air content and slump were tested at the time of placement. In addition, concrete cylinder samples and beam samples were obtained by the supplier.

After the concrete was set, minor earthwork was performed at the site to remove the top organic layer, and the site was surveyed to establish baseline elevation data. The soil around the piles was leveled with a small bucket loader and hand tools to a radius of at least 10 feet around each pile. Excess surface water at the test site was diverted to a nearby culvert by carving a channel around the perimeter of the leveled soil.

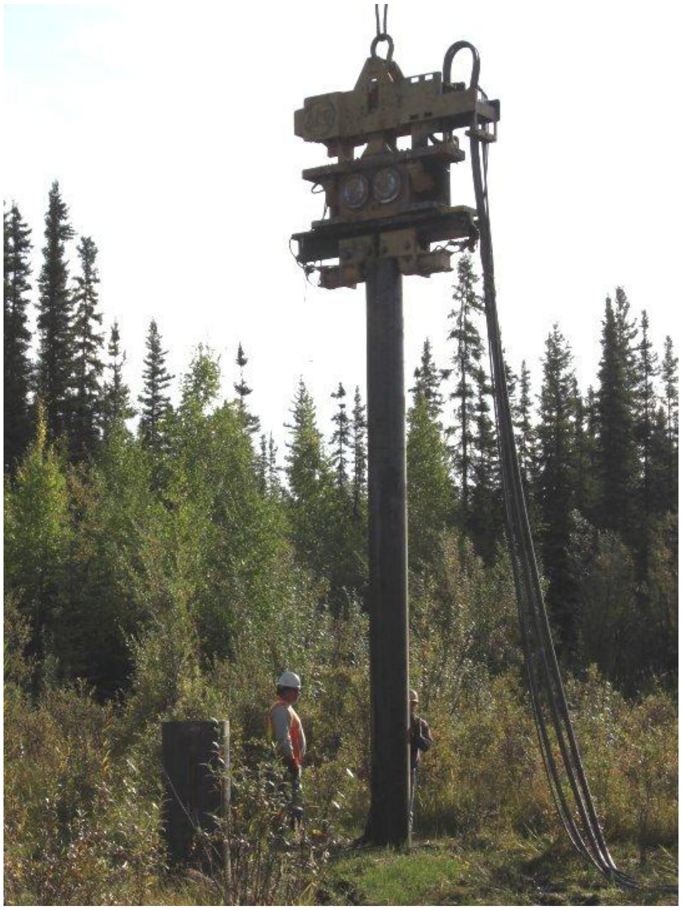

Figure 2.9: Installing a test pile using a vibration head (photo by INE staff).

Figure 2.10: Installing a reinforcing steel cage with sensors into a test pile (photo by INE staff).

2.6 Test Type 1: Tests to Measure Free-Vibration Response

In the Test Type 1 sequence of tests, we applied a lateral load to a pile using a manually operated Jet, Model JLP-300-10, chain hoist rated at 3 tons (6,000 pounds) (see Figures 2.11 and 2.12). The load was measured with a 10,000-pound Honeywell, Model 41, load cell. Lateral displacement was measured at either two or four positions with Daytronics LVDTs. Load and displacements were sampled at 25 Hz.

Load was quickly released with a Sea Catch, Model TR-7, quick disconnect, manufactured by McMillan Design, Inc. The Sea Catch is rated at 3.52 tons (7,040 pounds), and requires approximately 40 pounds to actuate. This quick-release mechanism was attached to a bracket that was fabricated and bolted onto the piles.

The accelerometer used to measure how the pile vibrated once the load was released was manufactured by PCB Piezotronics, Model PCB 353B01; it had a measurement range of positive or negative 250 gravities (peak). The accelerometer had its own power supply and signal conditioner, Model PCB 480C02, and the output signal from the conditioner was read as differential voltage by the CR9000X data logger.

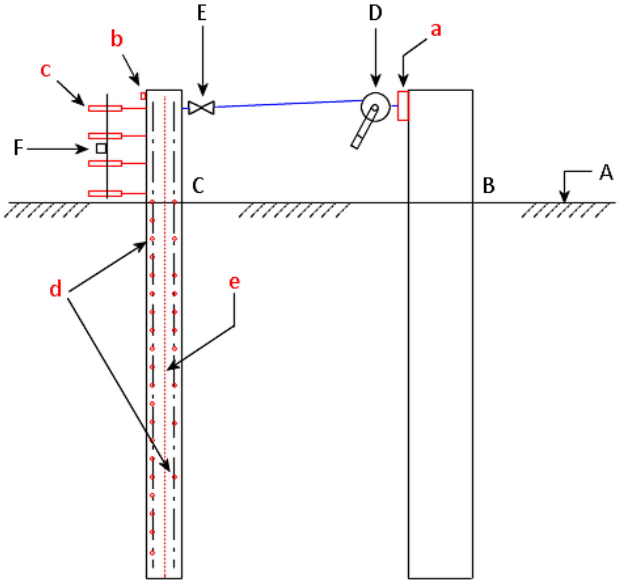

Figure 2.11: Elevation – Test configuration for free-vibration response.

The components are A – soil surface; B – reaction pile; C – test pile; D – chain hoist; E – quick disconnect; F – bridge for LVDT sensor array (end supports not shown for clarity); a – load cell; b – accelerometer; c – LVDT sensor array; d – strain gages on reinforcing bars; e – inclinometer. This sketch is not to scale.

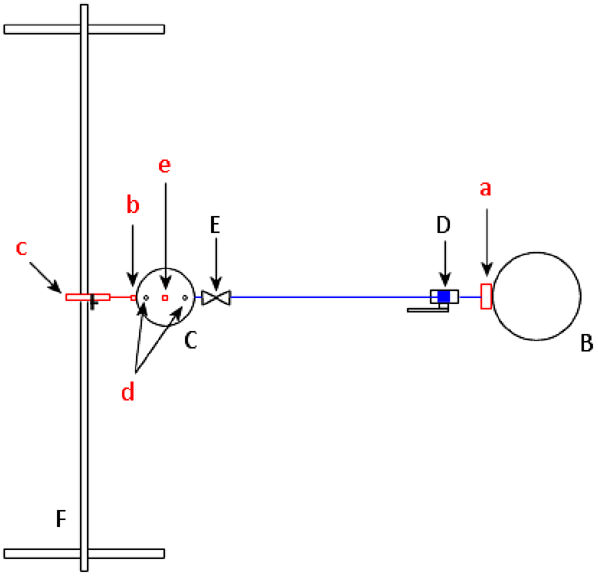

Figure 2.12: Top view – Test configuration for free-vibration response.

The components are B – reaction pile; C – test pile; D – chain hoist; E – quick disconnect; F – bridge for LVDT sensor array; a – load cell; b – accelerometer; c – LVDT sensor array; d – strain gages on reinforcing bars; e – inclinometer. This sketch is not to scale.

2.7 Test Type 2: Quasi-static Cyclic Lateral Load Tests

It may be argued that the pile (soil structure) responds as a function of soil type, soil moisture, ground temperature, pile stiffness, rate of loading, number of load cycles, and conditions prior to the load application.

Thus, an instrumentation plan was developed to assist in understanding how a pile responds to cyclic quasi-static laterally applied loads for different seasonal exposures (summer versus winter). To evaluate the influence of lateral loading on piles in seasonally frozen soils or thawed soils, we measured the following:

1. Deflection above the ground line, at ground line, and below the ground line.
2. Temperature of the pile and the soil with depth.
3. Pile strain.
4. Load applied to the pile and the time when it was applied.

The two test piles were instrumented with 30 strain gages, 1 inclinometer, 22 thermistors, and 6 linear motion transducers (LMTs). All instrumentation except the inclinometer was read and powered by a Campbell Scientific CR9000X data acquisition system. The load frame was equipped with a load cell, and the reaction pile was not instrumented.

2.7.1 Sensors for measuring deflection and load above the ground surface

Deflection above the ground surface was measured using LMTs manufactured by Ametek. This measurement conformed to ASTM D3966-07 Standard Test Methods for Deep Foundations under Lateral Load (ASTM 2007). During testing, six LMT sensors were used to monitor aboveground lateral movement of the pile. The elevation of each sensor is presented in Table 2.2.

Loads were applied to the pile with an Enerpac ram and measured with a 200-kip load cell. The load cell used for this study was a Honeywell, Model 41, precision load cell with a 200,000-pound capacity and 150% overload capacity. Accuracy of the load cell is ± 0.1% of full scale. During testing, LMT sensors and the load cell were read every 0.1 seconds.

Table 2.2: Gage Location / Elevations as Tested

North Pile as Tested		South Pile as Tested	
Elevation from Ground Surface (in)	Gage at Elevation	Elevation from Ground Surface (in)	Gage at Elevation
59.75	LMT 1	59.75	LMT 1
53.75	Inc & Therm	52.50	Inc & Therm
49.75	LMT 2	49.75	LMT 2
41.75	Inc & Therm	40.50	Inc & Therm
40.25	LMT 3	40.25	LMT 3
29.75	Inc & Therm	28.50	Inc & Therm
28.25	LMT 4	28.25	LMT 4
17.75	Inc & Therm	16.50	Inc & Therm
16.25	LMT 5	16.25	LMT 5

North Pile as Tested		South Pile as Tested	
5.75	A0, B0, Inc & Therm	4.50	A0, B0, Inc & Therm
4.25	LMT 6	3.00	LMT 6
-6.25	A1, Inc & Therm	-7.50	A1, Inc & Therm
-18.25	A2, B2, Inc & Therm	-19.50	A2, B2, Inc & Therm
-30.25	A3, Inc & Therm	-31.50	A3, Inc & Therm
-42.25	A4 & B4	-43.50	A4 & B4
-48.25	Inc & Therm	-49.50	Inc & Therm
-54.25	A5 & B5	-55.50	A5 & B5
-60.25	Inc & Therm	-61.50	Inc & Therm
-66.25	A6 & B5	-67.50	A6 & B5
-72.25	Inc & Therm	-73.50	Inc & Therm
-78.25	A7 & B6	-79.50	A7 & B6
-84.25	Inc & Therm	-85.50	Inc & Therm
-90.25	A8 & B7	-91.50	A8 & B7
-96.25	Inc & Therm	-97.50	Inc & Therm
-102.25	A8	-103.50	A8
-108.25	Inc & Therm	-109.50	Inc & Therm
-114.25	A10 & B9	-115.50	A10 & B9
-120.25	Inc & Therm	-121.50	Inc & Therm
-126.25	A10	-127.50	A10
-132.25	Inc & Therm	-133.50	Inc & Therm
-138.25	A12 & B11	-139.50	A12 & B11
-150.25	A13, Inc & Therm	-151.50	A13, Inc & Therm

North Pile as Tested		South Pile as Tested	
-162.25	A14, Inc & Therm	-163.50	A14, Inc & Therm
-174.25	A15, B15 Inc	-175.50	A15, B15 Inc
-186.25	A16, Inc & Therm	-187.50	A16, Inc & Therm
-198.25	A17 & Inc	-199.50	A17 & Inc
-210.25	A18, Inc & Therm	-211.50	A18, Inc & Therm
-222.25	A19, Inc & Therm	-223.50	A19, Inc & Therm
-234.25	Inc & Therm	-235.50	Inc & Therm

Abbreviations

- Inc – inclinometer Therm – thermistor
- A# - Tensile Strain gage
- B# - Compressive Strain gage

2.7.2 Sensors for measuring strain in the reinforcing bars

For lateral-loaded pile tests, it is important to measure load, time, and deflection as a function of depth. Aboveground surface deflections of the pile were measured using LMTs. Deflection of the pile below the ground surface was more difficult to measure; these deflections were measured indirectly. To accomplish measurements below the ground surface, two separate systems were employed. The first system consisted of 30 strain gages (in which the strain may be integrated to determine relative displacement); the second system consisted of an inclinometer. All strain gages located inside the test pile were mounted to the reinforcing bar (rebar) cage in the laboratory, and then transported to the test site and lowered into the pile. Placement of the gages in the completed test piles was accurate to approximately one-eighth inch in any direction. After installation, sensors in both test piles had the same elevation with respect to ground surface. During the winter of 2008–2009, the piles underwent frost jacking, with each pile being raised out of the ground to a different elevation.

In the past, strain gages have been used to measure strains throughout the pile length. Once the strain profile was obtained at a given point during the test, a curve would be fit to the data. The equation of the curve could then be integrated twice to get a deflected shape. Theoretically, this method works well, but experimentally, errors are compounded and results can be difficult to interpret. In many cases, the pile being tested was calibrated in the laboratory before being installed in the ground (Foriero et al. 2005; Cox et al. 1974; Reese and Welch 1975). The pile was calibrated by subjecting it to bending in the laboratory so that a correlation between strain and the deflected shape of the pile could be made. The calibrated test pile was then placed in the ground and tested. After testing, the test pile was removed from the soil, taken back to the lab, and again subjected to bending. Another correlation between the deflected shape of the pile and strain measurements was then made. For our experiment, this type of calibration would have been difficult and expensive to do, as the pile tested is a reinforced concrete-filled pipe pile that may exhibit nonlinear properties during bending; that is, its stiffness changes as the concrete cracks.

2.7.3 Sensors for measuring soil and pile temperatures

The piles were tested in both frozen and unfrozen condition. The temperature of soil in the frozen condition is important, as is the depth of the frozen soil layer. The temperature of the soil has a significant impact on soil strength. To accurately measure soil temperatures, thermistors, which measure temperature, were placed throughout each test pile (the north test pile and the south test pile) and in a soil string located between 20 and 30 feet away from the test piles. The accuracy of the thermistors is ± 0.1°C. The thermistors in the test piles were placed approximately 1 inch inside the steel pipe jacket. All three soil strings were read throughout the winter by CRREL employees, who monitored the soil strings at their meteorological station at the test site.

2.7.4 Data acquisition system

A Campbell Scientific CR9000X (Campbell Scientific 2010) data acquisition system was selected for this study.

2.7.5 Test 2 – Quasi-static cyclic lateral-loaded pile tests

Cyclic quasi-static lateral loads were applied to two 16-inch-diameter steel-jacketed reinforced concrete test piles. The testing was designed to create a correlation between stiffness of the pile in unfrozen soil and stiffness of a similar pile in a layer of seasonally frozen soil. Extensive testing has been conducted on piles in unfrozen soils. Some testing of piles in permafrost has been done, but very little testing of piles in seasonally frozen soils has been done. Testing for this portion of the project consisted of three full-scale pile tests. The first test was in September 2009 (fall). At the time, the soil was thawed for the full length of the pile. The second test was performed in January 2010. This date was chosen in an attempt to test when frost depth would be approximately half the expected maximum depth of frozen conditions. The final test was conducted in late March 2010, when depth of seasonally frozen soil is nearly at its maximum.

2.7.5.1 Lateral-load pile testing procedure

Two standards provide guidelines for laterally loaded pile testing. The first standard is a draft of a report entitled "Recommendation for Seismic Performance Testing of Bridge Piers" (FHWA 2004). The report was prepared for the Federal Highway Administration (FHWA) in an attempt to standardize bridge pier testing. The other standard is published by the American Society of Testing and Materials: ASTM D3966-07 Standard Test Methods for Deep Foundations under Lateral Load (ASTM 2007). Since the FHWA (2004) report was specifically drafted for seismic testing of bridge piers, it was the primary reference used in this study. ASTM D3966-07 was used where the FHWA report was not specific enough.

According to the FHWA (2004) report, pile testing falls under Type A2, Quasi-static Cyclic Testing, under the classification of quasi-static testing. Thus, the effects of inertia can be ignored. While cyclic testing from compression to tension to create asymmetric load conditions is recommended, equipment limitations precluded cycling from tension to compression. The test equipment could only pull the test pile toward the reaction pile. Further, displacement control, which is recommended by FHWA, was used for cyclic testing of piles. Thus, during September's test, displacement control was used. Displacement control is designed for soils, where exceeding the ram stroke usually defines failure or the end of testing. Displacement control was attempted during winter testing. As loads spiked to almost 50% of the yield strength of the pile without the pile deflecting 0.1 inch at the ram, it became clear that load control, not displacement control, should be used for winter testing.

The following recommendations from FHWA shaped the test plan:

1) Initial amplitude should be below yielding of the pile.
2) Subsequent amplitudes should be between 1.25 times and 1.5 times the current amplitude.
3) Three load cycles should be applied for each amplitude.

The loading plan used for pile testing is presented in Figures 2.13, 2.14, and 2.15. The September test was displacement-controlled. Because of ground stiffness, January and March tests were load-controlled.

While a constant ram speed throughout the entire loading program is recommended, some variation in loading speed is commonly practiced (FHWA 2004). Obtaining a constant speed throughout the test was extensively explored, but in the end, we determined that this was not possible without going to a computerized hydraulic loading system. The loading rate for the pile was variable, with a maximum loading speed at the ram of 7 inches/minute (0.29 cm/sec) for loads less than 22 kips and 1 inch/minute (0.0423 cm/sec) for loads over 22 kips. These load speeds are only approximations, and were obtained using the manufacturer's pump specifications for the pump and the effective area of the hydraulic ram, which is 22.5 square inches (see Figure 2.16 for the pump flowchart.

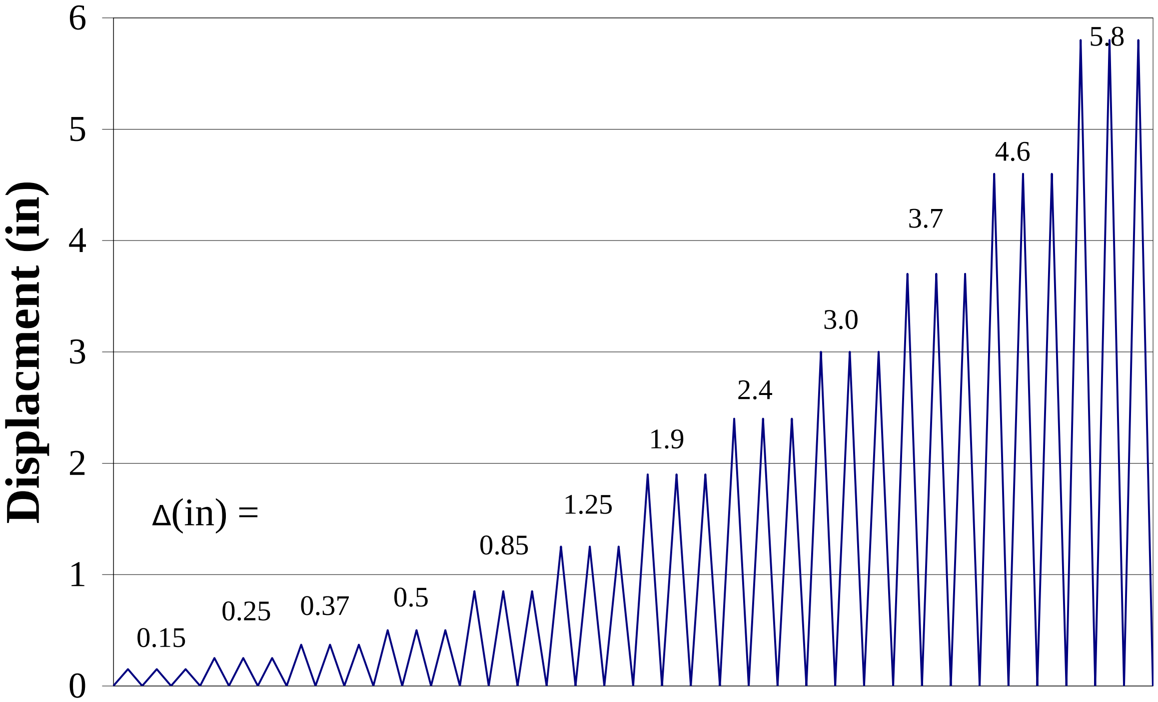

Figure 2.13: September target displacement increments.

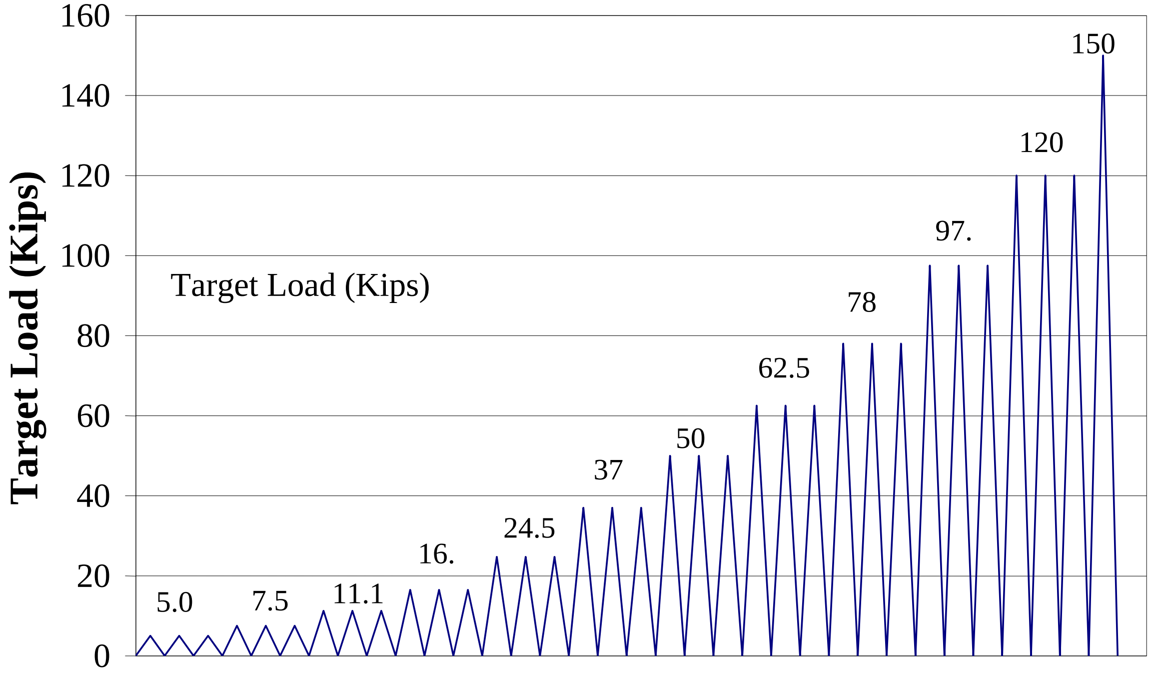

Figure 2.14: January target load increments.

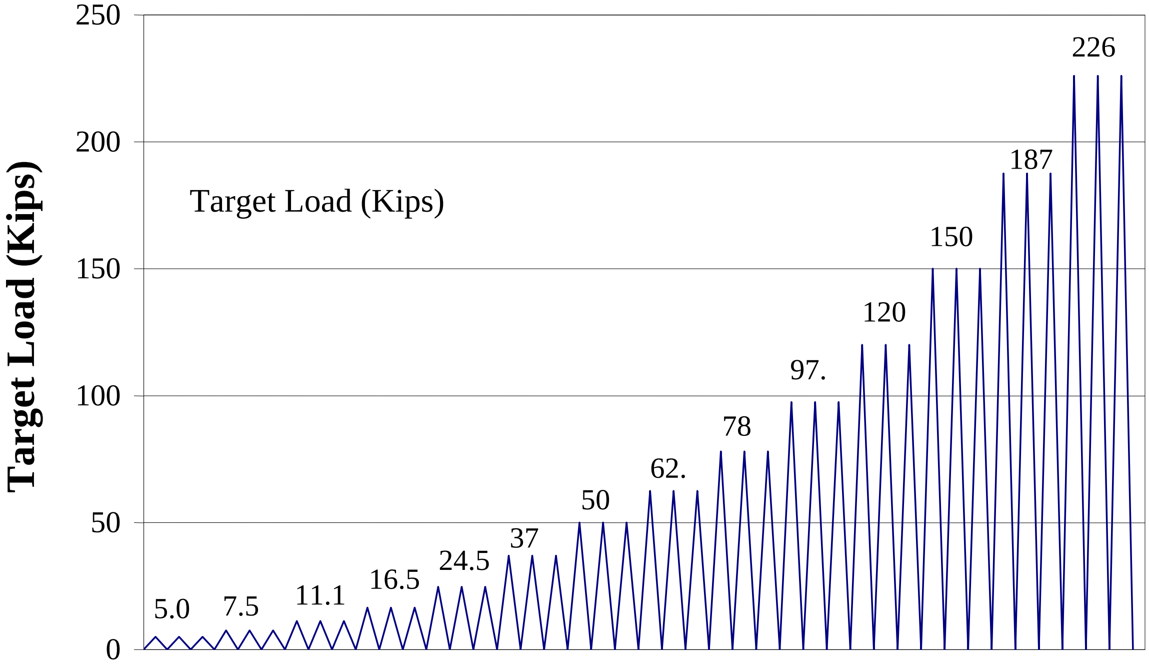

Figure 2.15: March target load increments.

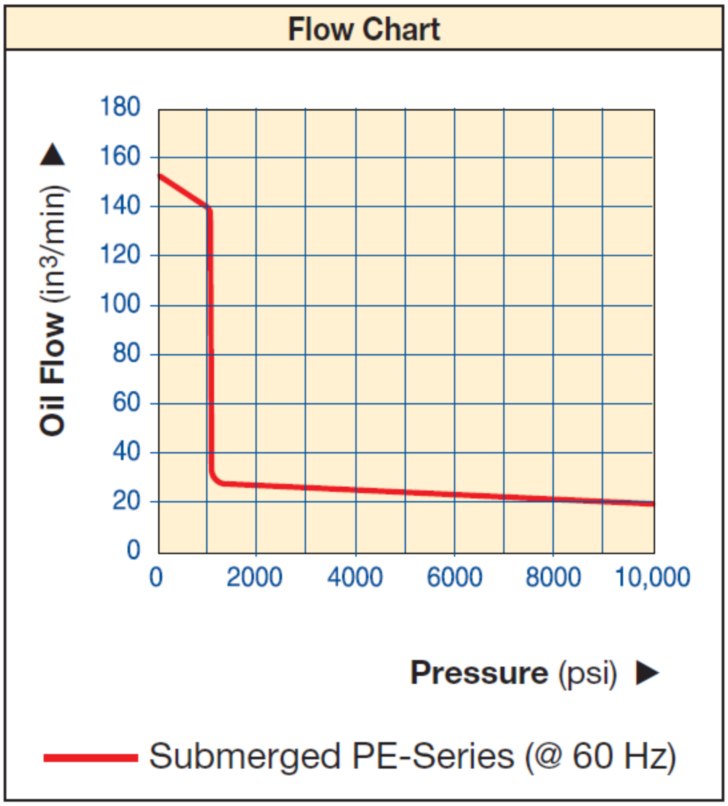

Figure 2.16: Flowchart – Hydraulic pump (Enerpac PE), Model PEJ1401B.

2.7.5.2 Test frame design construction and testing

The test frame was designed to meet the requirements set forth by ASTM D3966-07 and the FHWA (2004) report. The test frame was originally designed using allowable stress design (ASD) methods to limit the amount of stress to which each frame component was subjected. The estimated yield strength of the pile was 4,400 kip-inches, and the estimated ultimate strength of the pile was 8,700 kip-inches. For the September test, the estimated location of the maximum moment was between 48 and 96 inches below ground surface. Using the equivalent stiffness method, and assuming that the pile is fixed at 48 inches below grade and the ram is located 40 inches above grade, approximately 90 kips were required to fail the pile. The design capacity of the frame was 120 kips, which was 30% beyond the estimated capacity of the pile. The frame was also designed with a factor of safety, giving an increased capacity (see Figures 2.17 and 2.18 for the test frame design).

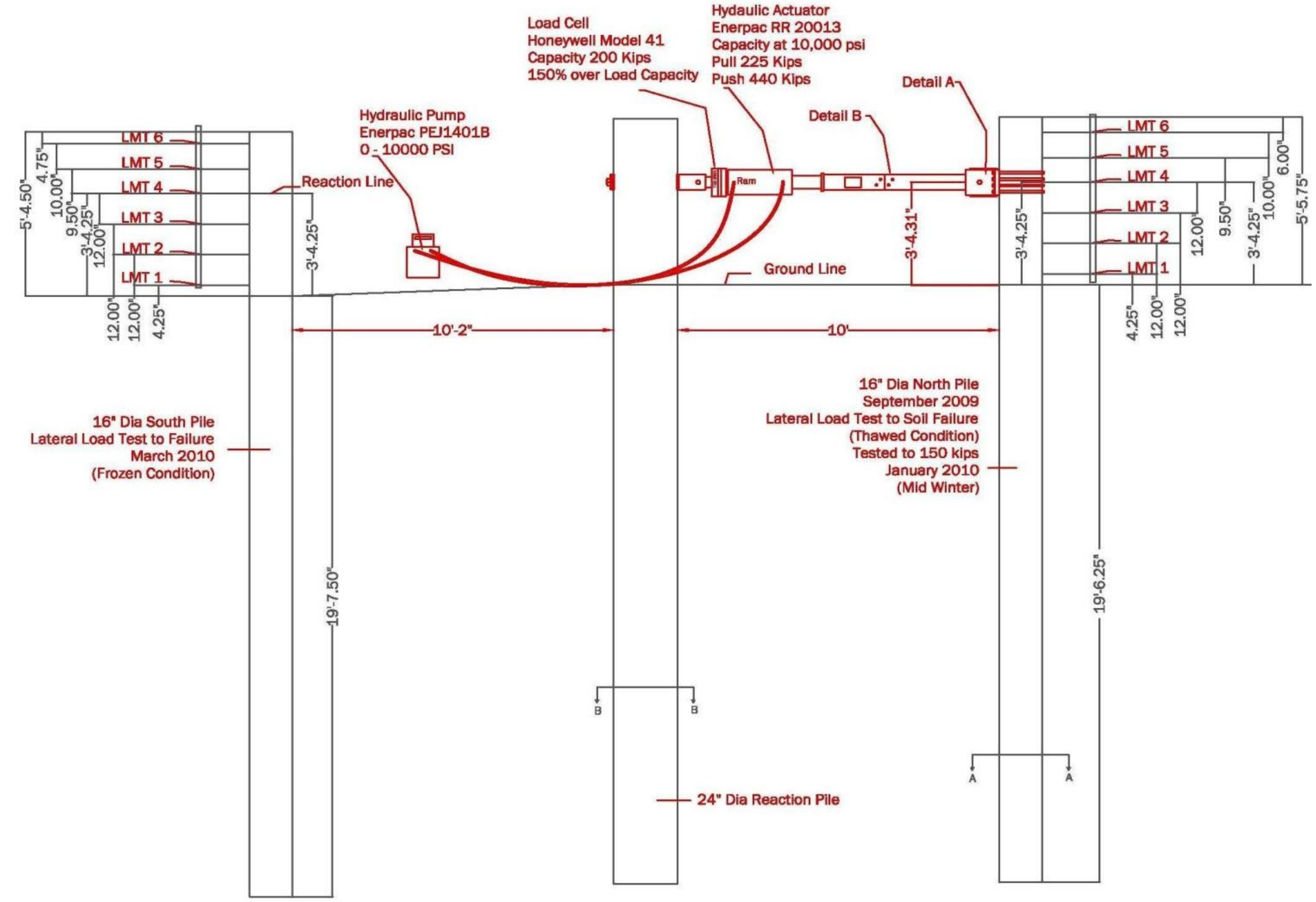

Figure 2.17: Test frame overview.

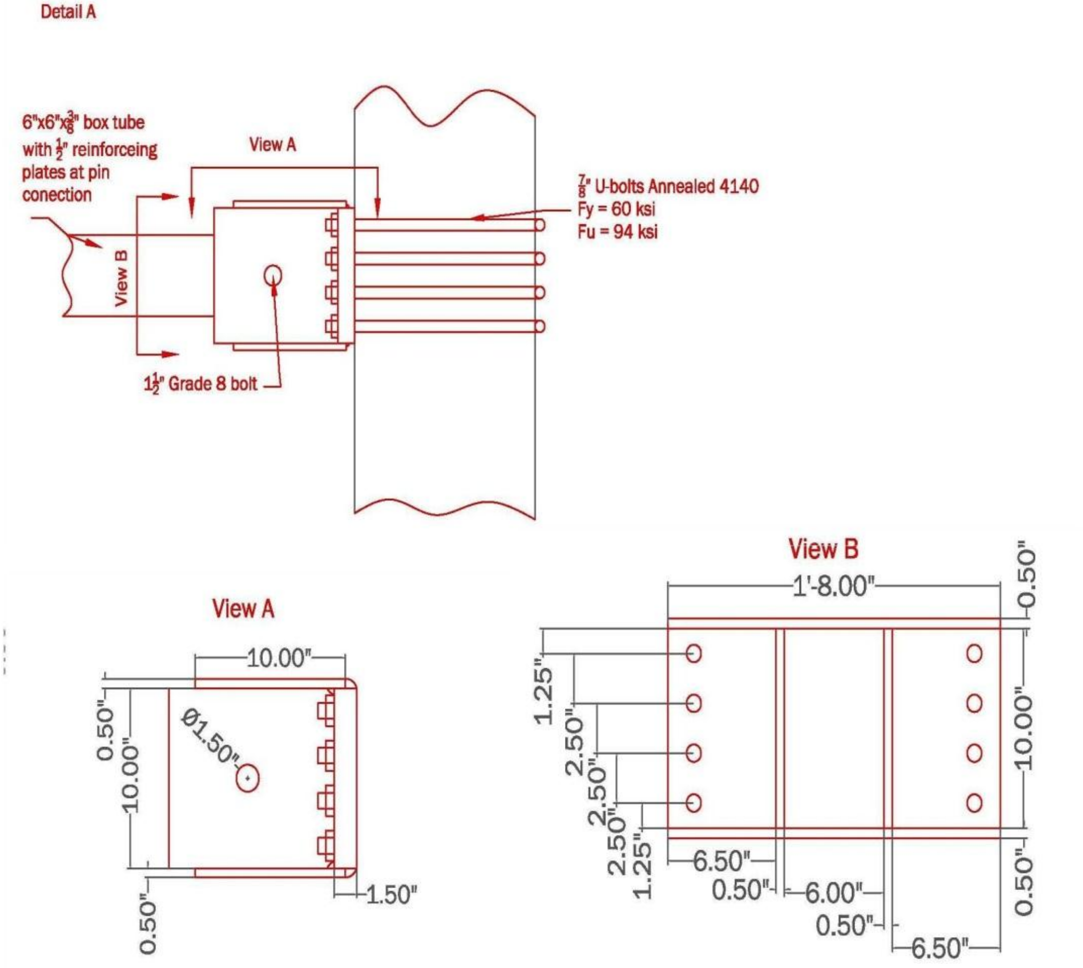

Figure 2.18: Test pile connection detail.

2.7.6 Quasi-static lateral-load pile testing

2.7.6.1 September testing

On September 19, 2009, we tested the north test pile. The weather was overcast and calm; the air temperature ranged between 45°F and 55°F. Displacement control was used throughout the test, with target displacement taken at the elevation of the ram. The first target displacement was 0.15 inch. Successive target displacements were 1.5 times the previous until 2.4 inches. Successive target displacements were 1.25 times the previous. Target displacements shown in Figure 2.13 were used for the test, with the pile pushed back into the upright position after each load cycle. Before testing began, we zeroed all instrumentation by taking an average reading in the unloaded condition and subtracting it from the gage reading. Shortly after testing began, we determined that data were not being collected. This was at the third displacement increment (increment 0.37 inch). At this point, we unloaded, re-zeroed, and started testing again. After the first few cycles, the pile was held in place for a period of at least 30 seconds. This was done in an attempt to give the inclinometer sufficient time to measure and record the centerline deflection of the pile (see Figure 2.19 for cyclic load versus deformation at the point of loading). Testing was stopped when the ram stroke reached maximum; this corresponded to a displacement of 5.7 inches for the test pile. During the test, both the test pile and the reaction pile displaced. Essentially, the reaction pile moved farther than the test pile. Failure occurred in the soil, with no visual signs of yielding of the test pile. See Figures 2.20 and 2.21 for September's final load test cycle. The soil gap formed in front of the pile is shown and quantified in Figure 2.22.

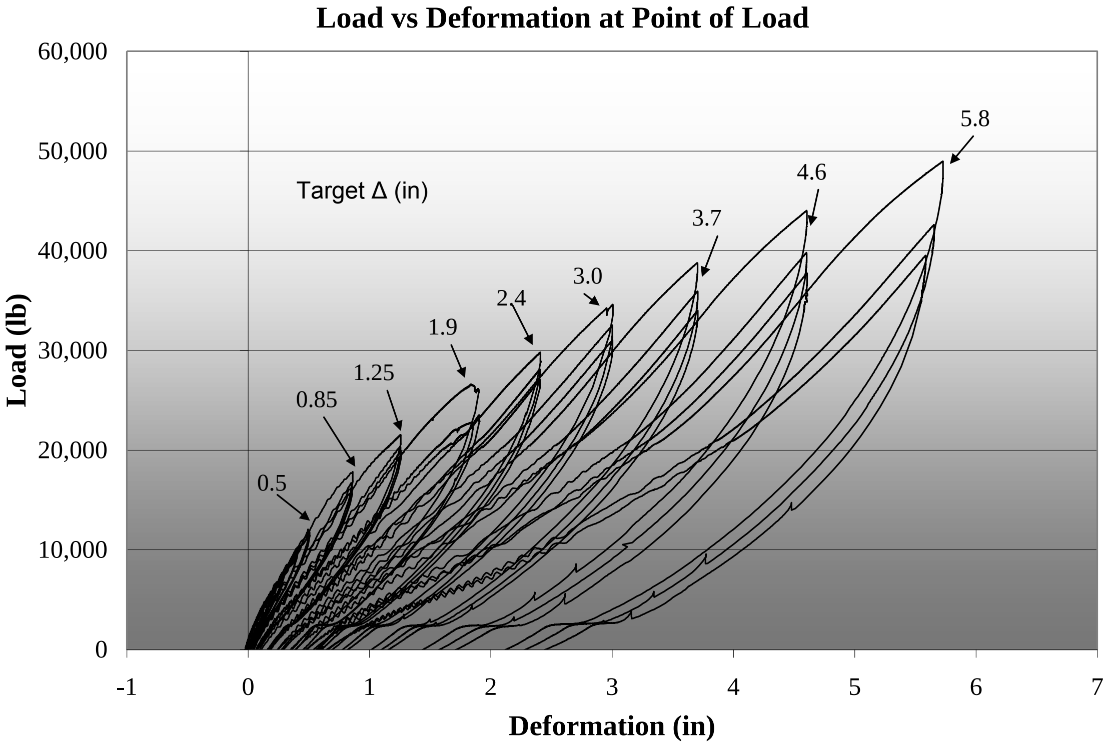

Figure 2.19: September cyclic load vs. deformation at point of load.

Figure 2.20: Test pile at final September load increment.

Figure 2.21: Reaction pile at final September load increment.

Figure 2.22: Plastically deformed soil; test pile after final loading and unloading.

2.7.6.2 Pile rehabilitation (September 2009)

In September 2009, we performed the first cyclic laterally loaded pile test. This test was conducted on the north 16-inch-diameter steel-jacketed reinforced concrete test pile. Test loads were applied using displacement control as the criteria for each load increment. During testing, load was applied by pulling the test pile toward the reaction pile until the desired deflection was reached. This step was followed by pushing against the reaction pile until displacement was zero. This procedure, which was considered a cycle, was repeated three times.

At the next load step, load was applied until displacement at the load cell reached the next target displacement (see Figure 2.13). This procedure continued until failure. In the case of the September test, the soil deformed to the point that ram stroke was exhausted. Failure occurred in the soil, and the structural capacity of the pile was not reached. After the test, the pile was returned to a vertical position and held there until the soil around the pile relaxed and the pile stayed vertical without any applied lateral load. We decided that it would be beneficial to test this pile again when seasonal frost was at approximately half of full frost depth.

The soil surrounding the pile after the fall test was plastically deformed, and a gap formed between the soil and the pile (see Figure 2.22). At the recommendation of the principal investigator and with the approval of ADOT&PF Bridge Design and the funding agencies, sand was placed in the gap and a pencil vibrator was used to liquefy the soil close to the ground surface until the sand was vibrated to completely fill the gap. The extent of this liquefaction of the soil affected approximately 6 inches of soil perpendicular to the front of the pile and 6 feet below the ground surface.

2.7.6.3 Snow conditions at the test site

In order to obtain maximum frost depth at the test site, snow was removed from around the south pile. A review of the literature revealed that if snow were removed from around the test pile for a radius of approximately 10 feet, frost would penetrate evenly around the test pile (Nicholson and Granberg 1973). Snow was removed after snow depth reached 4 inches, and was left undisturbed around the north pile to insulate the ground surface and keep frost depth to a minimum. Assuming winter conditions similar to that described by the 2008–2009 frost data and with snow cover left in place, we estimated depth of frost around the pile at 6 to 8 feet.

2.7.6.4 January testing

The January test was performed on the rehabilitated north test pile. In the beginning of the month, frost depth was just over 3 feet at the test site. Snow was removed from around the north test pile, and testing began on January 6, 2010. Displacement control was used initially, but when loads spiked to almost 50% of the yield strength of the pile before the first target deflection of 0.15 inch was reached, it became clear that displacement control would not work for winter testing. Testing was stopped, and a load-control test plan was developed.

The load plan for January testing was as follows: The first target load was 5 kips (the limiting value used for small displacement vibration testing). Successive target loads were 1.5 times the previous load until 50 kips; then successive target loads were 1.25 times the previous load (see Figure 2.14 for the loading schedule used for the January test).

Before testing was resumed, we reviewed data from the first cycle to make sure all readings were within a reasonable range. We gathered off-scale strain readings for approximately half of the strain gages during initial testing. Testing was stopped at this point, and several days passed before the problem was corrected. During this time, temperatures plunged to well below -40°F. Based on past experience with equipment operation in extremely cold weather, we decided to delay testing until the daily low temperature was above -20°F.

The test results for January 6 revealed that the pile in the frozen soil was stiff. A needle valve had to be added between the hydraulic pump and the cylinder so that the speed of the cylinder could be slowed to provide for accurate and achievable load steps. We estimated that the load rate for the January pile test did not exceed 1 inch/minute (0.0423 cm/sec).

On January 18, 2010, testing resumed on the north test pile. The weather was sunny and calm. Temperatures during testing ranged from -20°F to -9°F. During the 12 days between January 6 and January 18, the weather was extremely cold. With the protective snow cover removed, frost depth next to the north test pile increased to nearly 4.5 feet (see Figure 2.23).

The increase in pile stiffness from the unfrozen condition during the September test to the frozen condition of the January test was substantial. During January's test, the pile was loaded to 120 kips—the design capacity of the test frame—without any apparent yielding of the test pile and without the formation of a gap between the pile and the soil. Since none of the components of the test frame showed signs of failure and the frame had a factor of safety, we decided to load the pile to 150 kips, 30 kips beyond the design limit of the test frame. At this increased load, the connection to the reaction pile and the concrete under the jacket of the reaction pile crushed (see Figure 2.24). We stopped loading for the mid-winter test at this point, and the remaining two test cycles at 150 kips were unable to be completed. Load versus cyclic deformation is presented in Figure 2.25. A small amount of plastic deformation occurred during the 120-kip and 150-kip load increments.

A small crack in the soil at the base of the pile formed at the 150-kip load increment (see Figure 2.26), but it was less than 1/32 of an inch. No other soil cracking at the base of the pile was noticed.

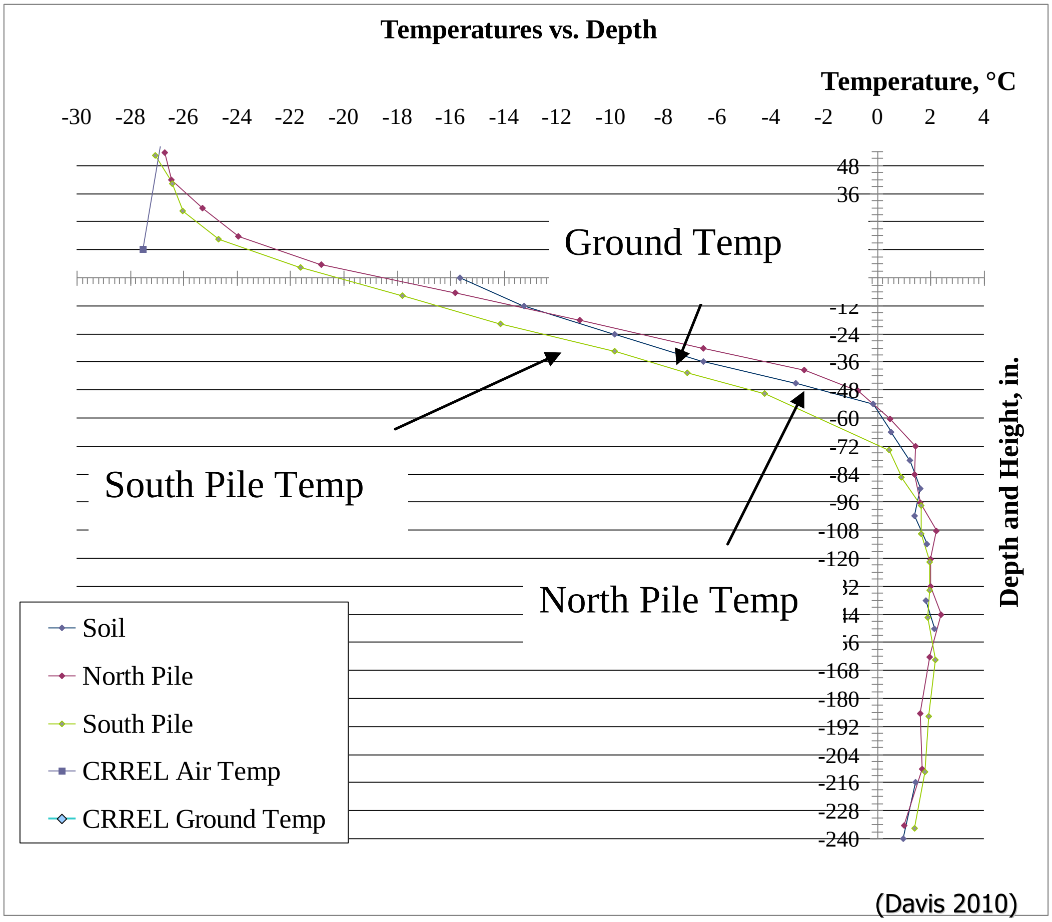

Figure 2.23: Temperatures with depth January 18, 2010.

Figure 2.24: Bearing failure of test frame at reaction pile.

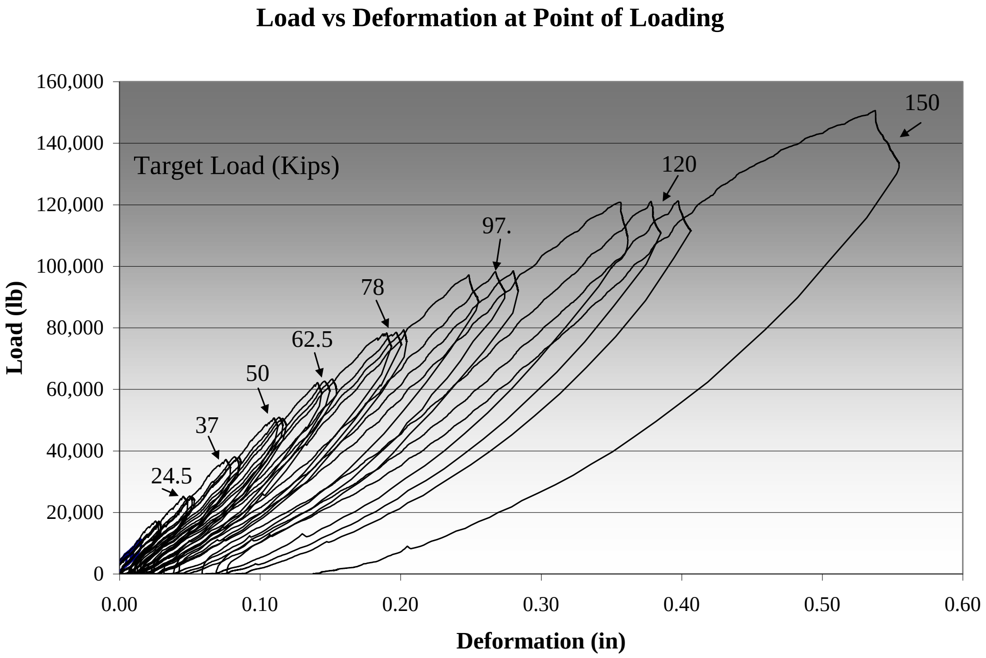

Figure 2.25: January cyclic load vs. deformation at point of load.

Figure 2.26: Soil crack at 150 kips, January test.

2.7.6.5 Test frame redesign

During testing in January 2010, the 120-kip capacity of the test frame was insufficient to fail the pile in the frozen condition. After the January 2010 test, the system was reevaluated using LRFD (load and resistance factor design) methods, with a design factor of safety of 1.0. Since the spring test was going to be the last pile test and the frame would not be needed for future testing, we determined that it was acceptable for parts of the test frame to go into plastic deformation. Modifications of the test frame were limited to increasing the bearing surface at the hinge on the test pile side of the reaction frame and increasing the size of the bearing plate at the reaction pile. With these modifications, the frame's capacity was raised to 226 kips, the maximum capacity of the hydraulic loading cylinder. No changes were made to the test pile/load frame interface.

2.7.6.6 March testing

On March 24, 2010, the south pile was tested. The weather was sunny with a slight breeze. Site temperatures ranged from 19°F to 25°F. The test equipment was set up the night before, and testing of the pile began around 1 p.m. The load plan for March testing was based on load control, with the following plan: The first target load was 5 kips; successive target loads were 1.5 times the previous load until 50 kips; and successive target loads were 1.25 times the previous load (see 2.7.3 for the loading schedule used for the March test). On test day, approximately 90 inches of frost were recorded (see Figure 2.27).

During the initial stages of loading (load steps below 50 kips), loading speed was reduced with a needle valve. The hydraulic pump pulsed, and the needle valve slowed the rate at which fluid flowed into the ram. For loads above 62 kips, the needle valve was not used, and it is reasonable to assume the rate of loading at the ram was nearly equal to the flow volume of the pump divided by the effective area of the ram, or about 1 inch/minute (0.0423 cm/sec). This assumption, which neglected movement of the reaction pile, is a reasonable estimate of the speed at which the pile was loaded.

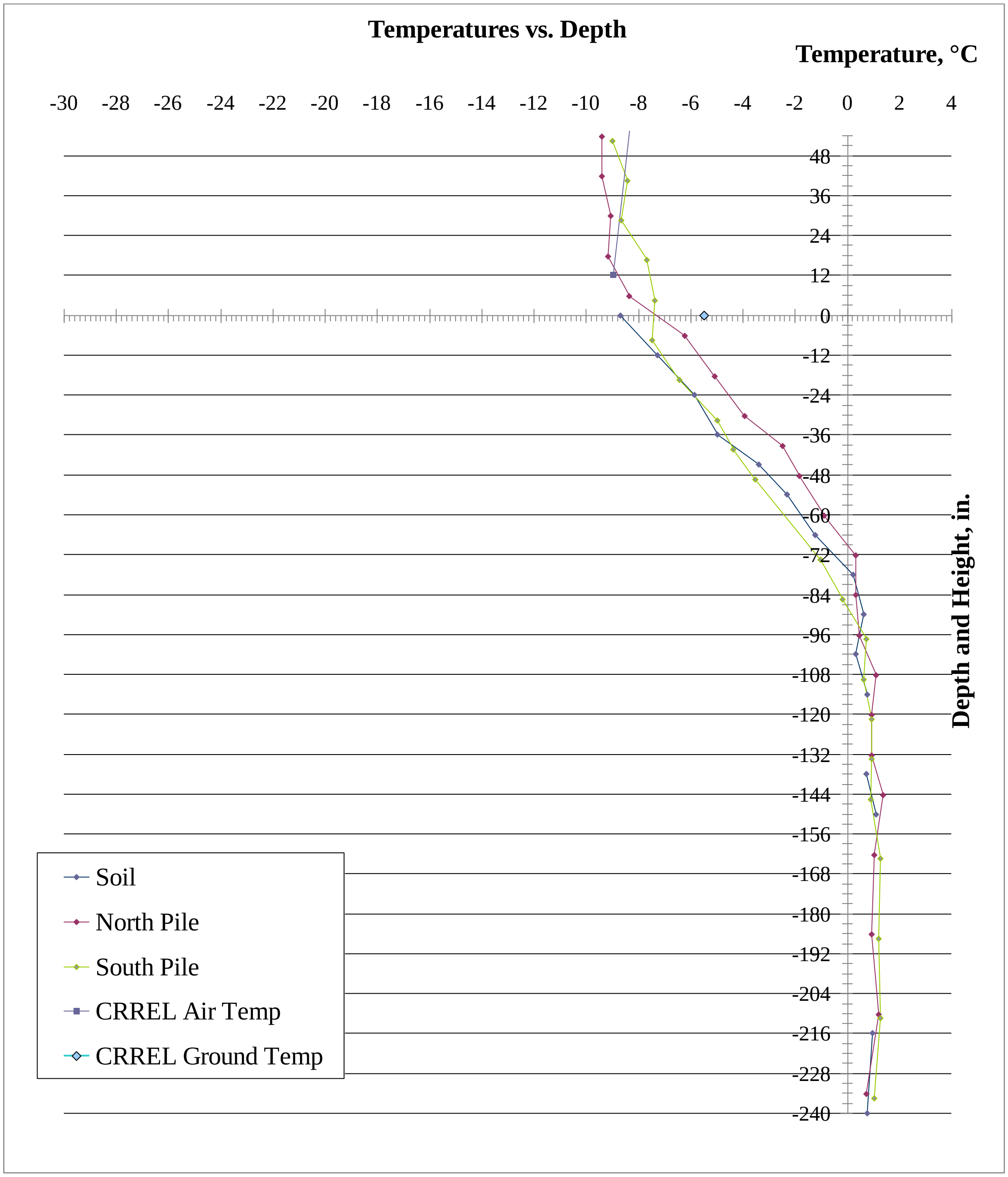

Figure 2.27: Temperatures with depth March 24, 2010.

A cracking noise of the concrete started at 50 kips and gradually increased throughout the test. Plastic deformation was noticeable above 120 kips. Figure 2.28 shows load-deformation behavior of the pile throughout the entire test, and Figure 2.29 shows the cyclic behavior of the pile at low deformations. Once large plastic deformation started to occur above 160 kips of load, cracking/popping noises began to increase rapidly. We theorized that the noise was caused by de-bonding between the steel and the concrete inside the pile, though this theory could not be proven without investigating the condition of the materials inside the pile. As plastic deformation of the pile started to take place during the first cycle of the 187-kip load increment, the amount of energy it took to load the pile increased. For the second and third cycles at the 187-kip load increment, plastic deformation had already occurred, and increased deformation was smaller at these cycles (see Figure 2.28). During the first cycle at the 226-kip load step, pile plastic deformation continued. The hydraulic pump overheated at approximately 199 kips, and loading for that cycle was stopped. The strain gage at 6.25 inches below ground surface on the tension side of the pile went off-scale due to strain readings over 28,000 micro strain. On the second cycle at the 226-kip load step, rotation of a plastic hinge formed just below the ground surface. This plastic hinge became so extreme that the pile tilted at an angle over 12 degrees. At 207 kips, the U-bolts holding the hinge onto the test pile slipped up the pile (see Figure 2.30). We stopped testing at this point, and a third cycle at 226 kips was not completed. The soil gap in front of the pile, in the unloaded condition after the 207-kip load step, was quantified (see Figure 2.31).

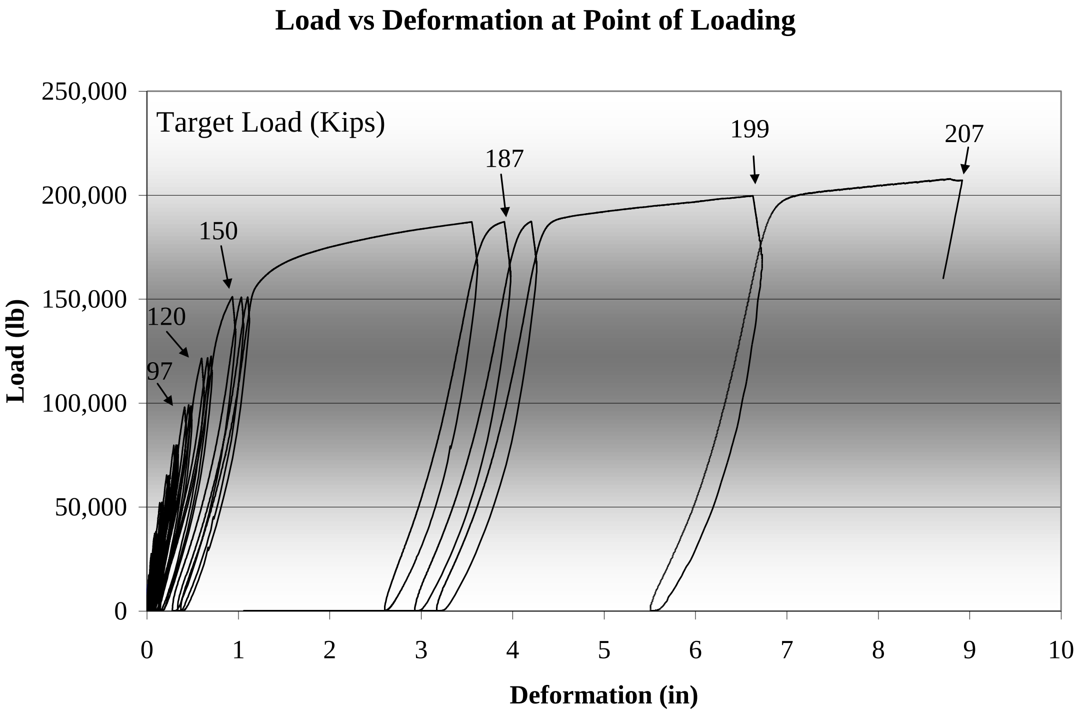

Figure 2.28: March cyclic load vs. deformation at point of load 0 to 207 kips.

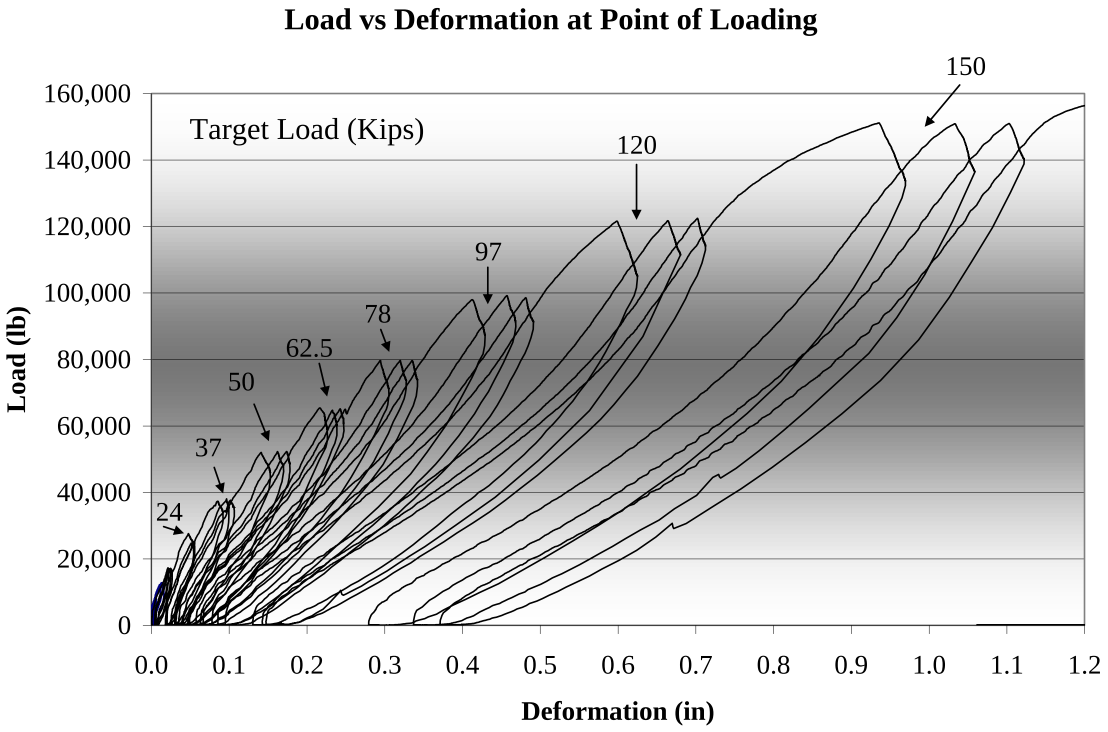

Figure 2.29: March cyclic load vs. deformation at point of load 0 to 150 kips.

Figure 2.30: At 207 kips, final loading of the south pile.

Figure 2.31: At 207 kips, unloaded plastically deformed soil gap in front of the test pile.

2.7.6.7 Formation of soil gap

The estimated gap left by plastic deformation of the soil is summarized in Figure 2.32 and Figure 2.33 for September and March, respectively. Figure 2.34 is a diagram of measurement locations. During March testing, several tension cracks were formed. This cracking is summarized in Figure 2.35. The gap formed in January testing was not summarized, as it was insignificant.

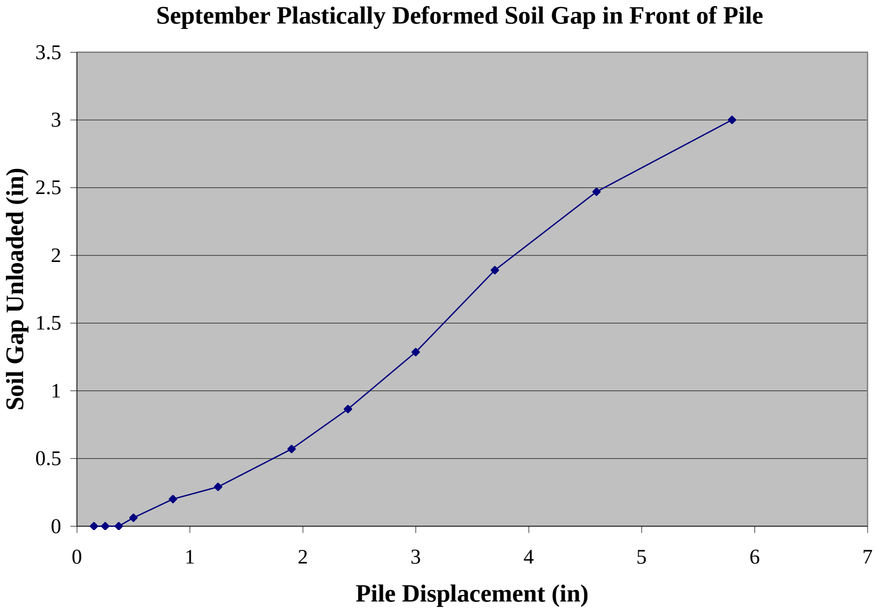

Figure 2.32: Plastically deformed soil gap in front of pile, September test.

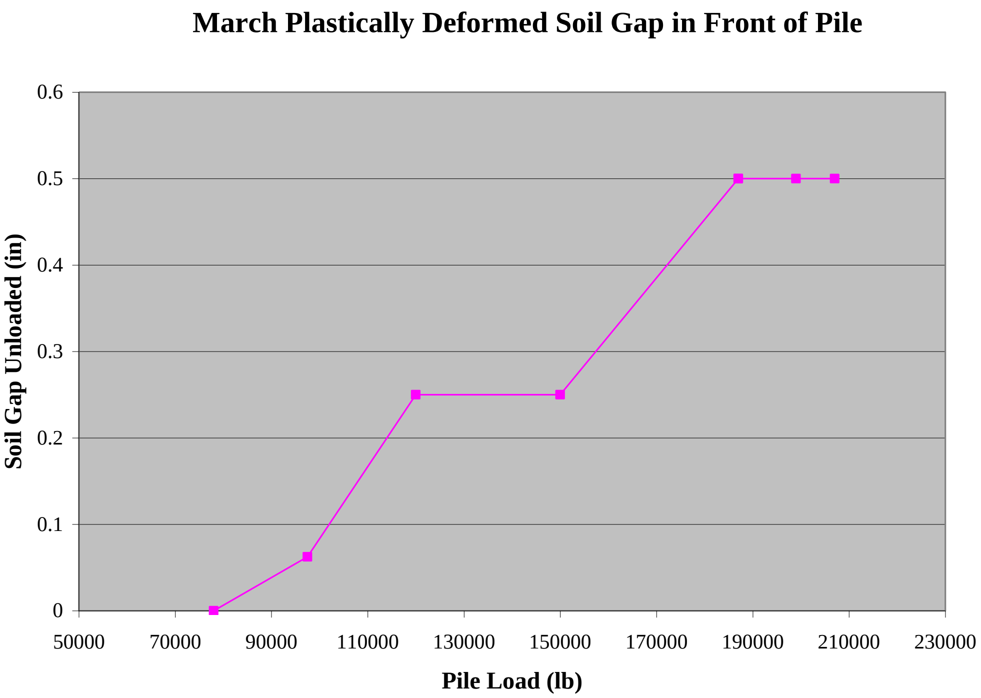

Figure 2.33: Plastically deformed soil gap in front of pile, March test.

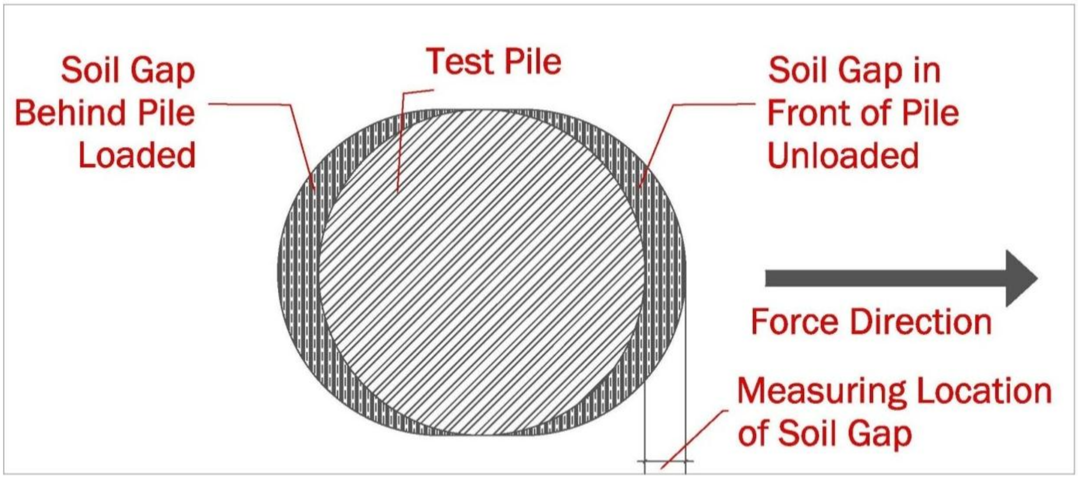

Figure 2.34: Soil gap location.

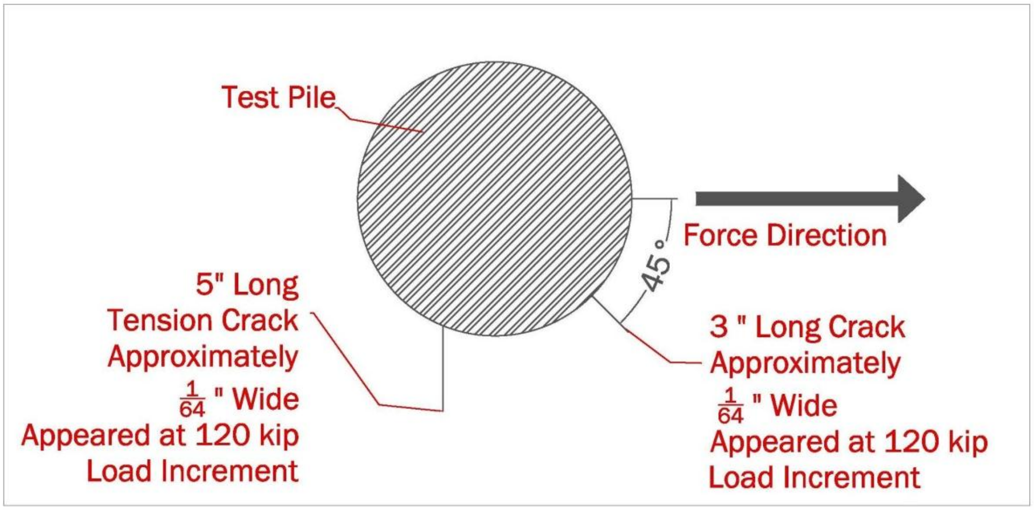

Figure 2.35: March soil cracking summarized.

2.8 Experimental Results and Data Analysis for Test Type 1 – Vibration Testing

Consider that a single pile is vertically embedded in the ground and we wish to measure its stiffness change as a function of seasonal conditions. This is a highly complex problem, in that stiffness is a function of the structural materials, soil type, soil densification, moisture, and ground temperature. A simple approximation for this complex problem is often used in design. For example, assume an equivalent fixed-free cantilever beam has the same stiffness as the soil–pile system (see Figure 2.36.

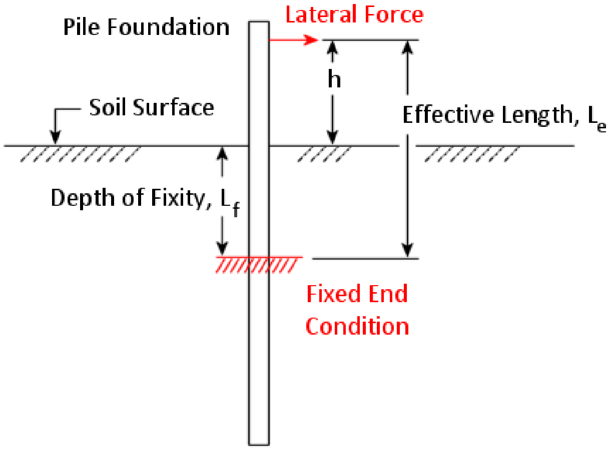

Figure 2.36: Effective length and depth of fixity definition (sketch).

Based on this idea and assuming a linear elastic, homogenous isotropic system in which plane sections before bending remain plane after bending, static deformation at the position of a statically load may be calculated as

$$\delta = \frac{PL_e^3}{3EI} \tag{2.1}$$

where δ is the amount of displacement of the beam at the point of load application, P is the magnitude of the transverse load, EI is the beam's flexural stiffness, and L_e is the length from the point of load application to the fixed end.

If the system is nonlinear, than the relationship between load and displacement may be expressed by

$$P = k\delta \tag{2.2}$$

where δ is displacement, k is the coefficient of stiffness, and P is the applied load.

If load, displacement at the load, and flexural stiffness of the beam are known (either directly measured or calculated from geometric and component material properties), then the effective length may be determined by combining Equations (2.1) and (2.2) giving

$$L_e = \sqrt[3]{\frac{3EI}{k}} \tag{2.3}$$

The free-vibration response for a fixed-free (cantilever beam) distributed mass model is given by (Palm 2007)

$$f_1 = \frac{3.516}{2\pi L_e^2}\sqrt{\frac{EI}{m}} \tag{2.4}$$

where f_1 is the frequency of the first mode of vibration (Hz), L_e is effective length of the cantilever member, EI is the member's flexural stiffness, and m is the member's mass per unit length.

2.8.1 Temperature

Temperatures were taken at discrete points along the length of the test pile. Temperature values are shown in Table 2.3 and Table 2.4, as the depths of the top and bottom of the seasonally frozen layer are linear interpolations between those points.

Table 2.3: South Pile Depths of Seasonally Frozen Soil Boundaries

	Top	Bottom	Soil Surface Temperature	
Test Date	(in.)	(in.)	(°F)	(°C)
4/16/2009	5.9	92.6	32.72	0.4
4/20/2009	10.1	91.1	33.62	0.9
4/27/2009	21.1	97	41.9	5.5
5/5/2009	35.6	93.7	42.98	6.1
5/12/2009	37.9	93.7	42.26	5.7
5/19/2009	46.2	97.6	54.5	12.5
5/26/2009	59.9	100.9 (note a)	65.48	18.6
6/2/2009	74.2	100.6 (note b)	61.16	16.2
6/16/2009	81.5	100.6 (note c)	69.8	21
7/16/2009	n/a	n/a	66.2	19
7/21/2009	239.2	n/a	72.68	22.6
9/18/2009	n/a	n/a	51.62	10.9
1/22/2010	0	77	1.94	-16.7
1/29/2010	0	80.1	5	-15
2/5/2010	0	83.7	-9.04	-22.8
3/8/2010	0	89.3	8.42	-13.1
3/23/2010	0	92.8	22.64	-5.2

Notes:

a) also from 119.9 to 128.6, and 239.3+
b) also from 122.8 to 127.1
c) also from 119.9 to 129.0, and 239.3+

Table 2.4: North Pile Depths of Seasonally Frozen Soil Boundaries

	Top	Bottom	Soil Surface Temperature	
Test Date	(in.)	(in.)	(°F)	(°C)
4/16/2009	---	---	---	---
4/20/2009	8.1	87.2	32.54	0.3
4/27/2009	22.7	99.2	39.56	4.2
5/5/2009	38.2	93.2	41.72	5.4
5/12/2009	40.5	99.2	39.56	4.2
5/19/2009	50.3	104.1	49.28	9.6
5/26/2009	58.9	112.1 (note a)	59.54	15.3
6/2/2009	64	112.1 (note a)	57.2	14
6/16/2009	---	---	---	---
7/16/2009	n/a	n/a	59.54	15.3
7/21/2009	227.8	n/a	64.94	18.3
9/18/2009	n/a	n/a	n/a	n/a
1/22/2010	---	---	---	---
1/29/2010	---	---	---	---
2/5/2010	---	---	---	---
3/8/2010	---	---	---	---
3/23/2010	---	---	---	---

Note (a): also from 134.8 to 139.3, from 188.8 to 196.2, and 235.8+

2.8.2 Load Deflection

Tables 2.5 and 2.6 show the calculated values of effective length and depth of fixity for each pile that was tested. Each pile test is listed by date, for a 5,000-pound reference load. On each date of testing, we conducted a number of tests on each pile. The values shown in the tables are minimum, maximum, and average values of those sets of tests.

No load-deflection tests were performed on the north pile or the reaction pile after September 18, 2009. Shortly after that date, those piles underwent large displacement tests as part of the second type of tests, and subsequently, the piles were significantly altered.

Depth of fixity for the south test pile appeared to correlate with the top of the seasonal frost layer (see Figure 2.37). Slopes of the linear regressions for depth of fixity and the top of the seasonally frozen layer are similar. Depth of fixity for the series of tests, where the soil was frozen to a significant depth, did not appear to change, and for these conditions, the top of the seasonally frozen soil layer is the top of the soil. However, a distinct difference was apparent in the depth of fixity relative to the top of the seasonally frozen soil layer while freezing rather than while thawing (i.e., 5 to 6 inches compared with 24 to 27 inches). This difference is likely due to the presence of frozen and unfrozen moisture content near the boundaries of the frozen layer, and the negligible amount of unfrozen moisture content in the frozen soil.

Table 2.5: South and North Pile Effective Lengths and Depth of Fixity

Test Date	South Pile						North Pile					
	Effective Length (in.)			Depth of Fixity (in.)			Effective Length (in.)			Depth of Fixity (in.)		
	Min.	Max.	Avg.	Min.	Max.	Avg.	Min.	Max.	Avg.	Min.	Max.	Avg.
4/16/2009	79.1	81.2	80.1	26.6	28.6	27.6	---	---	---	---	---	---
4/20/2009	84.3	84.9	84.6	31.8	32.4	32.1	92.8	95.9	94.0	36.4	39.5	37.6
4/27/2009	96.1	96.3	96.2	43.1	43.3	43.2	105.4	105.7	105.6	48.5	48.9	48.7
5/5/2009	115.0	119.5	117.2	61.4	65.9	63.7	122.6	124.8	123.4	65.2	67.4	66.1
5/12/2009	122.2	122.9	122.5	68.1	68.8	68.4	132.9	135.6	133.8	75.0	77.7	76.0
5/19/2009	131.4	135.6	133.2	76.7	81.0	78.6	139.9	142.2	141.2	81.5	83.8	82.9
5/26/2009	145.4	147.3	146.5	89.0	91.0	90.1	155.4	158.4	157.1	96.5	99.5	98.3
6/2/2009	150.7	154.0	152.4	93.8	97.1	95.5	158.2	163.2	160.8	97.8	102.8	100.5
6/16/2009	161.8	165.0	163.4	103.8	107.0	105.4	---	---	---	---	---	---
7/16/2009	146.6	153.0	150.5	87.8	94.2	91.7	153.3	154.7	153.9	94.9	96.3	95.5
7/21/2009	148.1	149.0	148.6	89.2	90.0	89.6	148.2	150.2	149.2	89.7	91.7	90.7
9/18/2009	152.0	152.9	152.4	91.8	93.9	92.9	157.7	159.0	158.5	98.9	100.1	99.7
1/22/2010	62.9	63.5	63.2	4.5	5.2	4.9						
1/29/2010	63.3	63.6	63.4	5.0	5.3	5.1						
2/5/2010	63.3	63.7	63.5	5.0	5.4	5.2						
3/8/2010	63.8	64.8	64.3	5.5	6.5	6.0						
3/23/2010	62.6	65.2	64.3	4.3	6.9	6.0						

Depths of fixity for the tests conducted on June 2, 2009, and June 16, 2009, are noteworthy because they appear to be deeper than the depths of fixity for the tests in unfrozen soil, by as much as 15 inches. The points that indicate the top and bottom of the seasonally frozen soil layer are the boundaries at which the soil becomes temperature-dependent.

Table 2.6: Reaction Pile Effective Lengths and Depths of Fixity

	Effective Length (in.)			Depth of Fixity (in.)		
Test Date	Min.	Max.	Avg.	Min.	Max.	Avg.
4/16/2009	---	---	---	---	---	---
4/20/2009	105.7	108.1	106.7	47.4	49.8	48.5
4/27/2009	118.3	119.7	119.2	59.5	61.0	60.5
5/5/2009	137.7	145.5	142.1	77.5	85.4	82.0
5/12/2009	148.6	153.2	150.2	87.7	92.3	89.3
5/19/2009	158.9	163.9	161.2	97.3	102.3	99.6
5/26/2009	178.0	180.8	179.4	115.7	118.6	117.1
6/2/2009	187.1	187.9	187.6	124.3	125.2	124.8
6/16/2009	---	---	---	---	---	---
7/16/2009	176.6	178.1	177.2	116.2	117.7	116.8
7/21/2009	---	---	---	---	---	---
9/18/2009	186.1	189.2	187.5	125.8	128.8	127.1

Note: --- indicates no test data were taken on that date

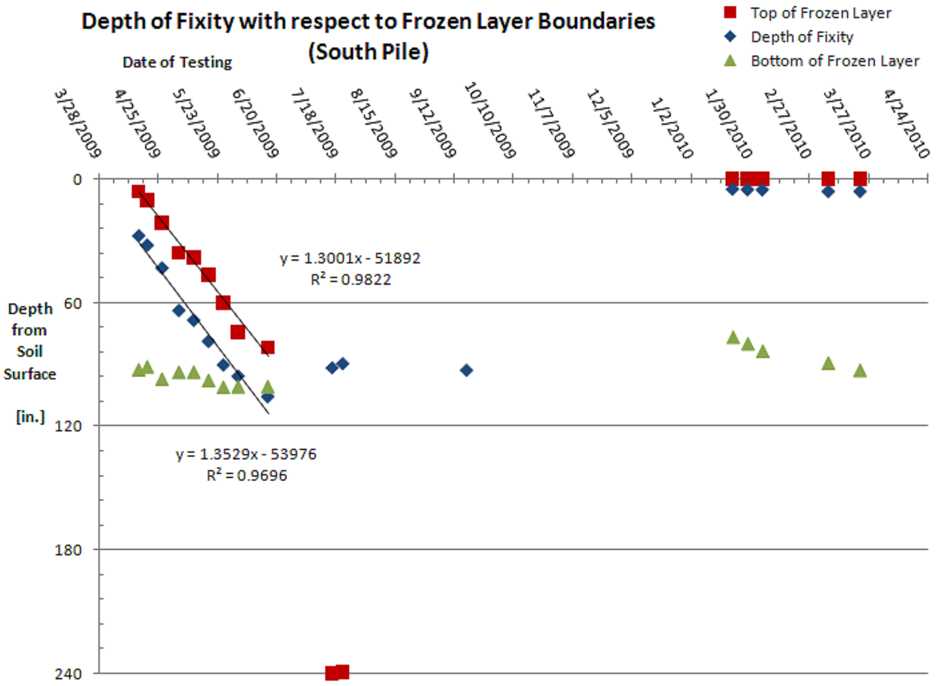

Figure 2.37: South pile depth of fixity compared with depth of seasonally frozen soil.

Similar results were obtained from tests on the north pile (see Figure 2.38). The slope of the linear regression through the depth-of-fixity points is slightly steeper than the slope of the linear regression through the top boundary of the frozen layer (i.e., 1.52 compared with 1.26). Soil composition at the surface of the north pile is slightly different from that of the south pile. During soil borehole testing and soil logging, the top meter of soil surrounding the south pile contained significant amounts of gravel; the soil surrounding the north pile contained silt with thin organic layers. The difference in soil composition near the surface at each pile probably accounts for differences in structure–soil interaction and, hence, the depth of fixity. The lack of gravel around the north pile would make that soil less stiff, and thus tend toward deeper depths of fixity, compared with the soil around the south pile.

Similar to the south pile, the depths of fixity for the tests conducted May 26, 2009, and June 2, 2009, appear deeper than the depths of fixity for tests conducted in unfrozen soil. Based on test-pile temperature readings, the transition between frozen and unfrozen soil for both the south pile and the north pile was not clearly defined.

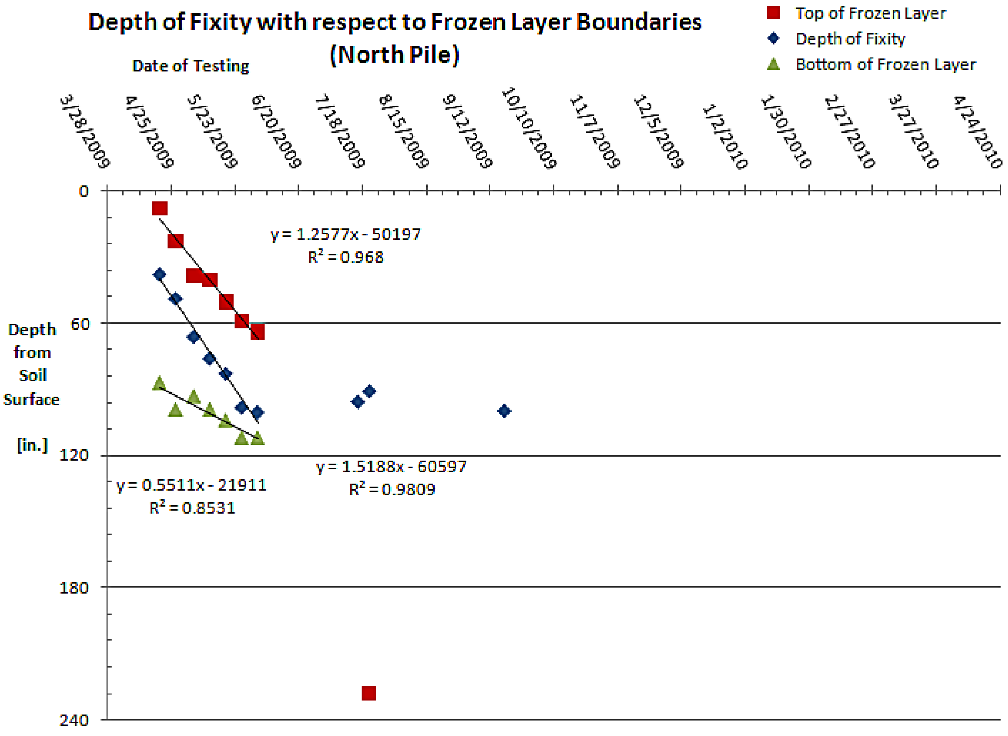

Figure 2.38: North pile depth of fixity compared with depth of seasonally frozen soil.

2.8.3 Reinforcing bar strain

Depths to maximum strain for the south pile are significantly different for the soil in frozen and unfrozen conditions (see Figure 2.39). Strain gages were placed at discrete points, spaced at 12-inch intervals, along the "A" reinforcing bar. The depth of maximum strain, and hence the maximum moment, was between 48 and 60 inches deep for piles embedded in unfrozen soil. The depth of maximum strain for the south pile embedded in frozen soil was near the surface. In general, the depths of maximum strain, and hence maximum moment, are the locations where plastic hinges are expected to develop. The maximum strains for piles embedded in frozen soil are expected to be nearer to the soil surface, and the magnitude of strain is less for a given load than for piles embedded in unfrozen soils.

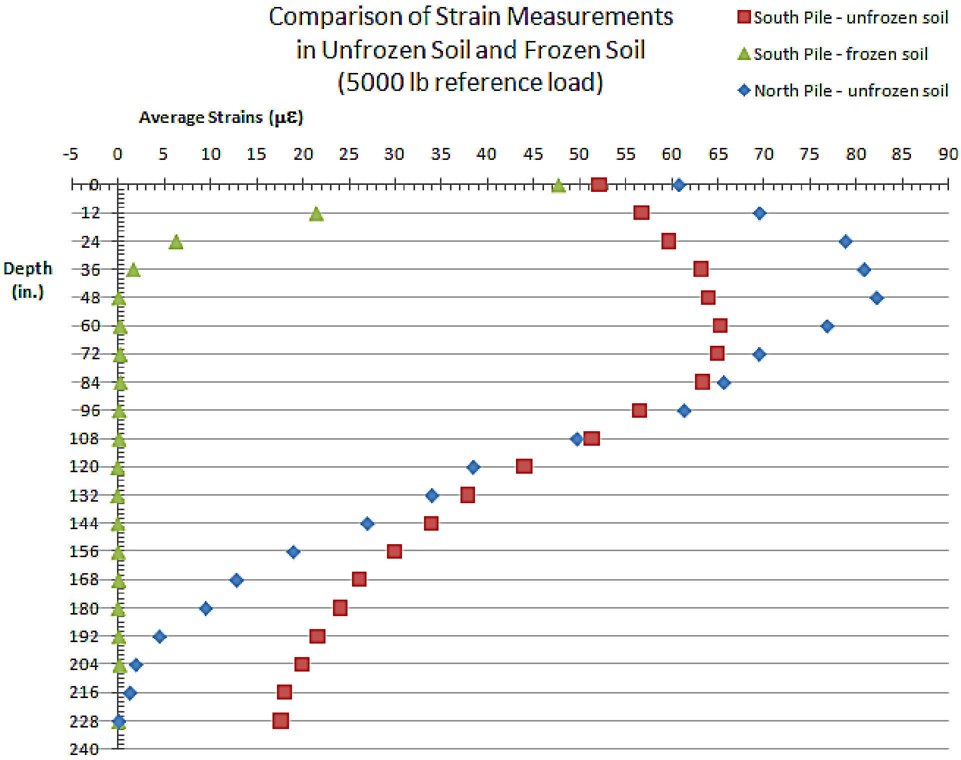

Figure 2.39: Comparison of strain distribution between frozen and unfrozen soils.

For this part of the study (small displacement vibrational response), we assumed that the laterally applied loads were small enough that the concrete making up the pile would not crack. In the calculations to estimate the pile's flexural stiffness, the concrete-cracking strain was found to be 1.81×10^{-4} in./in. If the depth-to-maximum moment in unfrozen soil is 60 inches and the height of the applied load is 64 inches above the soil surface (total of 124 inches from the point-of-load application to the point of maximum moment), then the amount of applied load that would cause the concrete to crack would be 5,414 pounds, which is greater than the reference load of 5,000 pounds. Similarly, if the maximum moment in frozen soil is at the soil surface and the height of the applied load is 64 inches above the soil surface (a total of 64 inches from the point-of-load application to the point of maximum moment), then the amount of applied load that would cause the concrete to crack would be 10,490 pounds.

2.8.4 Vibration

There appears to be a significant change in damped natural frequency of vibration between tests conducted in frozen and unfrozen soil. The frequency is higher and the effective length is shorter for a pile embedded in frozen soil than for a pile embedded in unfrozen soil.

For tests performed on the south pile embedded in unfrozen soil, damping displayed by the lower frequencies appeared linear and characteristic of Coulomb damping, while the higher frequencies appeared exponential and characteristic of viscous damping. In these tests, all frequencies in the spectrum were sensitive to boundary conditions for the differential equation of motion and to nonlinear structure–soil interaction. In all tests, no single frequency was dominant; instead, the response appeared to be multi-modal.

Depth of fixity values were evaluated for lateral static (load-deformation) tests and free vibration tests. These values are compared for the south pile, north pile, and the reaction pile for the test site (see Table 2.7).

While Figure 2.40 represents the correlation between effective lengths calculated from static and dynamic tests, it is useful to observe how the measured natural frequency and calculated effective lengths compare with theoretical values of the same, based on the beam’s estimated flexural stiffness. Figure 2.41 provides a comparison between calculated effective length for quasi-static load-deflection tests and measured damped natural frequency versus theoretical natural frequency. Theoretical natural frequency is based on Equation (2.4), using the calculated flexural stiffness values for the test piles and the reaction pile. The plot is useful for determining the quality of test results compared with theoretical values. The test results not only are similar between types of tests, but also correlate to their theoretical relationship.

Table 2.7: Depth of Fixity for 16" Piles and 24" Reaction Pile

		Static Tests			Dynamic Tests				
		Depth to fixity			Natural Frequency (Hz)		Depth to fixity (in)		
Test Date	Pile	Min. (in)	Max. (in)	# of Pile Dia(avg)	Min.	Max.	Min.	Max.	# of Pile Dia(avg)
4/16/2009	South	26.6	28.6	1.7	---	---	---	---	---
4/16/2009	North	---	---	---	---	---	---	---	---
4/16/2009	Reaction	---	---	---	---	---	---	---	---
4/20/2009	South	31.8	32.4	2.0	---	---	---	---	---
4/20/2009	North	36.4	39.5	2.4	---	---	---	---	---
4/20/2009	Reaction	47.4	49.8	2.0	---	---	---	---	---
4/27/2009	South	43.1	43.3	2.7	---	---	---	---	---
4/27/2009	North	48.5	48.9	3.0	---	---	---	---	---
4/27/2009	Reaction	59.5	61	2.5	---	---	---	---	---
5/5/2009	South	61.4	65.9	4.0	---	---	---	---	---
5/5/2009	North	65.2	67.4	4.1	---	---	---	---	---
5/5/2009	Reaction	77.5	85.4	3.4	---	---	---	---	---
5/12/2009	South	68.1	68.8	4.3	---	---	---	---	---
5/12/2009	North	75	77.7	4.8	---	---	---	---	---
5/12/2009	Reaction	87.7	92.3	3.8	---	---	---	---	---
5/19/2009	South	76.7	81	4.9	---	---	---	---	---
5/19/2009	North	81.5	83.8	5.2	---	---	---	---	---
5/19/2009	Reaction	97.3	102.3	4.2	---	---	---	---	---
5/26/2009	South	89	91	5.6	---	---	---	---	---
5/26/2009	North	96.5	99.5	6.1	---	---	---	---	---
5/26/2009	Reaction	115.7	118.6	4.9	---	---	---	---	---
6/2/2009	South	93.8	97.1	6.0	---	---	---	---	---
6/2/2009	North	97.8	102.8	6.3	---	---	---	---	---
6/2/2009	Reaction	124.3	125.2	5.2	---	---	---	---	---
6/16/2009	South	103.8	107	6.6	---	---	---	---	---
6/16/2009	North	---	---	---	---	---	---	---	---
6/16/2009	Reaction	---	---	---	---	---	---	---	---

7/16/2009	South	87.8	94.2	5.7	15.9	17.1	93.4	99.1	6.0
7/16/2009	North	94.9	96.3	6.0	15.9	16.5	96.6	98.1	6.1
7/16/2009	Reaction	116.2	117.7	4.9	15.9	16.5	124.7	127.7	5.3
7/21/2009	South	89.2	90	5.6	15.9	18.3	88.1	98.9	5.8
7/21/2009	North	89.7	91.7	5.7	13.4	16.5	96.5	109.4	6.4
7/21/2009	Reaction	---	---		---	---	---	---	---
9/18/2009	South	91.8	93.9	5.8	15.3	16.5	94.8	102	6.2
9/18/2009	North	98.9	100.1	6.2	12.2	14.6	105.6	121.2	7.1
9/18/2009	Reaction	125.8	128.8	8.0	14.6	16.5	124.8	135.9	8.1
1/22/2010	South	4.5	5.2	0.3	97	97.6	5.3	5.6	0.3
1/29/2010	South	5	5.3	0.3	96.4	97	5.6	5.8	0.4
2/5/2010	South	5	5.4	0.3	95.2	95.2	6.2	6.2	0.4
3/8/2010	South	5.5	6.5	0.4	95.2	95.2	6.2	6.2	0.4
3/23/2010	South	4.3	6.9	0.4	95.2	95.8	6.0	6.2	0.4

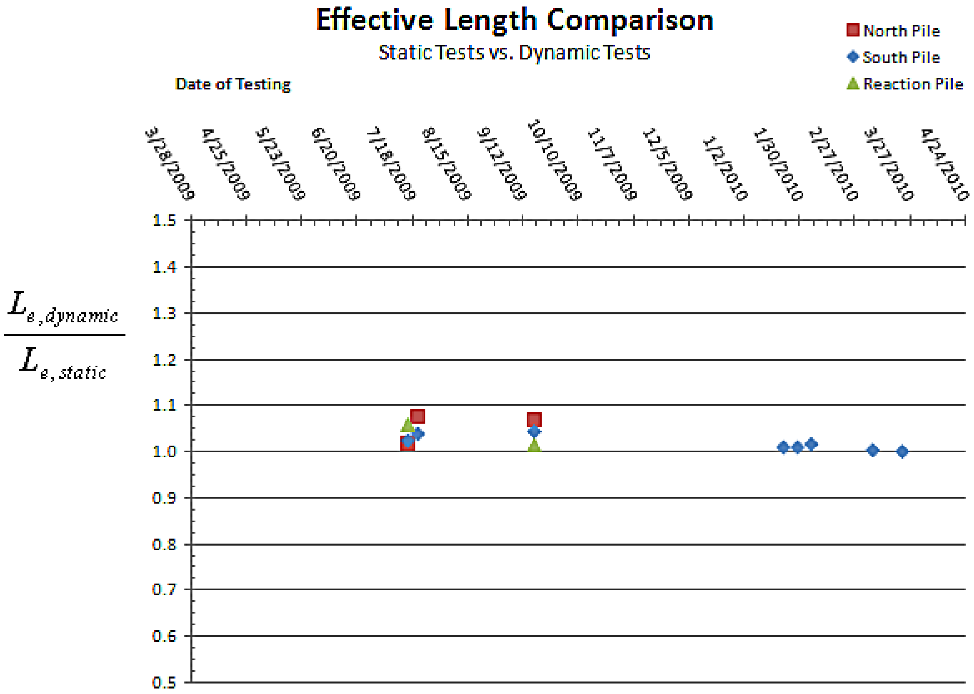

Figure 2.40: Comparison of effective length for static vs. dynamic test methods.

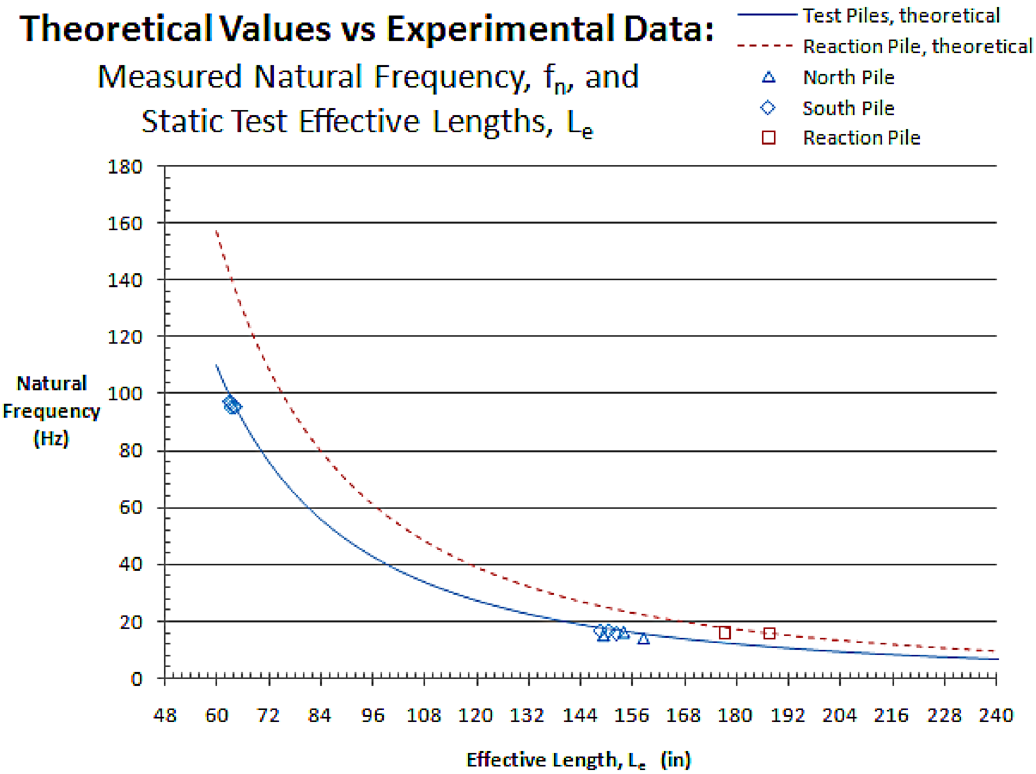

Figure 2.41: Comparison of empirical test results with theoretical test results.

The depth of fixity for the south test pile in frozen soil was approximately 6 inches; for the same pile in unfrozen soil, the depth of fixity was approximately 90 inches. On April 20, 2009, the soil around the south pile was thawed to a depth of approximately 10 inches, and the calculated depth of fixity in this condition was 32 inches; this depth of fixity is 35.1% of the average depth of fixity in unfrozen soil from tests conducted July 16, July 21, and September 18, 2009.

The depth of fixity for the north test pile in unfrozen soil was approximately 95 inches. Although not measured, the depth of fixity for the north test pile in frozen soil was expected to be similar to the depth of fixity of the south test pile in frozen soil. The two piles shared similar heat-transfer properties, and the only difference was the amount of gravel in the top meter of soil at the south test pile. On April 20, 2009, the soil around the north pile was thawed to a depth of approximately 8 inches, and the calculated depth of fixity in this condition was 37 inches. This depth of fixity is 39.4% of the average depth of fixity in unfrozen soil from tests conducted July 16, July 21, and September 18, 2009.

The depth of fixity for the reaction pile in unfrozen soil was approximately 122 inches. The depth of fixity for the reaction pile in frozen soil was not measured. The depth of thaw around the reaction pile also was not measured, but since the reaction pile had a greater surface area than that of the two test piles, the heat-transfer properties were expected to be different. On April 20, 2009, the calculated depth of fixity of the reaction pile was 48 inches, which was about 40% of the average depth of fixity for the conditions existing during the tests conducted July 16, and September 18, 2009.

The damped natural frequency of the south test pile when embedded in frozen soil was approximately 95 Hz; the damped natural frequency of the same pile when embedded in unfrozen soil was approximately 16 Hz. The damped natural frequency of the north test pile in unfrozen soil was approximately 15 Hz. Even though the flexural stiffness of the reaction pile was significantly greater than the flexural stiffness of the test piles, the damped natural frequency in unfrozen soil was approximately 16 Hz. The effective lengths calculated from these frequencies correlated to within 10% of the effective lengths calculated from the quasi-static lateral load tests. Calculated damped natural frequencies plotted with respect to calculated effective lengths from quasi-static lateral loads correlated to their theoretical relationship.

2.9 Type 2 Tests – Quasi-static Cyclic Loaded Pile Tests: Experimental Results

Tests results are presented for three different laterally loaded pile tests. Each test was conducted using cyclic quasi-static laterally applied loads to a 16-inch-diameter steel-jacketed reinforced concrete pile. The three tests were performed in September 2009 on the north pile (fall, fully thawed); January 2010 on the rehabilitated north pile (winter, frozen soils were 4.5 ft deep); and March 2010 on the south pile (spring, frozen soils were 7.5 ft deep).

Two analytical methods for evaluating the test results were requested by ADOT&PF. These methods were examined as part of the study of the experimental data. The first method is a simple, well-established method, based on the idea that this complicated problem can be simplified as a pile with a fixed end in the ground and a free end above the ground. In this method, the soil above the depth of equivalent fixity is neglected, and the soil below the depth of equivalent fixity is considered infinitely rigid (Coduto 2001). The second method is more complicated. This method is essentially a beam on elastic or inelastic foundation, where soil resistance is approximated by discretely spaced springs. For this analysis, LPile (Reese et al.

2004), a finite difference program, was used to develop soil springs for use in predicting the experimental pile deformations.

2.9.1 Material properties

2.9.1.1 Concrete strength

Compressive strength was obtained from uniaxial compression tests. This test, which conforms to ASTM C39 2005, was done 28 days after the pour. The average concrete compressive strength was 5,176 psi. The average secant modulus was 4,395,335 psi, the average chord modulus was 3,885,017 psi, and the ACI modified concrete modulus was 3,724,031 psi. The unit weight was 135 pcf, and the average tensile strength based on tests for modulus of rupture was 718 psi.

We chose the chord modulus as the elastic modulus. The expression relating stress, f_c, and strain, ε_{cf}, may be approximated (Collins and Mitchell 1991) by

$$\frac{f_c}{f'_c} = \frac{n(\varepsilon_{cf} / \varepsilon'_c)}{n - 1 + (\varepsilon_{cf} / \varepsilon'_c)^{nk}} \qquad (2.5)$$

where

f'_c = peak stress obtained from a cylinder test

ε'_c = strain when f_c reaches f'_c

n = curve-fitting factor equal to $(E_c/(E_c - E'_c)$

$E'_c = f'_c/\varepsilon'_c$

k = factor to increase the post-peak decay in stress, taken as 1.0 for $(\varepsilon_{cf}/\varepsilon'_c)$ less than 1.0 and as a number greater the 1.0 for $(\varepsilon_{cf}/\varepsilon'_c)$ greater then 1.0

The relationship between concrete stress-strain were approximated by

$$n = 0.8 + \frac{f'_c}{2500} \text{ (psi)} \qquad (2.6)$$

$$\varepsilon'_c = \frac{f'_c}{E_c} * \frac{n}{n-1} \qquad (2.7)$$

$$k = 0.67 + \frac{f'_c}{9000} \text{ (psi)} \qquad (2.8)$$

The stress-strain relationship obtained by Equations (2.6), (2.7), and (2.8) was compared with experimental data, and the results are presented in Figure 2.42.

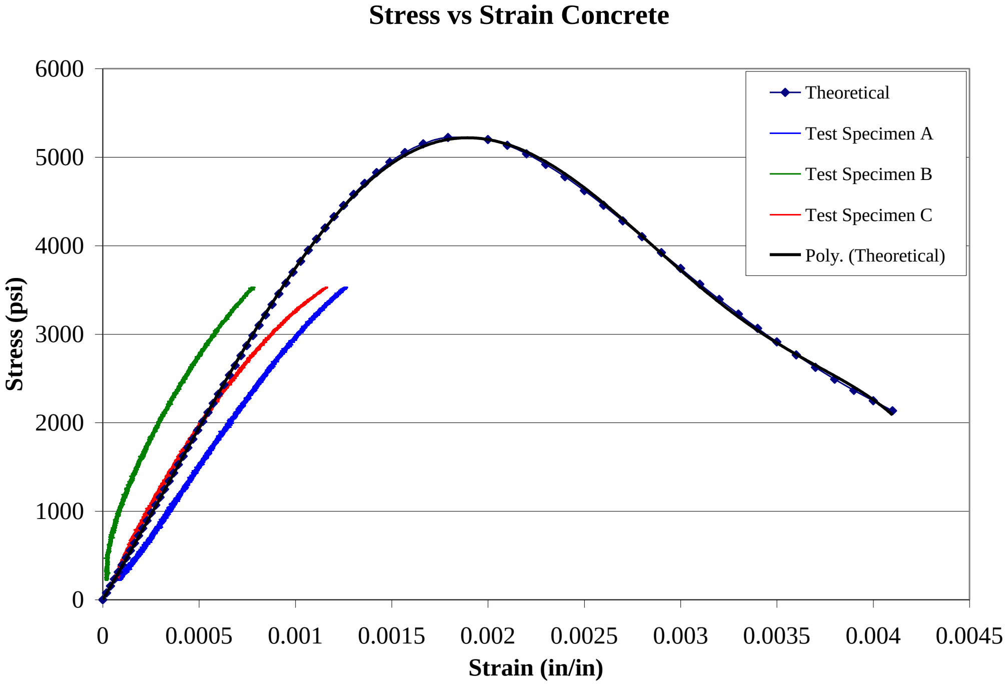

Figure 2.42: Concrete stress-strain behavior, experimental and theoretical.

2.9.2 Steel strength

Tensile properties for the steel pile jacket and the reinforcing bars were tested in accordance with ASTM A370 by Quality Inspection and Testing, Inc. The experimental steel properties are given in Table 2.8.

Table 2.8: Sectional Properties for the Steel Jacket and Reinforcing Bars

Items	Steel Jacket	Reinforcing Bars
Modulus of elasticity (psi)	28,946,889	30,610,801
Yield stress (psi)	57,243	76,531
Ultimate stress (psi)	71,674	105,612
Percent elongation (%)	28.03	26.50

2.9.3 Flexural stiffness of the pile

For calculating the flexural stiffness of the reinforced concrete steel-jacketed pile, we assumed that concrete was fully bonded to the rebar, no slip would occur between the concrete and the steel jacket, concrete stress-strain is nonlinear, and steel behaves linearly until it yields. Based on these assumptions, a program was written to approximate moment-versus-strain (moment-versus-curvature). The program utilized numerical integration to evaluate stiffness change. Moment at a given strain was calculated using 300 parallel slices. For the analysis, the concrete in each slice was considered uncracked until subjected to a strain that could cause cracking. After the cracking strain was reached, the concrete was considered cracked and the tensile capacity of the concrete was zero. Using an iterative approach, the strain on the compressive side of the pile was changed until the summation of forces in both the tensile and compressive zones of the pile were equal to zero. After equilibrium was reached, the moment needed to cause strain at the outer edges of the pile was calculated using summation of moments about the edge of the pile. The methodology was based on the following assumptions:

- Plane sections before bending remain plane after bending;
- Steel jacket and concrete are fully bonded;
- Reinforcing bars and concrete are fully bonded;
- Concrete stress is determined from stress-strain curve;
- Concrete tensile strength is considered zero after being subjected to a strain sufficient to cause cracking; and
- Steel stress is determined from its modulus of elasticity.

The following equation was used to find pile flexural stiffness at a given strain level:

$$EI = \frac{M \bullet c}{\varepsilon} \tag{2.9}$$

where EI = flexural stiffness, M = moment used to calculate flexural stiffness at the particular point, ε = tensile or compressive strain, and c = distance to the neutral axis from the outermost tensile or compressive fiber.

This step was repeated for the range of strain levels that the pile was subjected to during testing. Thus, flexural stiffness and the corresponding moment were found. In the strain-compatibility analysis, a computer program was written and 300 slices were used.

2.9.4 Pullover analysis

2.9.4.1 Experiment results

The load frame was installed 40.25 inches above the ground line (see Figure 2.43). At that height, both the load cell (applied load) and transducer displacement were read. Results for three load cycles are presented in Figures 2.44, 2.45, and 2.46. Average loads and deflections are presented in Figure 2.47.

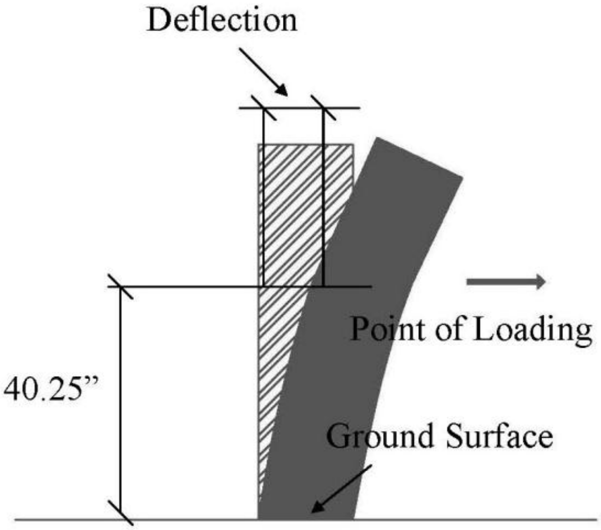

Figure 2.43: Location of deflection measurement.

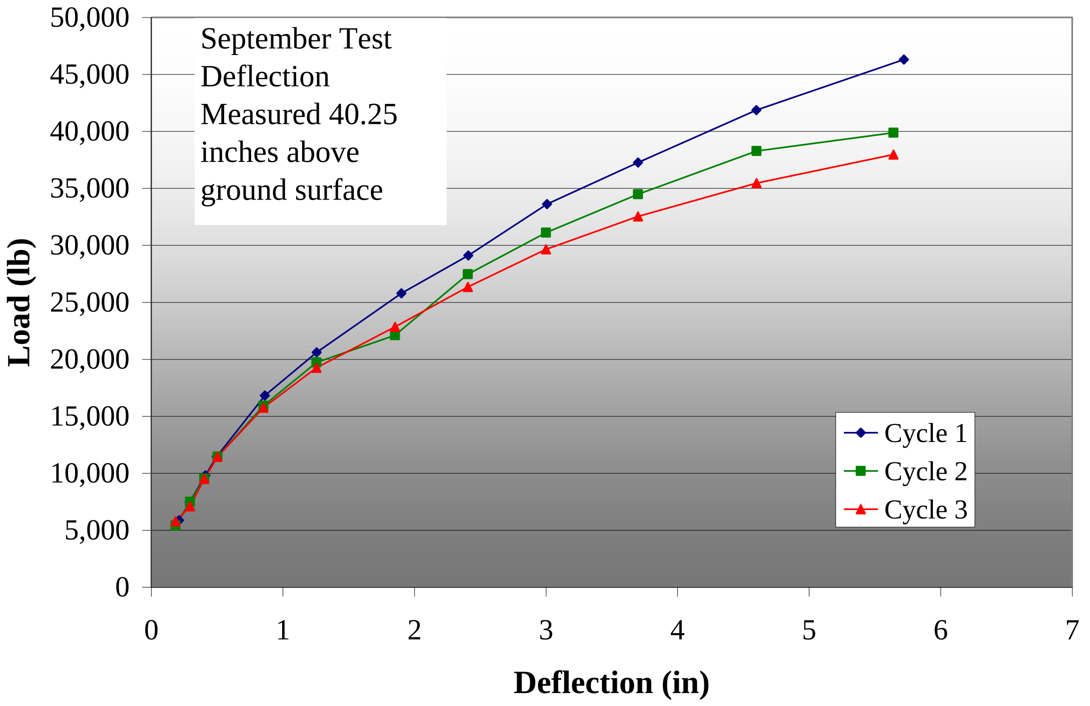

Figure 2.44: September pile test pullover analysis.

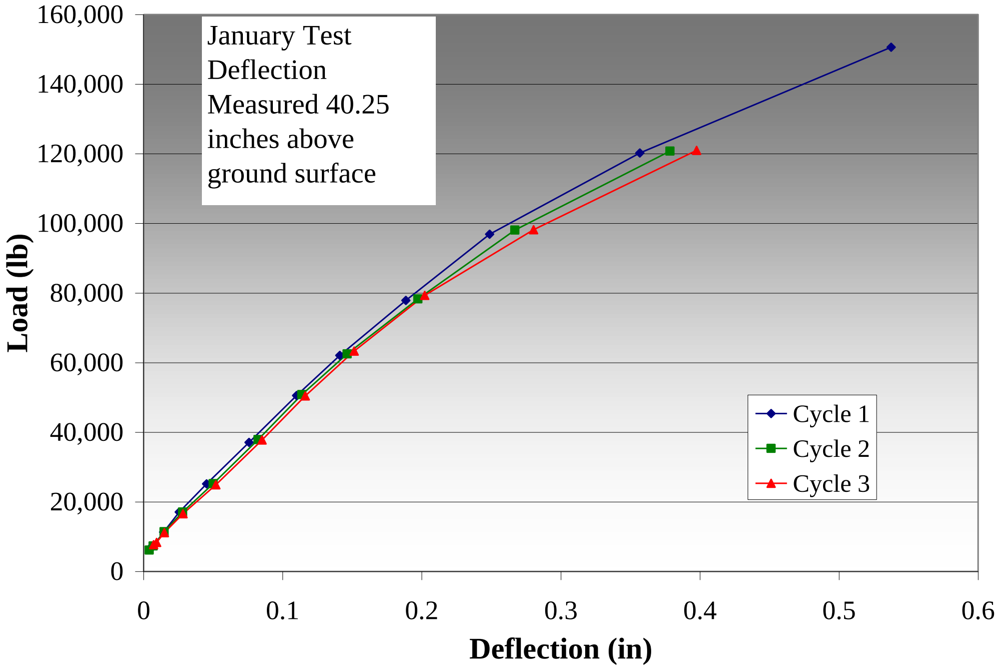

Figure 2.45: January pile test pullover analysis.

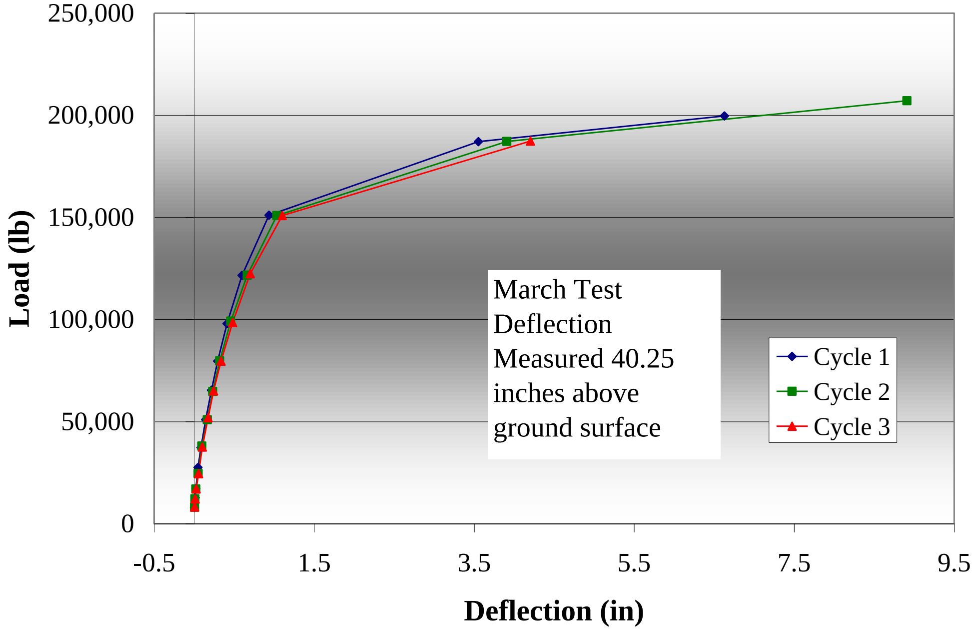

Figure 2.46: March pile test pullover analysis.

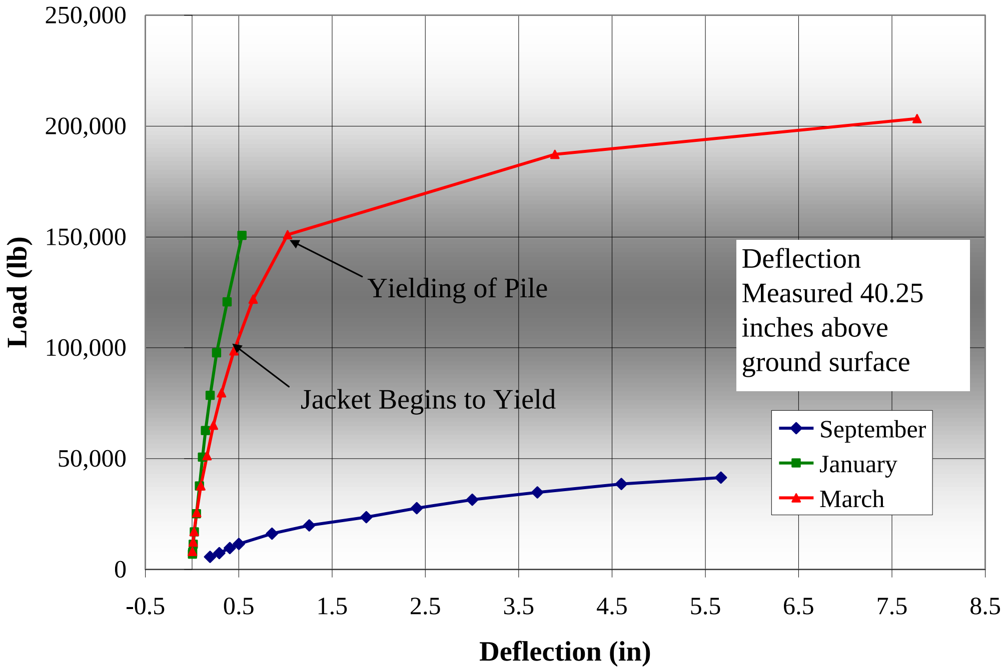

Figure 2.47: September, January, and March pile test pullover analysis.

2.9.5 Depth of fixity analysis

In the past, results from lateral pile tests have been described in terms of depth of fixity (Coduto 2001). There are several ways of finding equivalent depth of fixity. One method uses equations of bending to approximate distance from the point-of-load application to an equivalent fixed depth, similar to a cantilever beam. Another method uses the location of the maximum moment as the location for depth of fixity (Horazdovsky 2010).

2.9.5.1 Depth of fixity flexural analysis

In the depth of fixity analysis, the pile is modeled as a cantilever beam, where the soil above the depth of fixity is ignored and the soil below the depth of fixity is considered infinitely rigid (Coduto 2001). The deflection at the end of a cantilever beam is described as

$$\Delta = \frac{PL_e^{\ 3}}{3EI} \tag{2.10}$$

where Δ = deflection at point of loading, P = load, EI = flexural stiffness, and L_e = distance from load to fixed end.

Depth of fixity is typically measured from the ground surface. The pile stiffness (EI) is based on test results for the material properties (E, concrete stress-strain values, tensile strength), measured load and corresponding calculated moment of inertia, and measured deflection at the location of the load. Thus, by rearranging the variables in Equation (2.10) and by subtracting the distance from the point of load to the ground surface, the depth of fixity can be found:

$$L_f = (L_e - L) = (\frac{3EI\Delta}{P})^{1/3} - L \tag{2.11}$$

where L_f = depth of fixity measured from the ground surface, L_e = distance from point of loading to the depth of fixity, and L = distance from point of loading to ground surface.

Figure 2.48 presents load versus depth of fixity for the September, January, and March pile tests. This analysis is only valid for elastic behavior of the pile. During the last two load increments of the March test, a plastic hinge formed below the ground surface. Since this analysis is not valid beyond the elastic zone of the pile, these load increments are not included in this analysis. See Figure 2.49 for pile behavior during testing and a diagram of the depth-of-fixity analysis.

Results show that depth of fixity during March, when the frost depth was at its greatest, was actually lower then depth of fixity during January when frost depth was not as deep. This finding can be attributed to several factors. Stiffness of silt increases as the temperature decreases, and the silt surrounding the south pile had a 1-foot layer of gravel with low moisture content above it. This layer of gravel is not present where the north pile was tested.

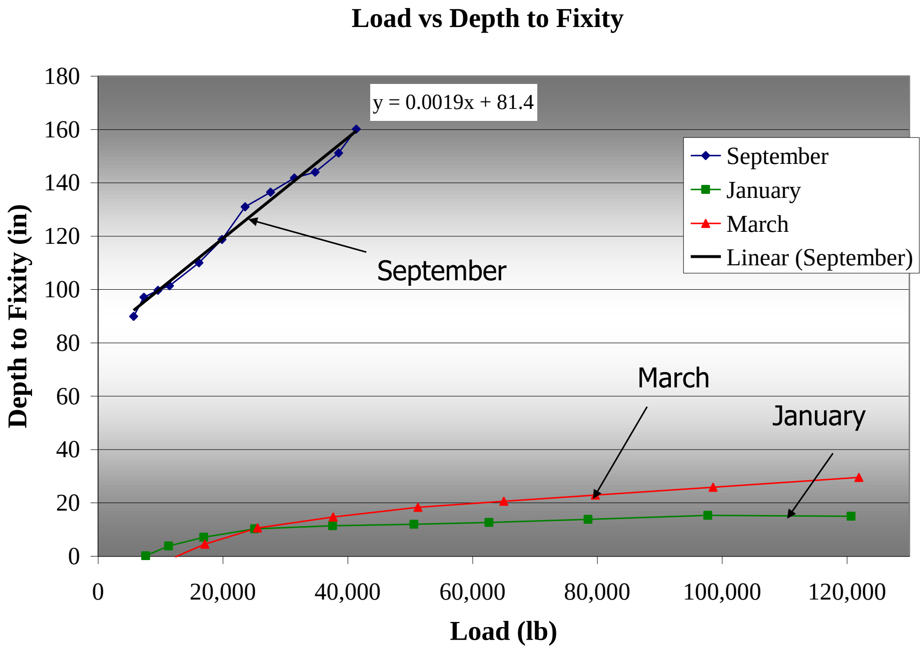

Figure 2.48: Load vs. depth of fixity.

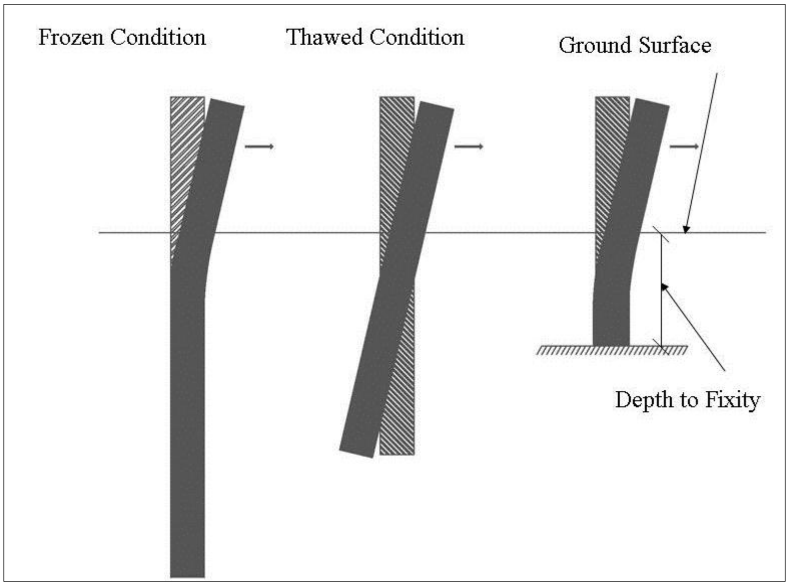

Figure 2.49: Pile short and long foundation behavior and depth of fixity.

2.9.6 Depth of fixity maximum moment analysis

Depth of fixity was also calculated by the method of locating the maximum moment. The location of maximum strain corresponds to the maximum moment, so strain data from testing were used to find the maximum moment. In Figures 2.50, 2.51, and 2.52, strain versus depth is plotted for each test increment. All load steps are plotted on the same graph.

For the September test, the pile response was that of a short foundation, with the pile rotating through the soil as though it were a rigid beam (see Figure 2.49). Strain data for the September test were noisy, and the location of maximum strain for the September test was not as clear as for the January and March tests (see Figures 2.50–2.52). This difference is a result of the pile responding more like a rigid body in soft soil than as a pile bending about a specific point. The depth of fixity for the September test was approximated at between 6 and 9 feet below ground surface.

For January pile testing, the pile response was that of a deep (long pile) foundation, with the pile bending and the toe of the pile not moving. Strain readings from the tension side of the pile indicated that the location of maximum strain was between ground surface and 12 inches below ground surface. The maximum strain occurred 6 inches below ground surface. On the compression side of the pile, no strain gage was located 6 inches below ground surface. Both tension and compression strains at 6 inches above ground surface and 18 inches below ground surface had similar strains. The neutral axis of the pile had shifted toward the compression side of the pile at higher loads. Maximum strain for the January test occurred between ground surface and 12 inches below ground surface.

For the March pile testing, pile response was again that of a deep foundation, with the pile bending and the toe of the pile not moving. Strain readings from the tension side of the pile indicated that the location of maximum strain was between ground surface and 18 inches below ground surface. Again, the maximum strain was 6 inches below ground surface. On the compression side of the pile, no strain gage was located 6 inches below ground surface. Again, like the March tests, both tension and compression strains at 6 inches above ground surface and 18 inches below ground surface had similar strains. The neutral axis of the pile had shifted toward the compression side of the pile at higher loads. Maximum strain for the March test occurred between ground surface and 12 inches below ground surface. It is noted that soil springs of frozen soils have been constructed using two approaches: (1) trial and error and (2) double differentiation of bending moment data. The results of the first approach can be found in Horazdovsky (2010). The details and results of the second approach are presented in Chapter 6.

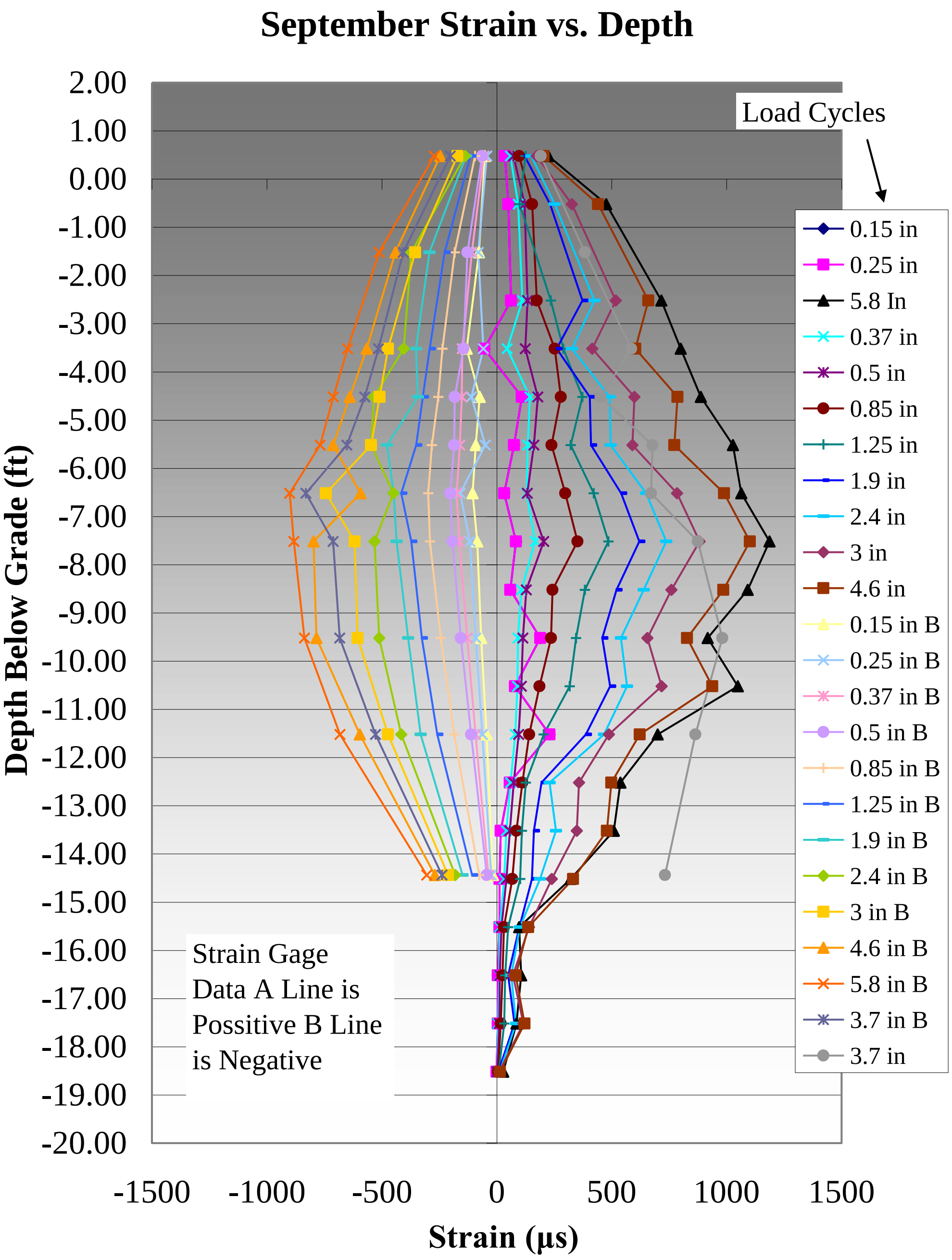

Figure 2.50: September pile test strain vs. depth.

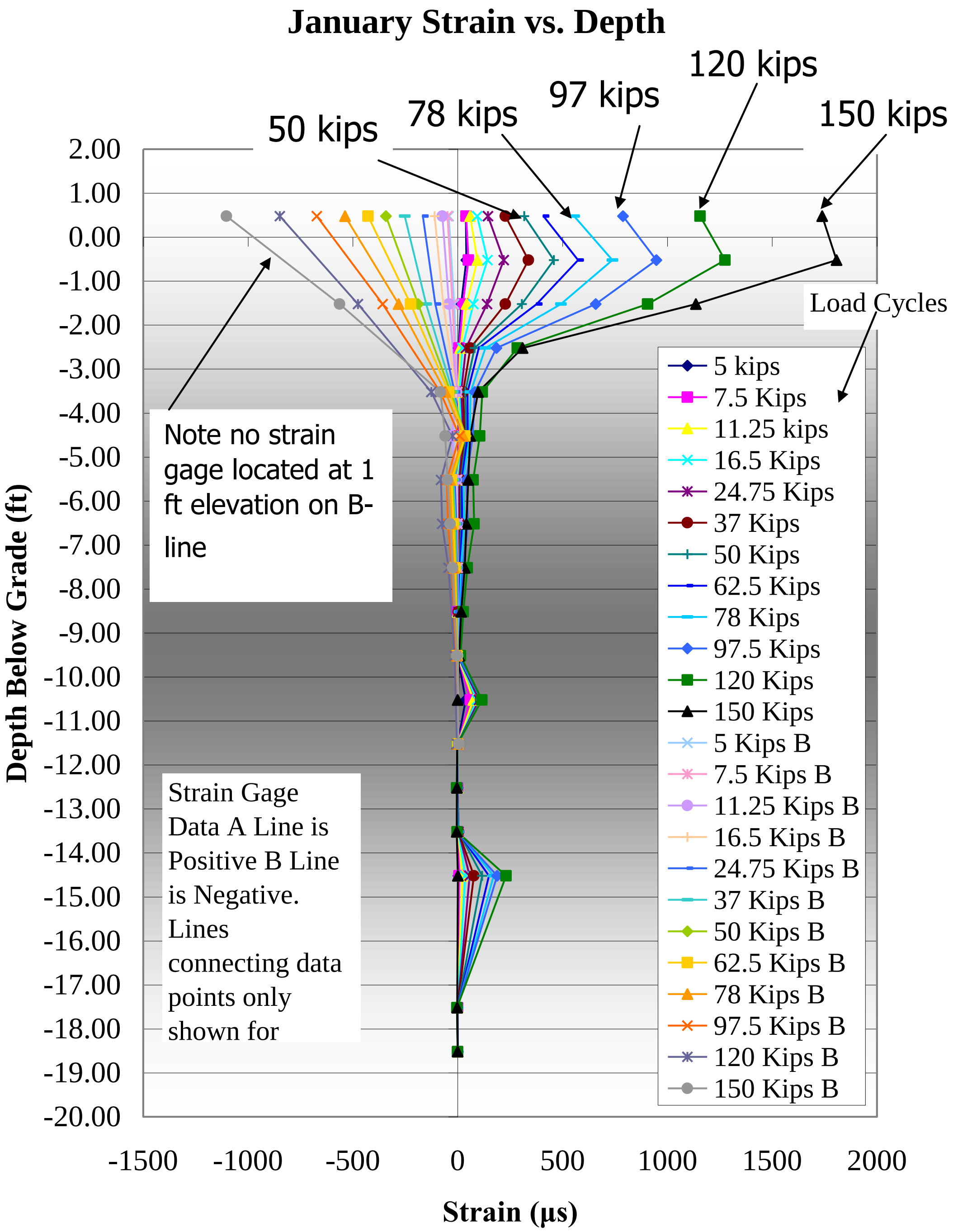

Figure 2.51: January pile test strain vs. depth.

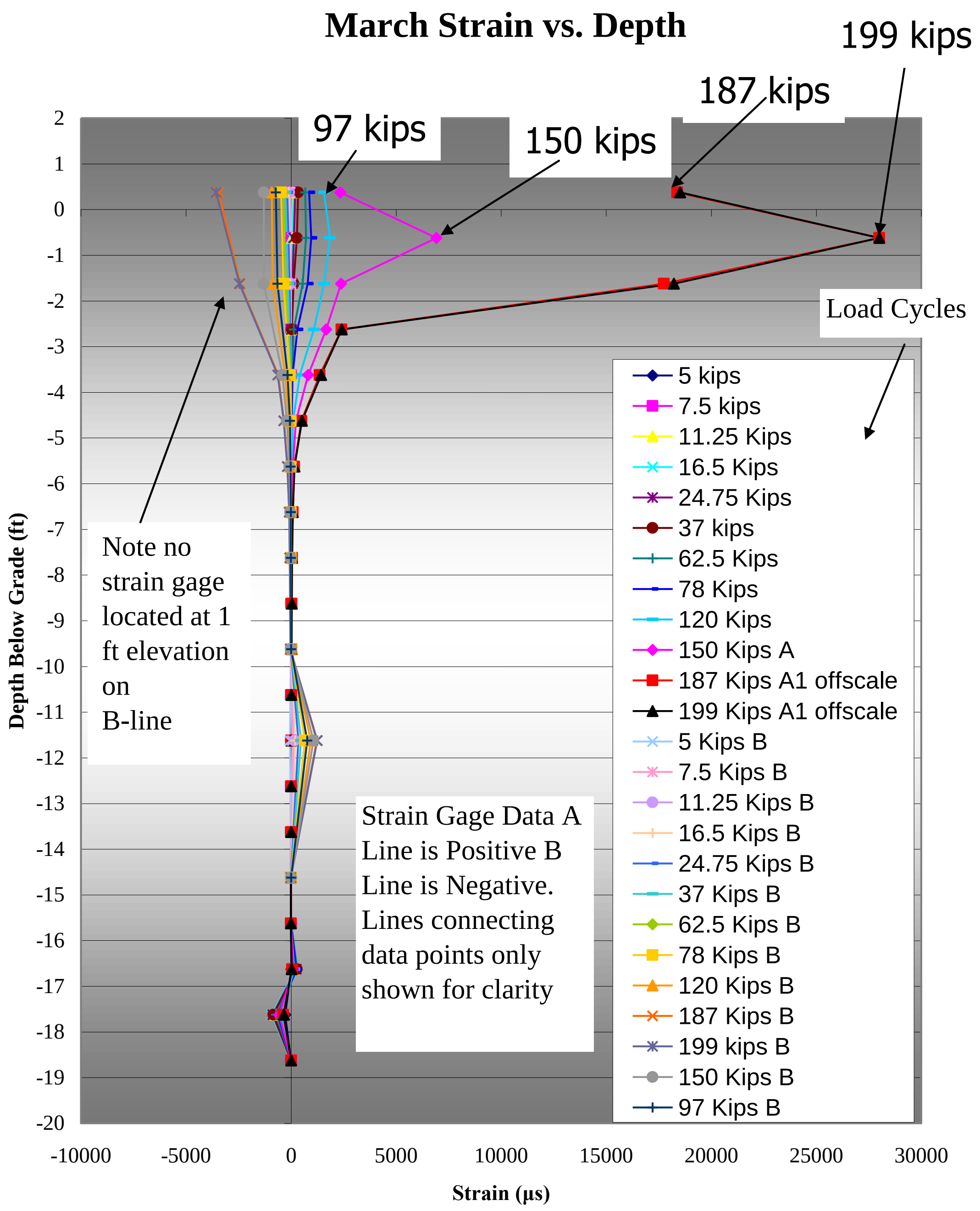

Note no strain gage located at 1 ft elevation on B-line

Strain Gage Data A Line is Positive B Line is Negative. Lines connecting data points only shown for clarity

Figure 2.52: March pile test, strain vs. depth.

2.9.7 Findings for cyclically lateral-loaded piles to failure

The pile tested in thawed conditions experienced short foundation behavior. The pile rotated about a point below subgrade (see Figure 2.53). The toe of the pile kicked, and failure of the system occurred in the soil. During frozen conditions, the pile was extremely stiff and experienced a bending-type failure that is typical of deep-foundation behavior. During both the

January and March tests, the location of the maximum moment was within 0.75 pile diameters of the ground surface for the 16-inch-diameter pile in Fairbanks silt or Fairbanks silt with a foot of gravel on top. During March testing, a plastic hinge in the pile formed 6 to 12 inches below the ground surface. Figure 2.54 is a picture of the yielded south pile.

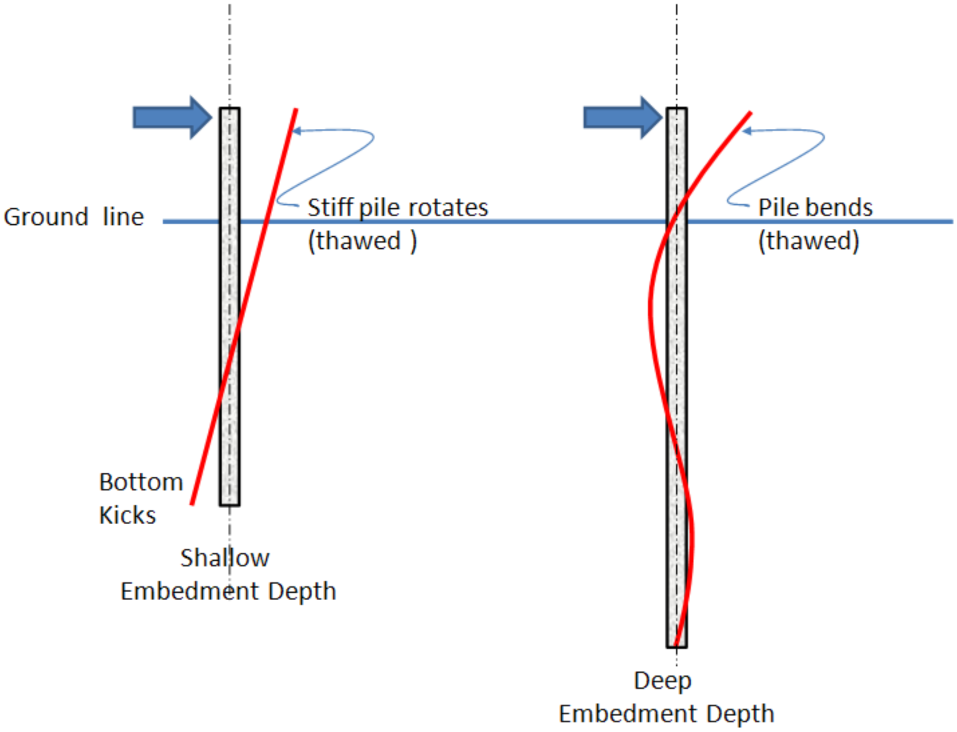

Figure 2.53: Short pile embedment vs. deep pile embedment.

Figure 2.54: Excavation of south pile tested March 2010.

2.9.7.1 Depth of fixity

Table 2.9 summarizes the results. The two methods described produced comparable results. While differences between the two methods appeared in the thawed condition, the differences can be attributed to the pile rotating through the extremely soft soils during summer testing (see Figure 2.53). Results from the flexural analysis were no longer valid after the formation of a plastic hinge, and are not shown for loads larger than 120 kips. The results from this analysis also became less accurate as the pile rotated in the ground. Thus, results for the thawed fall test are not shown for loads over 30 kips. The depth of equivalent fixity shifted up 8 to 10 feet during winter testing in comparison with summer testing. When designing for a worst-case winter depth of fixity for pushover analysis, it is safe to assume that the depth of fixity is located at or within 0.75 diameters of the ground surface for a similar pile in similar soil conditions.

Table 2.9: Depth to Fixity for a 16-Inch-Diameter Steel-Jacketed, Reinforced Concrete Pipe Pile, Embedded in 19.5 Feet of Fairbanks Silt

Depth of Frost	Thawed Soil (September)		4.5-Foot Layer of Seasonally Frozen Soil (January)		7.5-Foot Layer of Seasonally Frozen Soil (March)	
Load (kips)	Depth from Equivalent Stiffness Method (ft)	Depth from Location Maximum Moment (ft)	Depth from Equivalent Stiffness Method (ft)	Depth from Location Maximum Moment (ft)	Depth from Equivalent Stiffness Method (ft)	Depth from Location Maximum Moment (ft)
10	8-9	5-11	0-1	0-1	0-1	0-1
25	10-12	5-11	0-1	0-1	0-1	0-1
30	10-12	5-11	0-1	0-1	0-1	0-1
78			1-2	0-1	1-2	0-1
120			1-2	0-1	1-2	0-1
150				0-1		0-1
190				0-1		0-1
200				0-1		0-1

2.9.7.2 Soil springs

Soil springs were calculated for both frozen and unfrozen conditions. Initially, an attempt was made to use existing soil spring data from the LPile database. However, these spring values provided a poor comparison between the predicted *p-y* curves and the measured *p-y* curve data. Therefore, empirical springs were developed to correlate with experimental results. Spring stiffness increased by two orders of magnitude, from thawed to frozen. The force required to displace the soil spring 0.5 inches was approximately 0.3 kips in summer conditions to over 27.5 kips during frozen conditions. This spring represents the equivalent soil force for a 1-inch section of the pile.

2.9.7.3 Quantified stiffness increase and moment of maximum moment

The calculated yield and ultimate strength for the test pile was 4,400 kip-inches and 8,700 kip-inches, respectively. In September, the north 16-inch-diameter pile was tested, and during the test, it experienced short foundation behavior; that is, the toe of the pile kicked and the pile rotated through the soil. Failure occurred in the soil, not in the pile. During the January and March tests, the north pile (January test) and the south pile (March test) behaved as a long pile. In January, we determined that the capacity of the load frame was inadequate to fail the pile. During the January tests, the pile steel jacket started to yield at a lateral load exceeding 100 kips.

At that point in the test, the effective length was about 45 inches. The effective length value was determined by dividing pile capacity at yield (ft-kips) by the lateral force, causing the pile to yield. The resulting effective length corresponded to an equivalent depth of fixity of 5 inches below ground surface. By the end of the third cycle at 120 kips, plastic deformation was around 0.09 inches at the point of loading. After the first cycle of 150 kips, approximately 0.14 inches of plastic deformation occurred at the loading. This plastic deformation of the pile itself corresponds to calculated yield and ultimate strength of the pile, with a corresponding depth of fixity of 5 inches.

During March testing, the steel jacket started to yield above 100 kips of load, again corresponding to a depth of fixity of 5 inches below ground surface, calculated based on the assumptions stated above. By the end of the third cycle at 120 kips, plastic deformation was around 0.15 inches at the point of loading. After the first cycle of 150 kips, approximately 0.3 inches of plastic deformation occurred at the loading. This stiffness difference could be due to the difference in soil conditions. In the top 1 foot of the soil, the south pile had a layer of gravel fill. In the north pile, 1 to 2 inches of cobbles were mixed with the silt in the top 8 inches of soil; the material was over 80% silt. The difference also could be attributed to a difference in soil temperature. During the January test, the lowest recorded soil temperature was -18°C. During March testing, the lowest soil temperature was -8°C.

The March test was stopped when the rotation in the plastic hinge that formed just below the ground surface became too great and the U-bolts that attached the test frame to the test pile slipped up the pile. Total displacement at the point of loading was 8.9 inches under a load of 207 kips. The ultimate moment placed on the pile during testing, based on the location of the plastic hinge, was 6 to 12 inches below the ground surface. The magnitude was 9,570 to 10,800 kip-inches, which was 10% to 25% more than the estimated ultimate pile capacity.

In comparison to summer testing, shear demand in the pile increased from 42 kips to 207 kips: a 409% increase. Because of the excessive ground displacement, yielding of the test pile was not obtained during summer testing. The test pile had a maximum lateral displacement of 5.7 inches at the point of loading. While the pile started to plastically deform during January testing, the test was not taken beyond the ultimate capacity of the pile. During March testing, the displacement capacity at yield measured 0.75 inches at the point of loading. The force required to yield the pile was approximately150 kips. The stiffness increase from summer to winter was significant. Since the pipe rotated in the summer condition, the displacement capacity was not compared.

2.9.7.4 Conclusions for quasi-static cyclic lateral pile tests in Fairbanks, Alaska

The ADOT&PF funded this study to find the upper limit of stiffness for a typical bridge pile foundation in seasonally frozen soil. This research quantifies a stiffness increase for a 16-inch, steel-jacketed reinforced concrete pile embedded in frozen and unfrozen silt.

As soils freeze, stiffness and strength increase. Thus, if a pile is embedded in soil and the soil freezes, stiffness of the foundation system is expected to increase. As a result, the depth-to-equivalent fixity is reduced, and the displacement distance at the top of the pile before pile failure (displacement capacity) is reduced.

Sixteen-inch-diameter steel-jacketed, reinforced concrete piles embedded in frozen soil were subjected to cyclic quasi-static lateral load tests. The results of these tests showed that the piles behaved similarly to the same piles modeled as a fix cantilever beam, with the location of the fixed end being just below ground surface. Shear demand for piles in frozen soil versus piles in thawed soil increased over 400%. Depth of fixity of the pile was within 0.75 pile diameters of the ground surface during the winter and 8 pile diameters of the ground surface during the summer. Results were similar for two conditions: a 16-inch-diameter pile in Fairbanks silt and Fairbanks silt with a 1-foot layer of gravel fill atop the ground surface. The stiffness increase from summer to winter was notable. In summer, the unfrozen soil was easily compressed out of the way. In winter, as water in the soil froze, the soil became extremely stiff.

For earthquake design as an upper design limit, the depth of equivalent fixity is often used as a design parameter. In this case, the pile may be considered fixed at the ground surface for frozen silt in Interior Alaska. For a 16-inch-diameter steel-jacketed, reinforced concrete pile in similar soil conditions, it is accurate to assume that the pile is fixed at or within 0.75 pile diameters of the ground surface. For the thawed condition, the pile experienced short foundation behavior, with the pile simply rotating through the soil.

Soil springs used to model the pile in frozen soils are significantly stiffer than those that represent thawed or unfrozen soils. The spring stiffness needed to model the pile increased by two orders of magnitude, from thawed to frozen. For a soil spring representing the top few inches of soil and a 1-inch-long pile section, the force required to displace the soil spring 0.5 inches increased from 0.3 kips in summer to over 27.5 kips in winter.

CHAPTER 3. FULL BRIDGE EXPERIMENTS

3.1 Introduction

In order to investigate the influence of seasonal freezing on the seismic performance of bridges, a newly constructed bridge—North Fork Campbell Creek Bridge in Anchorage, Alaska—was instrumented with a network of accelerometers to monitor its dynamic and seismic behavior. Earthquake-induced vibration data were collected and analyzed to identify the fundamental frequency. Concurrently, a borehole was drilled under the bridge and a thermal probe was used to monitor the temperature profile of the bridge site. The relationship between the fundamental frequency and the depth of frozen ground was established. Binonwangan (2009) reported the field-monitoring results from December 2008 to March 2009. In this chapter, monitoring facilities and data processing are reviewed, and the new data and analysis results collected after March 2009 are discussed.

3.2 Description of Regional Climate

Anchorage is located in a seismically active region, with several major faults, such as Lake Clark–Castle Mountain Fault and Denali Fault, and a megathrust zone around it. Historic seismic activity (from 1899 to 2004) in the southcentral region of Alaska is shown in Figure 3.1. The earthquake risk in this region is among the highest in Alaska.

The local climate of Anchorage is classified as subarctic (the Köppen climate classification is Dfc), with an average summer temperature of 37°F to 65°F and an average winter temperature of 5°F to 35°F (DOWL Engineers 2005). Frost penetration averages 4 to 6 feet (Miranda 2007).

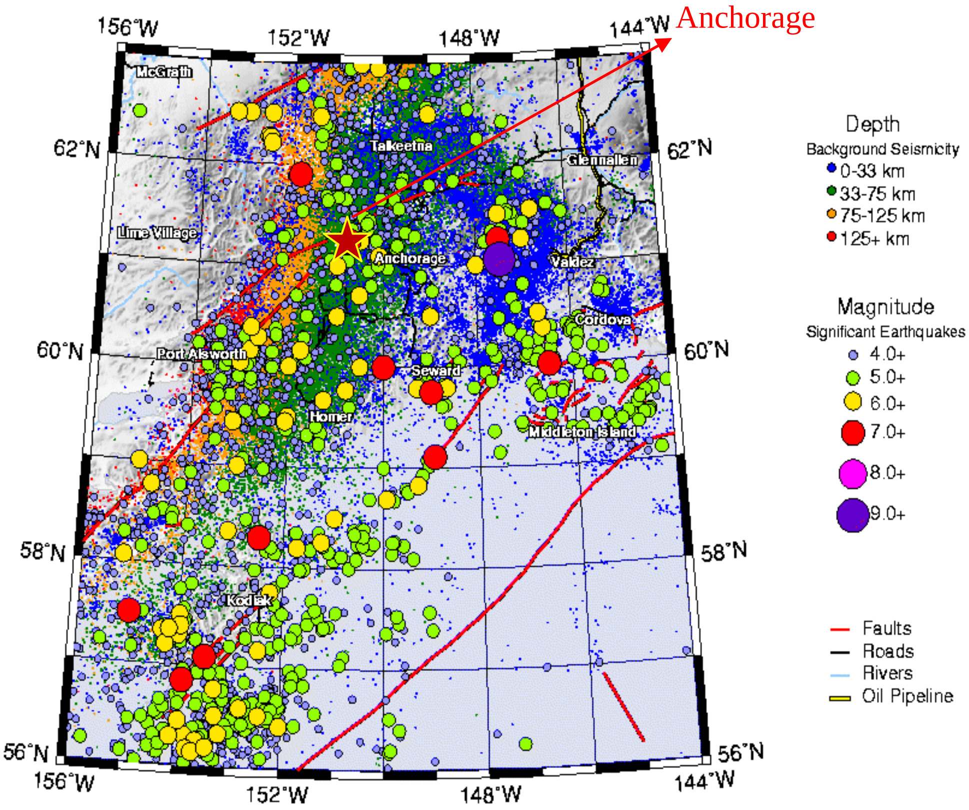

Figure 3.1: Southcentral Alaska seismicity (AEIC 2010).

3.3 Description of the Bridge and Monitoring Facilities

Figure 3.2 shows the location of the selected bridge in Anchorage, Alaska. As illustrated in Figure 3.3 and Figure 3.4, a prestressed, reinforced concrete girder bridge in Anchorage, referred to as North Fork Campbell Creek Bridge, was selected for field monitoring. The reasons we chose the North Fork Campbell Creek Bridge were that (1) it is supported on an extended steel-pipe pile-shaft system filled with reinforced concrete, a typical bridge foundation used in Alaska; (2) the bridge site consists of original sandy gravelly soils overlaid with a few feet of organic soils; and (3) the water table is within 1 foot of the ground surface. Such a site provides an ideal opportunity to evaluate the upper bounds of seasonal frost effects.

Figure 3.2: Project site (Google Earth 2010).

Figure 3.3: North Fork Campbell Creek Bridge.

(a) (b)

Figure 3.4: Views of the bridge substructure: (a) summer, (b) winter.

3.3.1 Description of North Fork Campbell Creek Bridge

Under the management of the ADOT&PF, the North Fork Campbell Creek Bridge was constructed in fall 2007 and opened to traffic in December 2007. Figure 3.5 shows the plan and elevation views of this bridge. The length of the three-span bridge is 358 feet. This concrete girder bridge is supported by two center piers founded on ten 36-inch-diameter concrete-filled steel-pipe piles and abutments founded on eleven 24-inch-diameter concrete-filled steel-pipe piles at both ends.

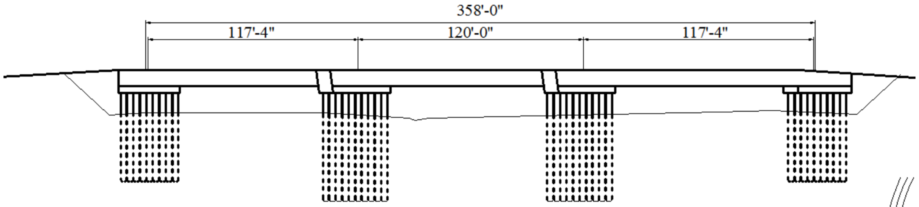

(a) Elevation

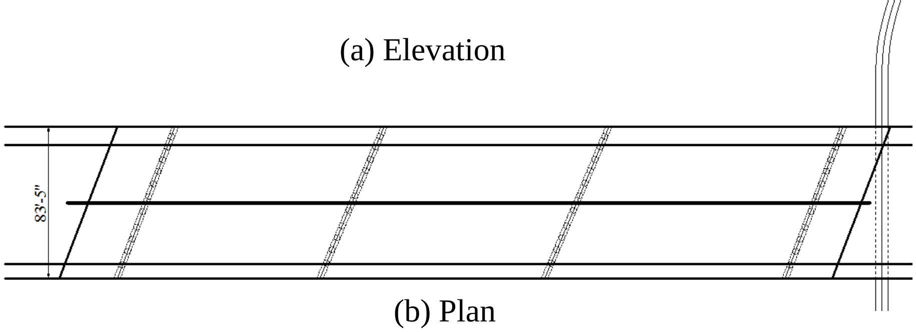

(b) Plan

Figure 3.5: Elevation and plan view of the monitored bridge.

3.3.2 Description of the monitoring system

To collect dynamic response data, a network that consisted of 11 strong-motion sensors was installed on the bridge superstructure in November 2008, according to the plan shown in Figure 3.6. Additionally, a 5-foot-deep borehole was prepared at the site in August 2008 for monitoring ground temperature and frost penetration.

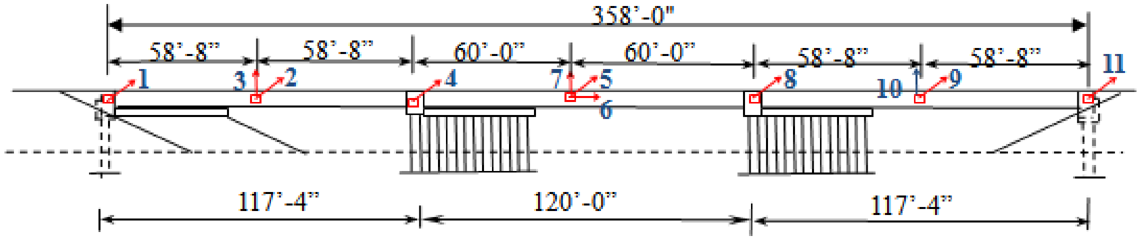

(a) ELEVATION

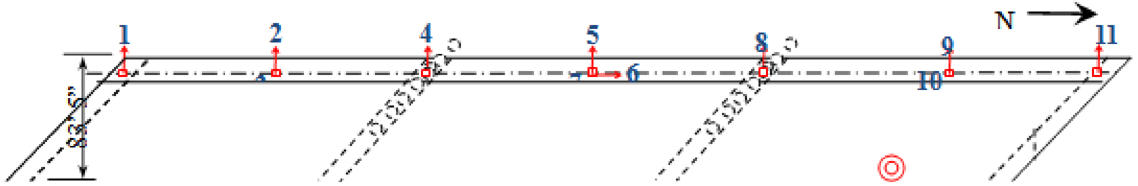

(b) PLAN

Figure 3.6: Schematic of the bridge selected for study and seismic instrumentation plan.

3.4 Frost Penetration Monitoring

3.4.1 Description of the frost penetration monitoring system

A frost-penetration monitoring system (FPMS) was set up at the site (Binonwangan 2009), and the monitoring results were used to determine the vertical temperature profile of the soil in this study. Figure 3.7 illustrates a typical data collection setup in the field. The three main components for setting up the FPMS are summarized below:

(a) A 5-foot-deep borehole was drilled beneath the bridge.

(b) A 1-inch-diameter 10-foot-long PVC pipe was pushed down into the borehole.

(c) Temperature data were collected by using a temperature acquisition cable (TAC) with 11 temperature sensors at predefined spacing (10 inches) and a handheld computer, as illustrated in Figure 3.8.

Figure 3.7: A typical measurement setup (Binonwangan 2009).

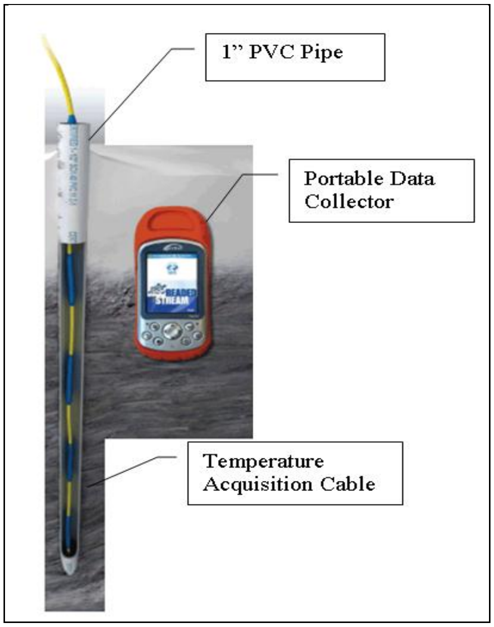

Figure 3.8: Schematic of a temperature acquisition cable (BeadedStream 2008).

3.4.2 Results from frost penetration monitoring

Figure 3.9 shows a set of temperature data collected on March 4, 2008, and illustrates the method used to determine the frost penetration depth. The diamonds in the figure represent the temperature collected by the TAC. As shown in Figure 3.9, the ground temperature is higher than the air temperature and increases with depth. Under the ground level, the rate of temperature change decreases with depth, indicating that the cooling effect of cold air to the ground gradually diminishes. The temperature of the top 3.96 feet of soil is below the freezing point (32°F), and frost depth is 3.96 feet. Table 3.1 summarizes the observed frost penetration data from October 2008 to May 2009 (Binonwangan 2009). The results show that ground freezing continued from the end of October 2008 to the end of March 2009, and thawing occurred thereafter. The deepest frost penetration reached 4.8 feet.

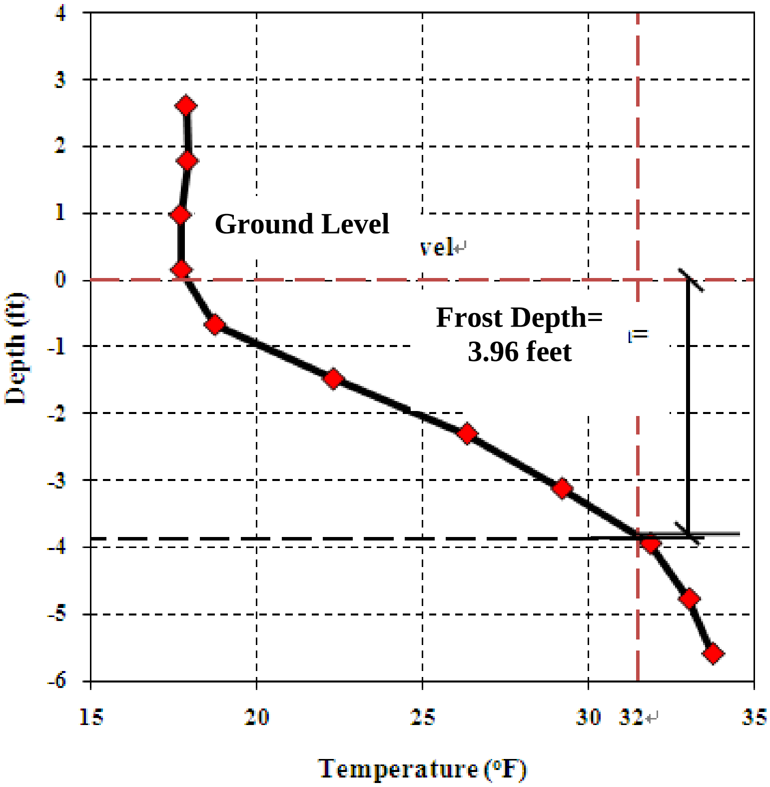

Figure 3.9: Temperature profile on March 4, 2008.

Table 3.1: Frost Depth vs. Time

Date	Frost Depth (feet)	Date	Frost Depth (feet)
10-31-2008	0.25	11-18-2008	2.00
12-09-2008	1.80	01-06-2009	4.80
01-09-2009	4.80	01-16-2009	3.40
01-24-2009	3.80	01-27-2009	3.80
02-05-2009	3.95	03-04-2009	3.96
03-06-2009	4.00	03-22-2009	4.20
03-31-2009	4.00	04-26-2009	3.00

3.4.3 The Modified Berggren Formula for evaluating frost depth

The modified Berggren equation (Andersland and Ladanyi 2004) was utilized to provide a continuous assessment of the frost penetration depth. This formula is the Stefan Formula, corrected for the effects of temperature changes in the soil mass (University of Washington 2008). The modified Berggren formula is

$$X = \lambda \sqrt{\frac{2k_{ave} nFI}{L}} \tag{3.1}$$

where X is the frost depth (feet); λ is a dimensionless coefficient that takes into consideration the effect of temperature changes in the soil mass and accounts for sensible heat changes; k_{ave} is the thermal conductivity of soil, which is the average of frozen and unfrozen soils in units of *BTU/(hr•feet•°F)*; n_f (n_t) is a dimensionless conversion factor for the air-freezing (or thawing) index to surface-freezing (or thawing) index; *FI* is the air-freezing index in *°F•days*; and *L* is the latent heat of soil in *BTU/ft*^{3}. These parameters were calibrated by the field measured frost depth data and their values are listed in Table 3.2.

Table 3.2: The Parameter Values Used for Frost Depth Evaluation

Parameter	Value
λ	0.89
kave (BTU/(hr• feet• °F))	0.965
nt	1.3
nf	0.6
L (BTU/ft^3)	3110

The temperature data used to compute *FI* were obtained from a local weather station called MNUAA2 (location shown in Figure 3.2). In this computation, it was assumed that the freezing of ground started on the first day after the average temperature was below 32°F for five consecutive days. For comparison, the estimated frost depth from October 2008 to May 2009 is shown in Figure 3.10, which demonstrates that the calibrated modified Berggren formula can accurately predict the frost depth for this site. This calibrated formula was used to evaluate the frost depth for the 2009–2010 winter. The result is presented in Figure 3.11.

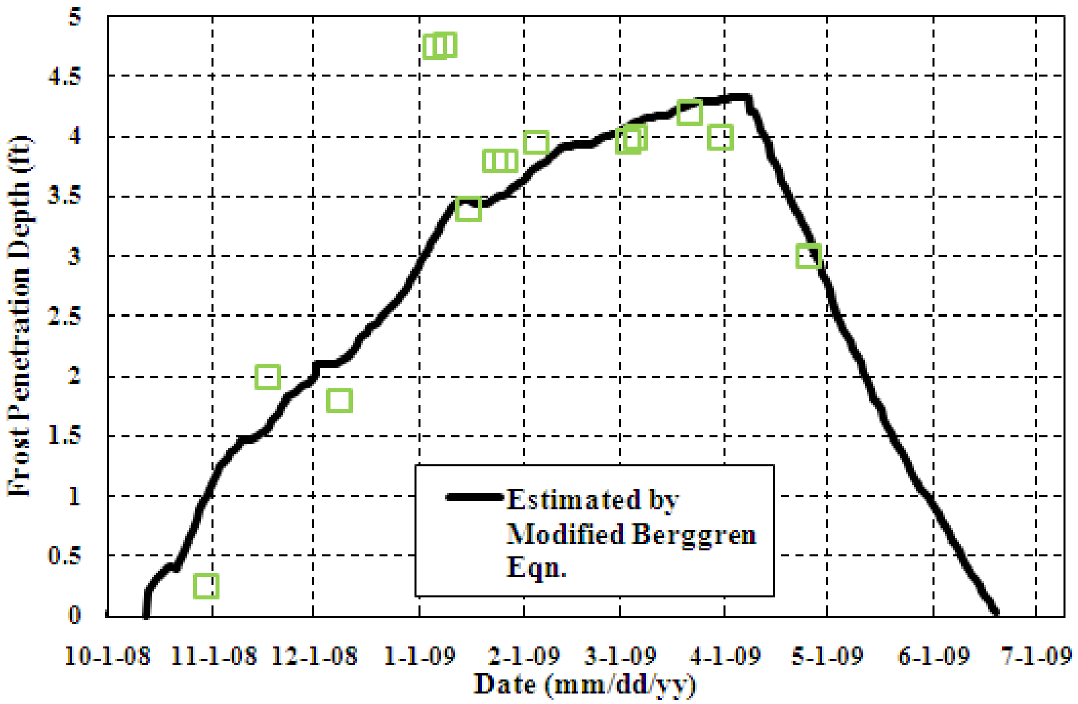

Figure 3.10: Comparison of frost depths estimated by using modified Berggren equation with field-monitoring data.

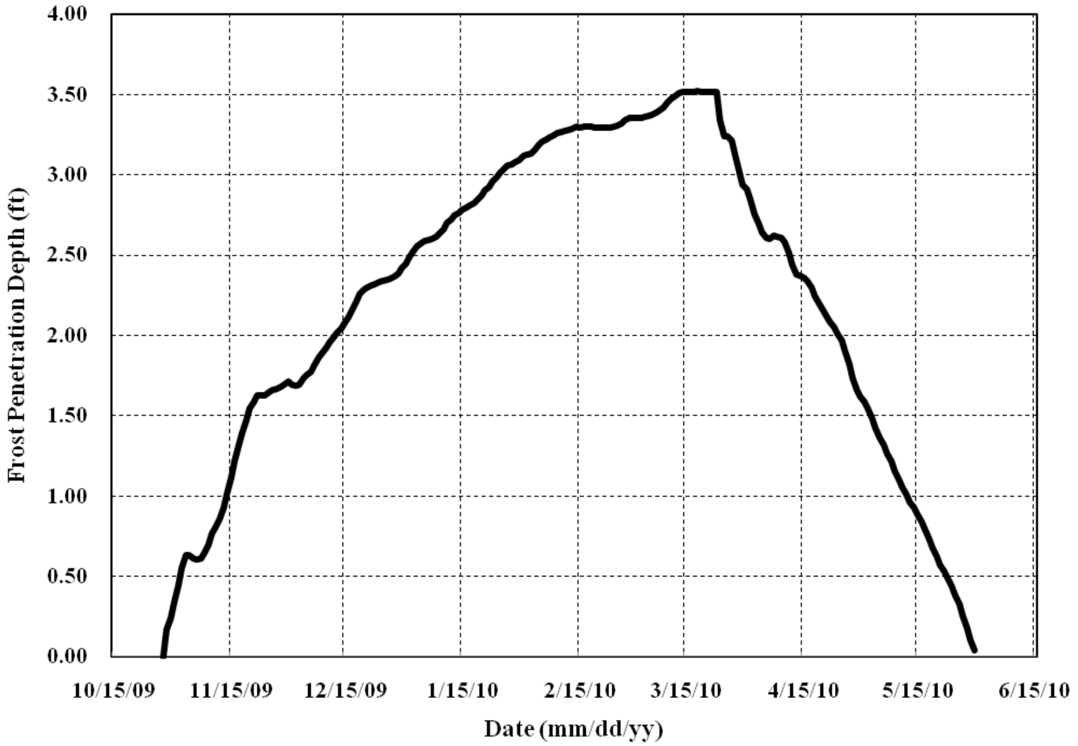

Figure 3.11: Frost depth evaluated by using the modified Berggren equation from October 2009 to March 2010.

3.5 Bridge Seismic Response Monitoring

3.5.1 Description of the bridge seismic response monitoring system

The seismic response monitoring system used in this project includes 11 (ES-U2 EpiSensor) force balance uniaxial accelerometers and a 12-Channel Granite Data Recorder (Figure 3.12). As shown in Figure 3.6, the 11 sensors were installed to monitor north–south (longitudinal), east–west (transverse), and vertical vibrations of the bridge during earthquakes.

(a) (b)

Figure 3.12: Strong motion sensor and data acquisition system: (a) ES-U2 EpiSensor, (b) a 12-Channel Granite Data Recorder (Kinemetrics 2010).

The earthquake data recorded by the recorder were processed by Strong Motion Analyst (SMA), Matlab, and ARTeMIS Extractor programs. Strong Motion Analyst was used to process strong-motion accelerogram records; it can be used to read and process data from EVT files, and save the data as USGS format V2 files (Kinemetrics 2010). A Matlab program was used to convert seismic data from USGS format V2 files to individual acceleration, velocity, displacement, and response spectrum files (ASC file). These acceleration data from ASC files were used to generate an acceleration input file for the ARTeMIS program that analyzed the bridge dynamic properties including modal frequencies and mode shapes. The steps for data processing are summarized in Figure 3.13.

Twenty-two local earthquakes triggered the accelerometer network from January 2009 to March 2010. In most events, only the first transverse mode was excited. Table 3.3 summarizes the first transverse frequency identified from each earthquake event. Other relevant data including earthquake and environment parameters are included in Table 3.3.

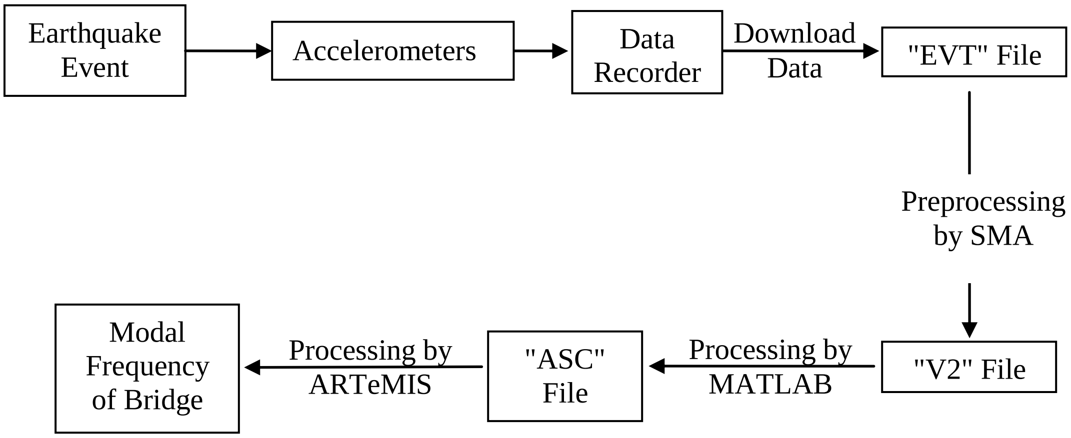

Figure 3.13: Data processing flowchart.

Table 3.3: Earthquake Events, Frost Depth, and First Transverse Modal Frequency

Earthquake Event Date	Earthquake Magnitude (ML)	Epicentral Distance (mile)	Earthquake Depth (mile)	Air Temperature (°F)	Frost Depth (feet)	First Transverse Frequency (Hz)
2009-1-24	5.7	200	63	18	3.80	7.065
2009-2-1	3.3	29	31	2	3.85	7.458
2009-2-09	4.4	310	22	7	3.91	7.774
2009-2-15	4.3	30	25	30	3.91	7.55
2009-2-16	3.7	50	43	30	3.92	7.505
2009-3-12	4.0	140	119	29	4.08	7.593
2009-4-7	4.6	11	15	32	4.00	7.579
2009-4-26	3.7	17	2	44	3.00	6.45
2009-10-4	4.0	73	61	43	0	2.847
2009-11-11	3.9	140	98	21	0.63	3.11
2009-12-15	3.9	120	74	28	2.07	5.02
2009-12-16	3.0	16	32	28	2.12	5.12
2010-1-5	3.2	105	45	21	2.59	5.3
2010-1-21	3.7	31	27	6	2.90	5.747
2010-1-30	3.5	68	59	16	3.09	6.5
2010-1-31	3.0	25	44	12	3.12	7.02
2010-2-2	3.5	75	49	24	3.13	6.994
2010-2-11	4.2	115	66	26	3.27	7.029
2010-2-20	3.6	169	61	34	3.29	7.235
2010-2-21	3.0	35	36	32	3.29	6.83
2010-2-27	3.7	56	37	14	3.34	6.956
2010-3-2	3.7	80	29	33	3.35	6.69
2010-4-23	3.7	45	10	38	2.05	4.31
2010-9-20	4.9	20	26	48	0	2.89
2010-9-25	5.4	143	53	43	0	2.79

3.6 Conclusion and Discussion

The frozen ground thickness and first transverse modal frequency are illustrated in Figure 3.14. A clear correlation is seen between the frost penetration and the bridge first transverse modal frequency. Modal frequency increases with frost penetration. Specifically, when there is no frozen ground, the first transverse modal frequency is detected as 2.5 Hz. As frost thickness increases at about 4 feet, the modal frequency oscillates around 7.5 Hz, representing a 200% increase.

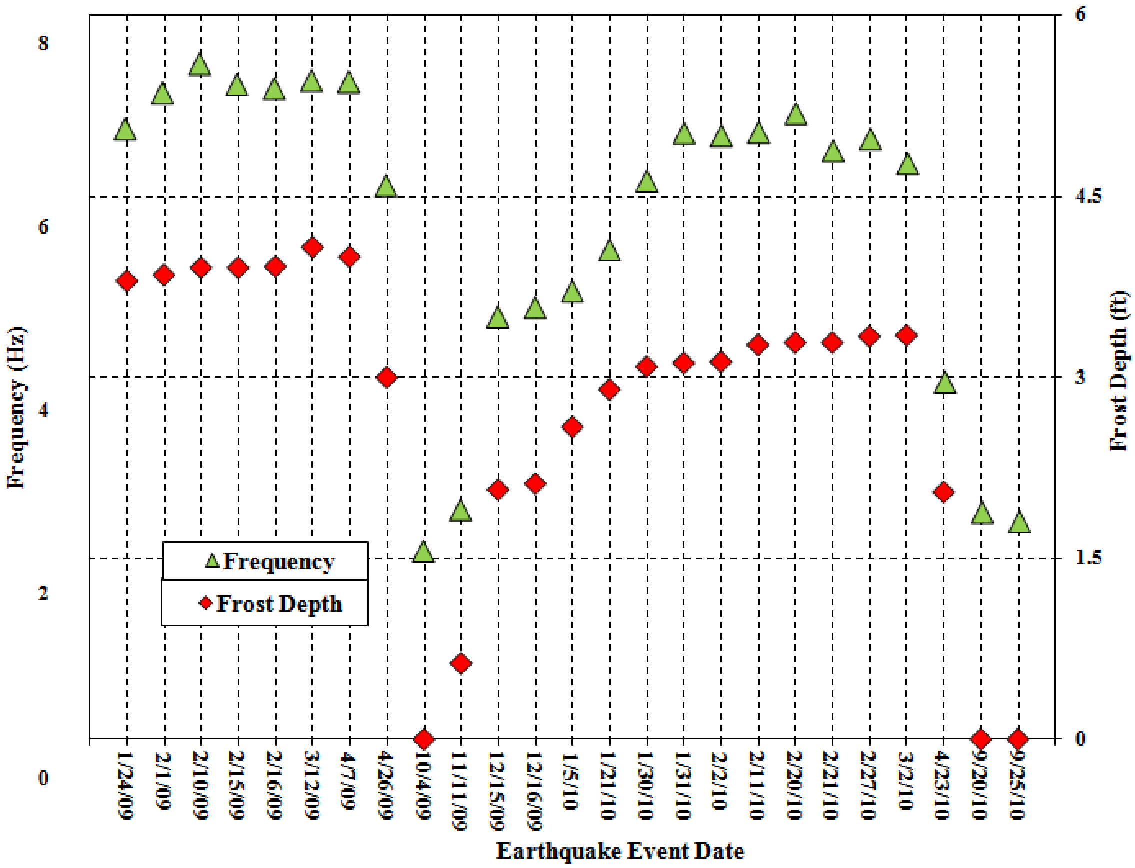

Figure 3.14: Frozen ground thickness vs. first transverse modal frequency.

CHAPTER 4. SEASONALLY FROZEN SOIL EFFECTS ON BRIDGE DYNAMIC PROPERTIES

4.1 Introduction

A 64% drop in the bridge's first transverse modal frequency was observed from winter to summer. In this chapter, numerical simulation is employed to investigate the effects of seasonally frozen ground on the dynamic characteristics of the bridge.

While the finite element (FE) model is an efficient analytical tool, creating a model capable of reproducing the measured dynamic characteristics of a prototype is a challenge. Discrepancies between experimental and analytical dynamic characteristics arise due to assumptions made in modeling, as well as uncertainties in material and geometrical properties and boundary conditions (Brownjohn et al. 2003). We created FE models, calibrated them against the field-monitoring data, and then used them to analyze the seasonally frozen soil effects.

This FE analysis aims at systematically investigating the effects of seasonal frost depth on the dynamic properties of the bridge in terms of natural frequencies and mode shapes. Four cases were studied: (1) no frozen soil; (2) frozen depth reaches 1.5 feet below the ground surface; (3) frozen depth reaches 4 feet below the ground surface; and (4) frozen depth reaches 6 feet below the ground surface.

4.2 Modeling Approach

4.2.1 Model simplification

A model for the entire bridge–foundation–soil system would be ideal for investigating frozen-soil effects. However, such model analysis demands a great amount of computing power and time, which are not readily available at UAA. The Arctic Supercomputer Center at UAF provides sufficient computing power for such analysis; however, it takes a considerable amount of effort to adapt the analysis software to the supercomputers. Therefore, we decided to model the soil–pile system and the bridge superstructure separately. The FE model of the soil–pile system was used to find the equivalent depth of fixity of the piles. The depth-of-fixity results were used for building a simplified model for the bridge superstructure (Priestley et al. 1996). This approach effectively reduces the complexity of the model and the computation demand while not compromising the accuracy of results. The equivalent depth-of-fixity concept is reviewed in the next section.

4.2.2 Introduction of the equivalent cantilever concept

The equivalent cantilever method assumes that the soil–pile system can be replaced by an equivalent cantilever that is fully restrained against lateral translation and rotation at the base (Caltrans 1986; Dowrick 1987; Chai 2002). In this method, the equivalent depth of fixity is used to account for the flexibility of the embedded pile (Chai 2002).

In Figure 4.1, the sketch on the left is a soil–pile system, and the sketch on the right is the corresponding equivalent cantilever. L_a is the height of the pile aboveground, and L_f is the equivalent depth of fixity. The equivalent depth of fixity depends on the relative stiffness between the pile and the surrounding soil and may be determined by equating the lateral stiffness of the soil–pile system to that of an equivalent cantilever (Chai 2002).

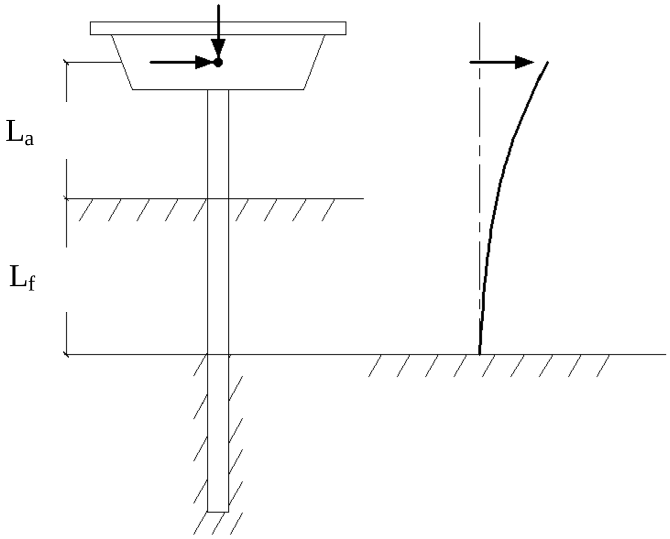

Figure 4.1: Representation of a soil–pile system by an equivalent fixed-base cantilever (Chai 2002).

4.3 Numeric Analysis Platform

The Open System for Earthquake Engineering Simulation (OpenSees) is a FE software framework (Mazzoni et al. 2006) for modeling and simulating the performance of structural and geotechnical systems subjected to earthquakes and other loading conditions. OpenSees is emerging as an excellent research tool for studying structure–soil interaction.

A user-friendly GUI, developed for soil–pile interaction analysis with OpenSees by Lu et al. (2006) and named OpenSeesPL, was used in this analysis. OpenSeesPL (http://cyclic.ucsd.edu/openseespl) is a three-dimensional (3D) simulation environment for seismic and pushover analyses of lateral soil–pile interaction. OpenSeesPL includes a pre-processor for (1) definition of the pile geometry (circular or square pile) and material properties (linear or nonlinear); (2) definition of the 3D spatial soil domain; (3) definition of the boundary conditions and input excitation or pushover analysis parameters; and (4) selection of soil materials from a set of cohesionless and cohesive soil materials (Lu et al. 2006; Elgamal et al. 2008).

4.4 The Constitutive Model and Elements Used in the FE Model

The constitutive models and elements used in this study are reviewed and discussed next.

4.4.1 Constitutive modeling

4.4.1.1 Soil material modeling

In OpenSeesPL, two models—Pressure-Depend-MultiYield Material and Pressure-Independ-MultiYield Material—are available for modeling cohesive and cohesionless soils, respectively (Lu et al. 2006). For cohesionless soil, the constitutive model (Parra 1996; Yang and Elgamal 2002; Elgamal et al. 2003) is developed based on the multi-yield-surface plasticity theory (Prevost 1985). The model, as illustrated in Figure 4.2 and Figure 4.3, is developed with emphasis on controlling the magnitude of cycle-by-cycle permanent shear strain accumulation in clean medium dense sands (Yang and Elgamal 2002; Elgamal et al. 2003; Lu et al. 2006). Special attention is given to the deviatoric-volumetric strain coupling (dilatancy) under cyclic loading, which causes increased shear stiffness and strength at large cyclic shear strain excursions (i.e., cyclic mobility).

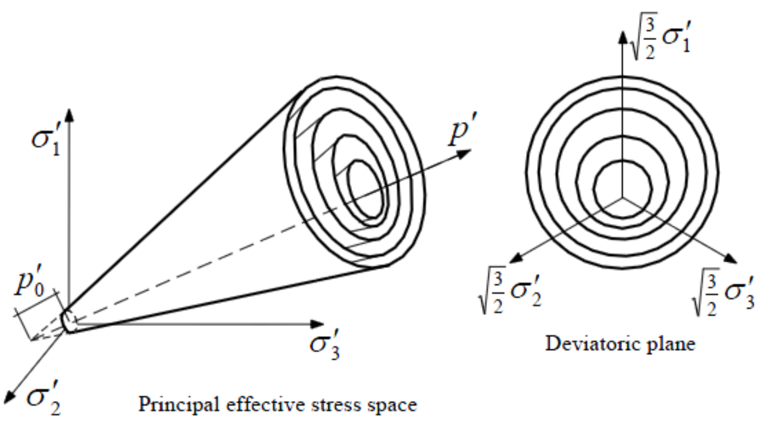

Figure 4.2: Conical multi-yield surfaces in principal stress space and deviatoric plane (Prevost 1985; Parra 1996; Yang 2000).

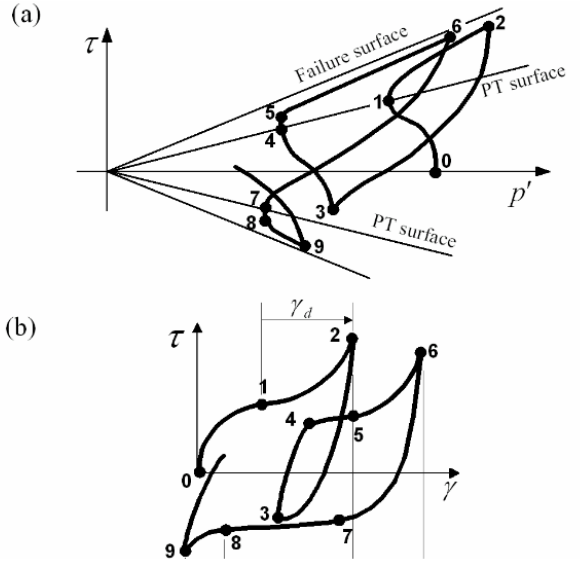

Figure 4.3: Shear stress-strain and effective stress path under undrained shear loading conditions (Yang and Elgamal 2002; Yang et al. 2003).

Clay material is modeled as a nonlinear hysteretic material (Parra 1996; Yang 2000; Yang et al. 2003) with a von Mises multi-surface (Iwan 1967; Mroz 1967) kinematic plasticity model, as shown in Figure 4.4. In this regard, emphasis is placed on reproduction of the soil hysteretic elasto-plastic shear response (including permanent deformation). In this material, plasticity is exhibited only in the deviatoric stress-strain response. The volumetric stress-strain response is linear-elastic and is independent of the deviatoric response. This constitutive model simulates monotonic or cyclic response of materials whose shear behavior is insensitive to the confinement change. Plasticity is formulated based on the multi-surface (nested surfaces) concept, with an associative flow rule. In the clay model, the nonlinear shear stress-strain backbone curve is represented by the hyperbolic relation (Kondner 1963), defined by two material constants, low-strain shear modulus and ultimate shear strength.

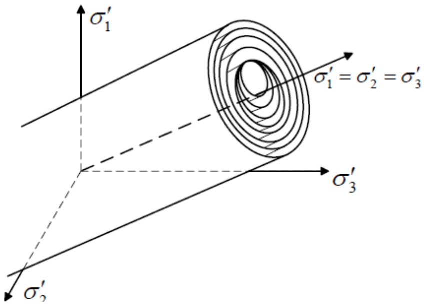

(a) von Mises multi-surface

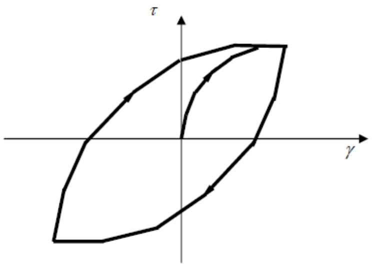

(b) Hysteretic shear

Figure 4.4: von Mises multi-surface kinematic plasticity model
(Yang 2000; Yang et al. 2003).

4.4.1.2 Pile material modeling

The concrete material was modeled by the uniaxial Kent-Scott-Park concrete material with degraded linear unloading/reloading stiffness according to the work of Karsan-Jirsa and no tensile strength (Mazzoni et al. 2006). The stress-strain relationships and material parameters are shown in Figure 4.5. The parameter description and specific values used in this analysis are listed in Table 3.1.

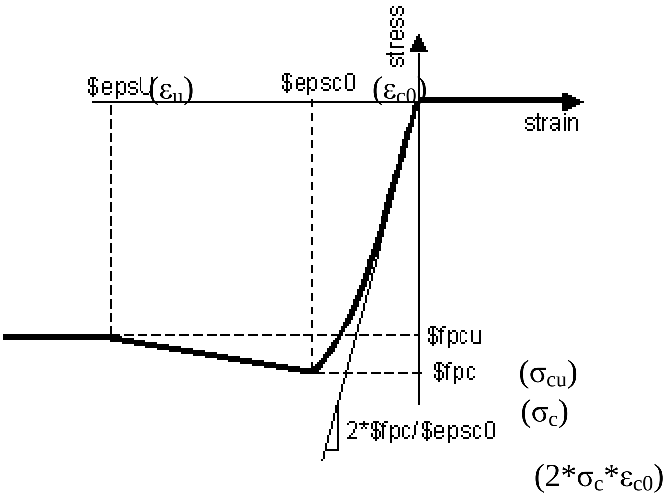

Figure 4.5: Stress-strain relationships and material parameters for concrete (Mazzoni et al. 2006).

The steel material was modeled by the uniaxial bilinear steel material model with kinematic hardening and optional isotropic hardening, described by a nonlinear evolution equation (Mazzoni et al. 2006). The stress-strain relationships and material parameters are shown in Figure 4.6. The parameter description and specific values used in this study are listed in the next section.

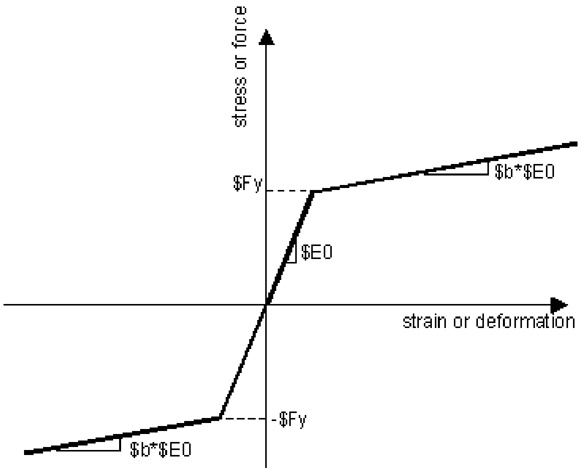

Figure 4.6: Stress-strain relationships and material parameters for steel (Mazzoni et al. 2006).

4.4.2 Nonlinear beam column element

A three-dimensional nonlinear beam-column element, shown in Figure 4.7, was used to simulate the piles supporting the bridge. This force-based beam-column element with non-iterative or iterative force formulation considers the spread of plasticity along the element (Mazzoni et al. 2006). In this element, each node has six degrees of freedom, including translations in the *x*, *y*, and *z* directions and rotations about the *x*, *y*, and *z* directions. Element property is represented by the section model identified at each integration point. The element response is obtained by integration of the section response, based on the Gauss-Lobatto quadrature rule (Mazzoni et al. 2006).

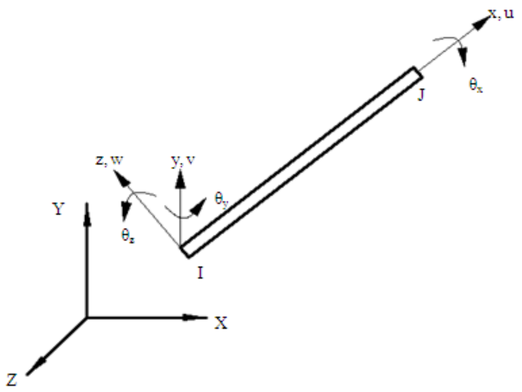

Figure 4.7: A nonlinear beam-column element.

4.4.3 Elastic beam column element

An elastic beam column element (Mazzoni et al. 2006) was used to model the rigid link that connects beam nodes with soil nodes in the soil–pile system (see Figure 4.8), in order to account for the pile-size effects. The element is three-dimensional, with six degrees of freedom at each node (i.e. translations in the *x*, *y*, and *z* directions and rotations about the *x*, *y*, and *z* directions). The property of this element is defined directly with the cross-section area, Young’s modulus, shear modulus, and second moment of area about the local *y* and *z* axis).

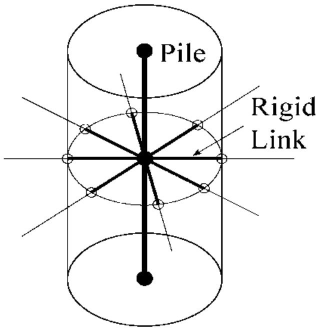

Figure 4.8: Pile–soil coupling by rigid links.

4.4.4 BrickUP Element

BrickUP (Mazzoni et al. 2006), shown in Figure 4.9, is an 8-node hexahedral linear isoparametric element. Each node has four degrees of freedom (DOF): DOFs 1 to 3 for solid displacements (u_x, u_y, and u_z) and DOF 4 for fluid pressure (p). This element is implemented for simulating the dynamic response of fully coupled solid-fluid material, based on Biot's theory of porous medium. We used BrickUP to model soils.

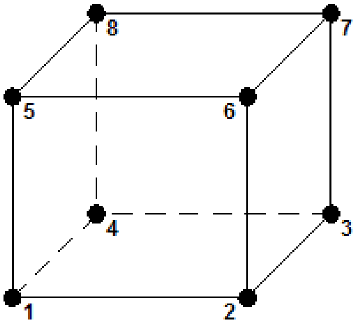

Figure 4.9: BrickUP element.

4.5 Numerical Simulation of the Soil–Pile System

A three-dimensional FE model of the seasonally frozen soil and concrete-filled steel-pipe pile was constructed by utilizing OpenSeesPL. We used this model to obtain the equivalent depth of fixity of the pile based on the concept of equivalent cantilever.

4.5.1 Finite element model of the soil–pile system

Two types of piles were used in the bridge: a 24-inch-diameter pile with a length of 45 feet and a 36-inch-diameter pile with a length of 60 feet. These two types of pile were considered for four different soil conditions of varying frozen soil depth. Due to symmetry, a half-model was used for the soil–pile system. As an example, Figure 4.10 (a) shows a mesh of the 36-inch pile embedded in 4 feet of frozen soil and the detail of the mesh around the pile. The model has a length of 80 feet (*X* or longitudinal direction) and a width of 40 feet (*Y* or transverse direction). The total thickness of the soil domain is 80 feet, with 20 feet below the pile tip. The mesh was refined to minimize the mesh effects.

In these models, the following boundary conditions were enforced: (1) The bottom of the domain was fixed in the longitudinal (*X*), transverse (*Y*), and vertical (*Z*) directions; (2) Left, right, and back planes of the mesh were fixed in the *X* and *Y* directions and free in the *Z* direction; and (3) Plane of symmetry was fixed in the *Y* direction and free in the *Z* and *X* directions.

The pile cross section was discretized into an array of fibers, as shown in Figure 4.10 (b) and (c). Three regions were identified to represent the confined concrete, the longitudinal steel reinforcement, and the steel pipe.

For these models, pushover analysis was conducted with lateral displacement applied at the pile head in the longitudinal direction to simulate lateral loading. The corresponding force at the pile head was recorded with the increasing of displacement.

In order to compare the lateral stiffness of the soil–pile system for two different piles (24-inch pile and 36-inch pile) with various soil conditions to the equivalent fixed-base cantilever, a corresponding cantilever model was established to conduct pushover analysis. For each frozen soil condition, the lateral stiffness was evaluated for the cantilever with different length. If the lateral stiffness for a certain length of cantilever was equal to that of the soil–pile system, the cantilever length was determined to be the equivalent length of the soil–pile system.

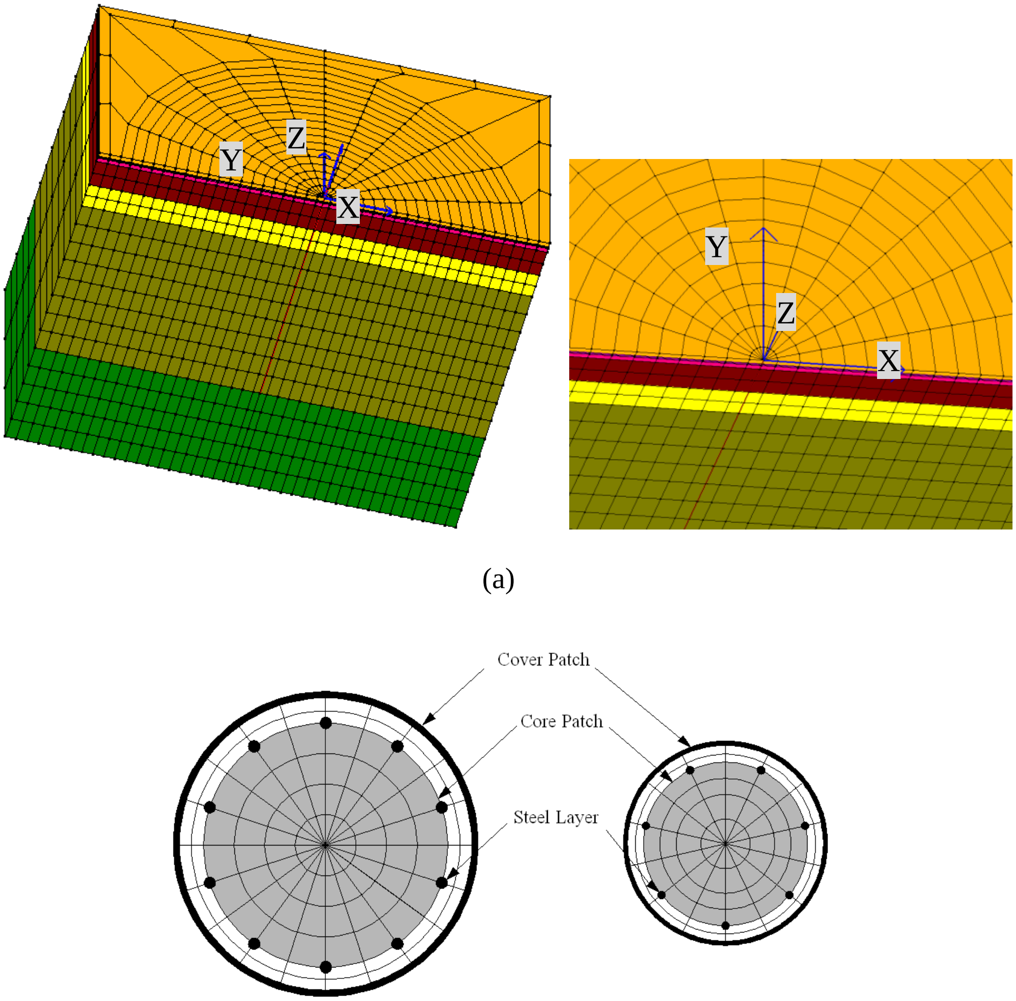

(a)

(b) (c)

Figure 4.10: Finite element model of the soil–pile system: (a) isotropic view of the entire model and detailed mesh around the pile; (b) fiber section of the 36-inch pile; and (c) fiber section of the 24-inch pile.

4.5.2 Material modeling

This section discusses the material modeling, including the pile material modeling and soil material modeling, and the parameters used for each material.

4.5.2.1 Pile material modeling

An enhancement in the flexural strength and ductility of the pile element can be expected due to the increase in concrete compressive strength and corresponding strain resulting from the confining action of the steel pipe (Yang et al. 2008). Mander et al. (1988a, 1988b) proposed a constitutive model for the concrete core to account for the confining effect based on Elwi and

Murray (1979). The compressive strength and corresponding strain in the presence of lateral pressure can be evaluated by using Equation (4.1) and Equation (4.2), respectively (Mohamed 2006).

$$f'_{cc} = f'_{co}(2.254\sqrt{1+\frac{7.94 f'_l}{f'_{co}}} - \frac{2 f'_l}{f'_{co}} -1.254) \tag{4.1}$$

$$\varepsilon_{cc} = \varepsilon_{co}\left[1+5(\frac{f'_{cc}}{f'_{co}}-1)\right] \tag{4.2}$$

where f_{CC}' and ε_{CC} are the compressive strength and corresponding strain of confined concrete; f_{CO}' and ε_{CO} are the compressive strength and corresponding strain of unconfined concrete; and f_l' is the effective lateral confining pressure exerted on the core concrete by the steel pipe at yield.

It is known that cold temperature causes significant increase in the compressive strength of concrete (Lee et al. 1988a, 1988b; Sritharan et al. 2007; Montejo et al. 2008). According to Montejo et al. (2008), when the moisture content of concrete is 3%, the increase of concrete compressive strength is about 20% at -20°C (-4°F) compared with that at 20°C (68°F).

The unconfined compressive strength of the concrete (Class AA) used in this project is 5.0 ksi at room temperature, and the unconfined compressive strength of the concrete was assumed to be 6.0 ksi at -20°C (-4°F). By using Equations (4.1) and (4.2), the corresponding confined compressive strength and strain at 20°C (68°F) and -20°C (-4°F) are 12.9 ksi and 14.5 ksi, respectively. Crushing strain increases also, from 0.004 for unconfined concrete to 0.03 for well-confined concrete. Table 4.1 and Table 4.2 summarize the material properties of core concrete and steel used in this study.

The impact of cold temperature on the properties of steel is not as significant. Filiatrault and Holleran (2001) reported that the change in temperature from 23°C (73°F) to -20°C (-4°F) increased the steel yield and ultimate strengths by only 4.5%, and the ultimate strain and the elastic modulus did not change with temperature. In this model, the steel properties were assumed constant at all temperatures, as shown in Table 4.2.

Table 4.1: Material Properties of Core Concrete

Material Parameters	20°C		-20°C	
	Unconfined	Confined	Unconfined	Confined
Compressive Strength at 28 Days $fpc (σc)	5.0 ksi	13.0 ksi	6.0 ksi	14.5 ksi
Strain at Maximum Strength $epsc0 (εc0)	0.003	0.02	0.003	0.02
Crushing Strength $fpcu (σcu)	4	9.7	5*	13.0
Strain at Crushing Strength $epsU (εu)	0.004	0.03	0.004	0.03

Table 4.2: Material Properties of Steel

	Material Parameters	
Reinforcing Steel (ASTM A706)	Yield strength ($Fy)	60 ksi
	Initial elastic tangent ($Eo)	30,000 ksi
	Strain-hardening ratio ($b)	0.01
Steel Pipe (ASTM A709)	Yield strength ($Fy)	50 ksi
	Initial elastic tangent ($Eo)	30,000 ksi
	Strain-hardening ratio ($b)	0.01

4.5.2.2 Soil material modeling

The soil property for each layer was obtained from a geotechnical report generated by DOWL Engineers (2005). As shown in Figure 4.11, a test boring TB-59 was drilled within the bridge's vicinity in March 2004. The boring log for TB-59 is shown in Appendix A (Figure A.0.1). A downhole shear-wave velocity survey was performed in TB-59. A shear wave velocity measurement was started from 6 feet below the ground surface and continued to a depth of approximately 150 feet.

The profile of shear wave velocity is shown in Appendix B (Figure B.0.2). However, in this project it is essential to know the soil property in the top 6 feet, which is the maximum frozen depth expected at this bridge site.

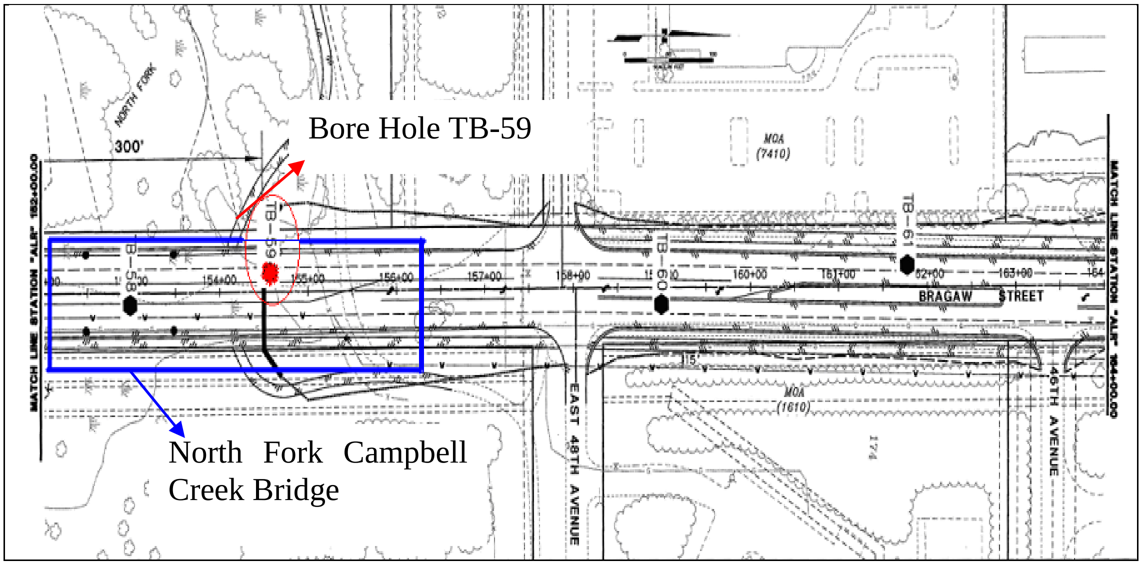

Figure 4.11: The location of North Fork Campbell Creek bridge and test borehole TB-59 (DOWL Engineers 2005)

Based on previous testing results (Czajkowski and Vinson 1980; LeBlanc et al. 2004), the shear wave velocity was assumed at 3,000 feet/second and 250 feet/second for fully frozen and unfrozen peat, respectively. For the transition layers (i.e., 0.5-foot-thick layer assumed for the surface soil and the soil between seasonally frozen layer and the unfrozen layer (Yang et al. 2010), the shear wave velocity was taken as 2,000 feet/second for the frozen case. Shear wave velocity profiles for the top 6 feet in different soil conditions are presented in Figure 4.12. The 24-inch pile was covered by gravel on the top 6 feet, and no frozen condition was anticipated in the field.

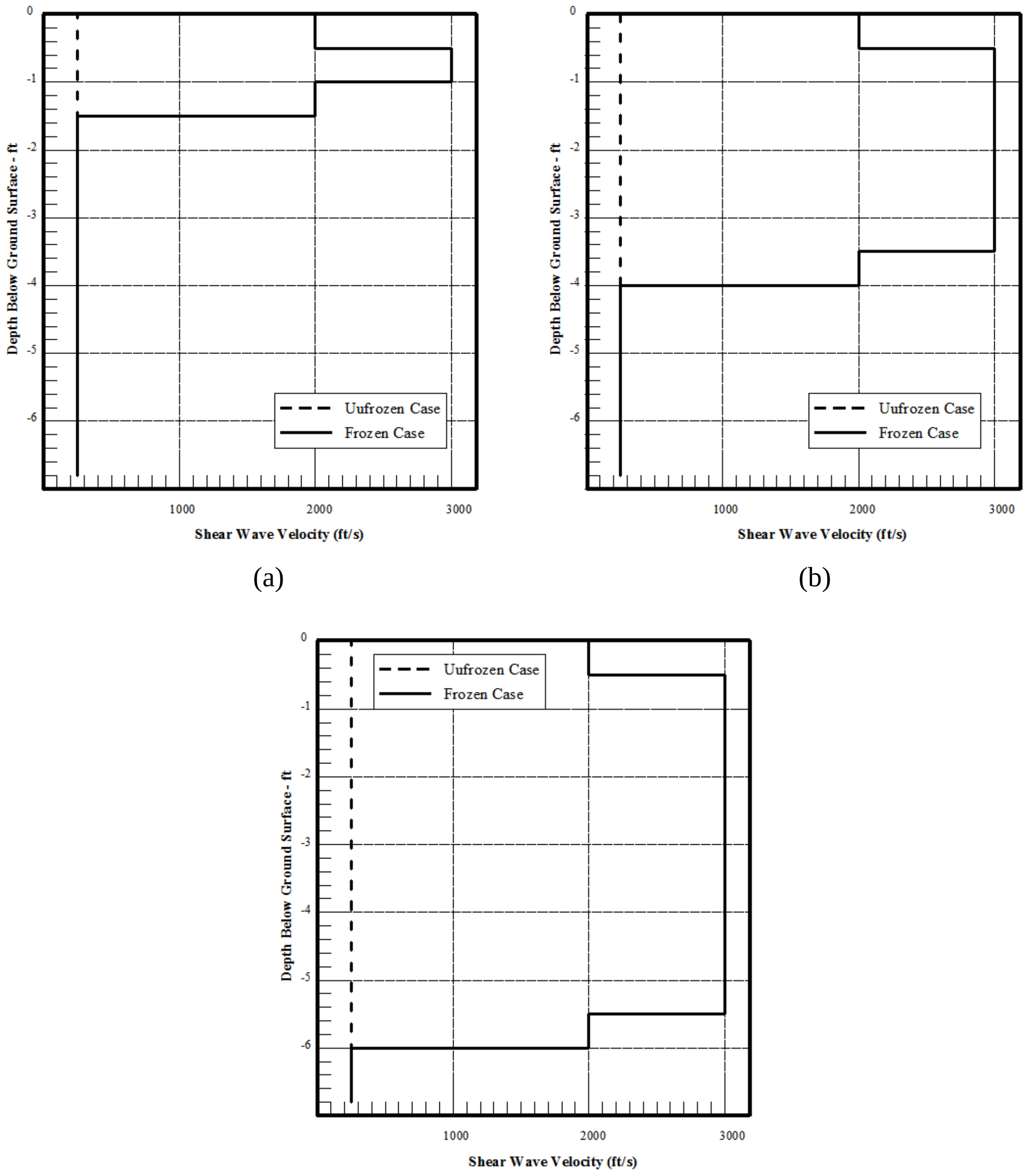

(a)

(b)

(c)

Figure 4.12: Shear wave velocity profile of the test site: (a) frozen depth is 1.5 feet; (b) frozen depth is 4 feet; and (c) frozen depth is 6 feet.

Based on test boring information, the soil profile was divided into four layers, as illustrated in Figure 4.13, for the top 80 feet below ground surface. The engineering properties for each layer are listed in Table 4.3.

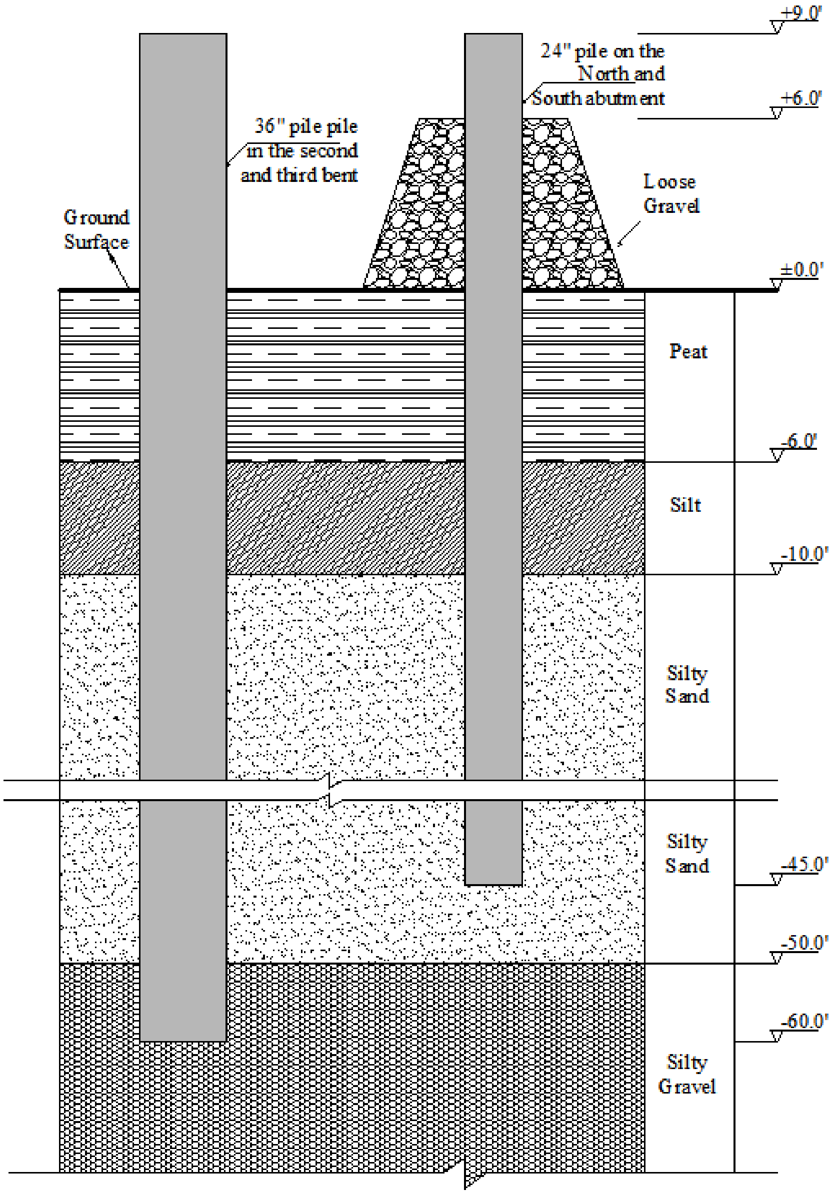

Figure 4.13: Soil profile of the bridge site.

Table 4.3: Summary of the Soil Properties

Depth (feet)	Soil Type	Season	Mass Density (pcf)	E* (ksi)	ν**	Friction Angle (deg)	Cohesion (psi)
-6.0-0 (24-inch Pile)	Gravel	Winter /Summer	110	1.3	0.3	29	0
0-0.5 Transition Layer	Peat	Winter	70	110	0.3	0	14.5
		Summer	70	0.7	0.3	0	0. 145
0.5-5.5 Active Layer	Peat	Winter	70	110	0.3	0	14.5
		Summer	70	0.7	0.3	0	0.145
5.5-6.0 Transition Layer	Peat	Winter	70	110	0.3	0	14.5
		Summer	70	0.7	0.3	0	0.145
6.0-10.0	Silt	Winter /Summer	125	14	0.3	15	0
10.0-50.0	Silty Sand	Winter /Summer	130	14	0.3	30	0
50.0-80.0	Silty Gravel	Winter /Summer	145	20	0.3	30	0

* Young’s Modulus
** Poisson's Ration

4.5.2.3 Single element simulation

One-element numerical simulation was conducted to illustrate the stress-strain behavior and unconfined compressive strength for frozen and unfrozen soils. Figure 4.14 shows the simulation setup. Pressure was exerted on top of the element after gravity application. The properties of peat, as previously discussed , in frozen and unfrozen conditions were input into the model. The stress-strain curves for frozen and unfrozen peats are shown in Figure 4.15. From this figure, the difference in the stress-strain behavior and the compressive strength between frozen and unfrozen peats can easily be seen.

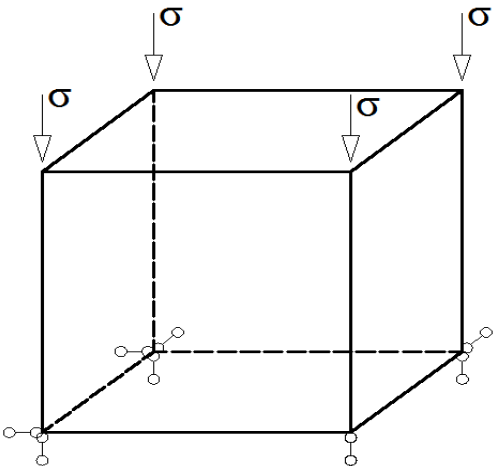

Figure 4.14: One-element unconfined compression test setup.

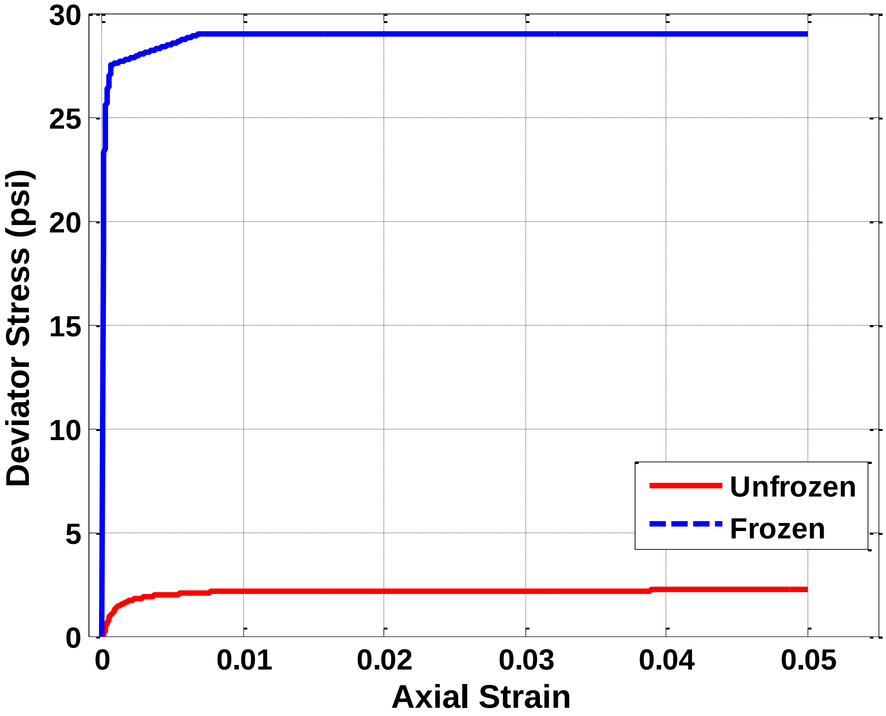

Figure 4.15: Stress-strain curve.

4.5.3 Simulation results

The earthquakes observed were small local events and the accelerations observed on the bridge were quite small. Therefore, only small deformation behavior was considered, and the lateral stiffness of the pile and soil–pile system at the elastic stage was compared to obtain the depth of fixity. The lateral load-displacement curves for various lengths of cantilever (thin line) and soil–

pile system (thick line) in different soil conditions are presented in Figure 4.16 for the 24-inch pile and in Figure 4.17 for the 36-inch pile.

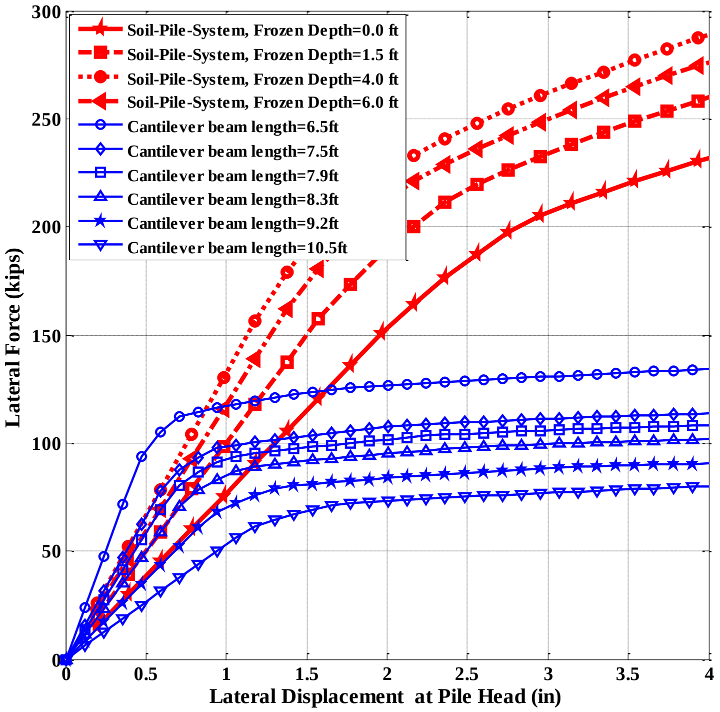

Figure 4.16: Lateral load vs. displacement for 24-inch pile.

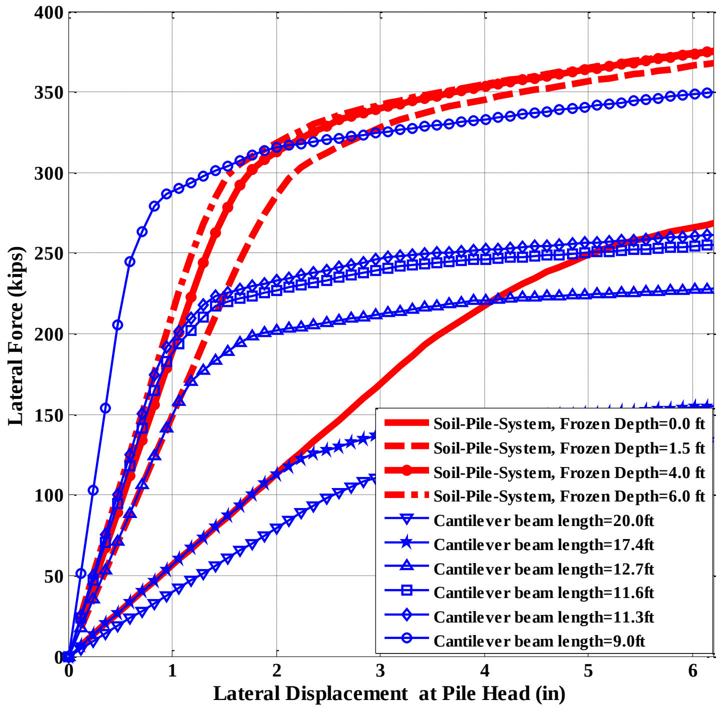

Figure 4.17: Lateral load vs. displacement for 36-inch pile.

The ratio of lateral force to displacement was used to evaluate the lateral stiffness of the pile and the soil–pile system at the elastic stage. As shown in Figure 4.16 and Figure 4.17, the slope of the thick curves; that is, the lateral stiffness of the soil–pile system at the elastic stage increases with increasing depth of frost. Take the 36-inch pile, for example. When the lateral deflection at the pile head reaches 1.5 inches, the corresponding lateral forces are 89.2 kips, 242.7 kips, 281.6 kips, and 300.4 kips for unfrozen ground, 1.5 feet, 4 feet, and 6 feet of frozen soil, respectively. Compared with unfrozen conditions, the lateral load increases about 172% when frozen depth is 1.5 feet. When the frozen depth increases to 4 and 6 feet, the lateral load increases 216% and 237%, respectively. The effects of frozen depth on the increase of lateral load diminish as frozen soils penetrate deeper. Since the 24-inch piles are covered by loose gravel above the ground surface, the 24-inch pile–soil system is not as sensitive to frost depth as the 36-inch pile–soil system. For the cantilever model, lateral stiffness, shown as thin lines in Figure 4.16 and Figure 4.17, increases with reducing cantilever length. Note that the yield load of the cantilever is much lower than the soil–pile system in most cases.

If the lateral load-displacement curves for the soil–pile system and the cantilever with certain length coincide in the elastic stage, an equivalent cantilever is achieved. Take the 36-inch pile embedded in unfrozen soil condition, for example. As seen in Figure 4.17, the straight-line part of the soil–pile system with 1.5 feet of frozen soil almost coincides with the straight-line part of the 17.4-foot-long cantilever at the elastic stage. This indicates that the equivalent cantilever length is 17.4 feet. The equivalent lengths for the soil–pile systems with different frost depth penetration are summarized in Table 4.4.

Table 4.4: Equivalent Cantilever Length for the Soil–Pile System.

Frost Depth (feet)		0	1.5	4.0	6.0
Equivalent Length (feet)	36-inch Pile	17.4	12.7	11.6	11.3
	24-inch Pile	9.2	8.3	7.9	7.5
Equivalent depth of fixity (feet / xD)	36-inch Pile	8.4 (2.80D)	3.7 (1.23D)	2.6 (0.87 D)	2.3 (0.77 D)
	24-inch Pile	3.2 (1.60D)	2.3 (1.15D)	1.9 (0.95 D)	1.5 (0.75 D)

As shown in Table 4.4, with increased frost depth, the equivalent length of the soil–pile system decreases. For the 36-inch pile, when frost depth reaches 1.5 feet, the equivalent length of the soil–pile system decreases 27% when compared with its length in unfrozen condition. With increased frost depth, the equivalent length continues to decrease. Decreases of 33% and 35%

are found when the depth of frozen ground reaches 4 feet and 6 feet, respectively. However, the effect of frozen ground on the depth of fixity diminishes with increasing frost depth. At 6 feet of frost depth, the equivalent depth of fixity is 0.75D, compared with 2.8D for the 36-inch pile at unfrozen condition, where *D* is the pile diameter.

4.6 Numerical Simulation of the Bridge

With the equivalent cantilever length at a different soil condition for each soil–pile system, a simplified model for the bridge superstructure was built by utilizing OpenSees to conduct modal analysis.

4.6.1 Finite element model of the bridge

A simplified FE model of bridge superstructure was developed for modal analysis. Figure 4.18 shows a three-dimensional view of a FE model. Since the transverse stiffness of the bridge dominates the bridge seismic behavior and the vibration of the bridge girders was not the primary concern, the bridge superstructure was simplified as three girders fixed on the cap beam.

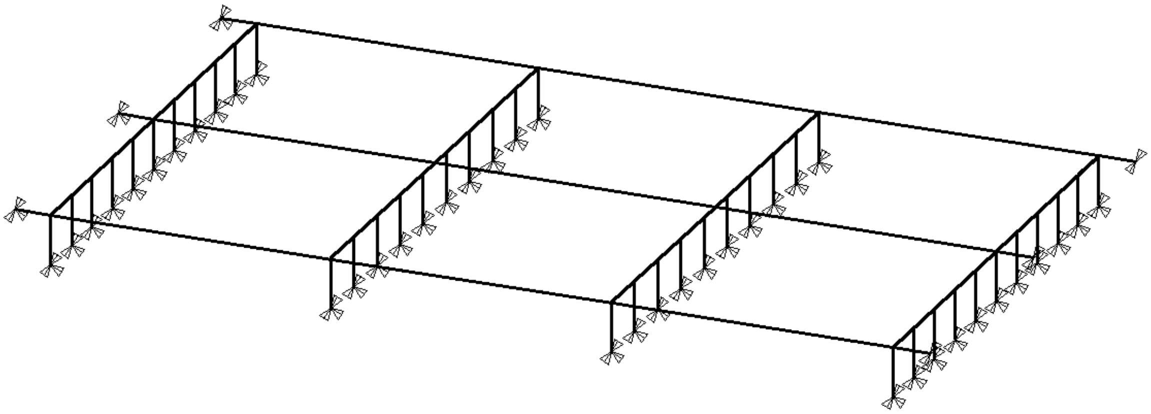

Figure 4.18: A simplified 3D FE model of the bridge superstructure.

In this model, the girders, cap beams, and piles were modeled by two-node beam-column elements. There are 249 nodes and 248 elements in this model. All piles were fully fixed at the depth of fixity. In the longitudinal direction, the left ends of the three girders were fully fixed; on the right side of the girders, the translational DOF was free in the longitudinal direction to account for the restrained action from the adjacent structure. The mass of the bridge deck was distributed equally as lumped mass. The cap beam-girder joints were fixed in translational directions, allowing rotation between the cap beam and bridge girder.

4.6.2 Modal analysis results

Modal analysis was carried out to analyze the dynamic characteristics of the North Fork Campbell Creek Bridge in terms of natural frequency and mode shapes under various frozen soil depths. The FE modal analysis was validated by experimental data. The first transverse modal frequency and shape identified from field-monitoring results for the case with 2 feet of frozen soil were used to calibrate the FE model in terms of superstructure mass and stiffness. The calibrated model was then used to predict the dynamic characteristics of the bridge for other conditions by only varying the depth of fixity of the piles (results presented in Table 4.5). For example, the modal shape of the first transverse mode is shown in Figure 4.19. Note in Table 4.5 that the first transverse modal frequency of the bridge predicted by the calibrated FE model agrees well with the field test results for cases of no frost and 4 feet of frost. For the case with 6 feet of frost, the predicted first transverse modal frequency is 7.9 Hz, representing a 230% increase, compared with the case of no frost.

Table 4.5: Comparison between Identified and Calculated Results and
the First Transverse Frequencies Calculated by the FE Model

	Calculated		Identified	Different between Calculated and Identified Data
Frost Depth	The First Transverse Frequency(Hz)	Percentage Increase		
0 feet (Unfrozen Soil)	2.416	0.0%	2.528	4.6%
2.0 feet	4.960	105.3%	5.020	1.2%
4.0 feet	7.336	203.6%	7.579	3.3%
6.0 feet	7.938	228.6%		

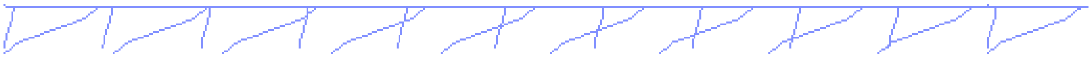

(a) YZ Plane

(b) XZ Plane

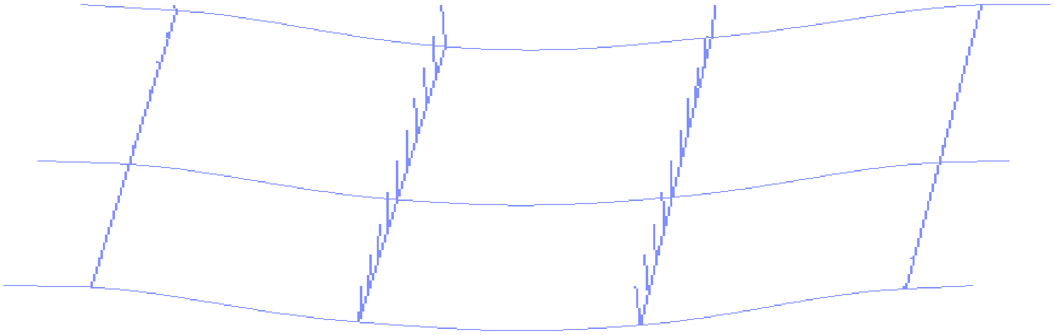

(c) XY Plane

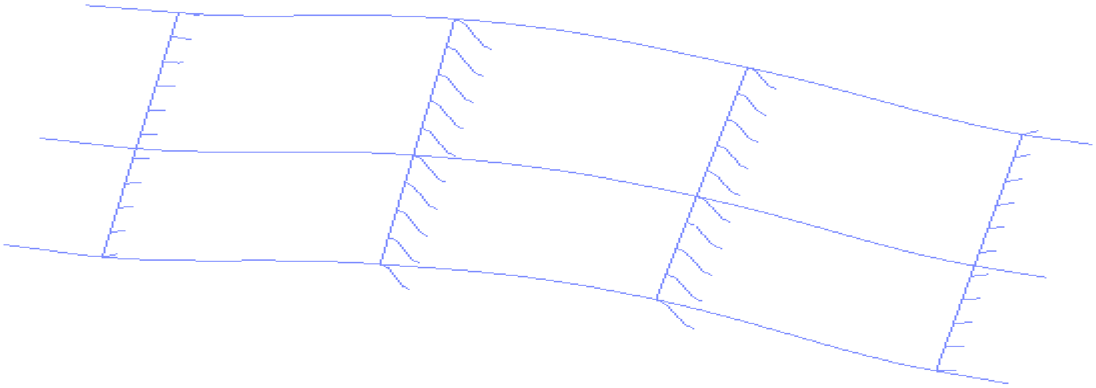

(d) 3D

Figure 4.19: The first transverse mode shape.

4.7 Conclusions and Discussion

Finite element models for the soil–pile system bridge superstructure of North Fork Campbell Creek Bridge were constructed to analyze the bridge dynamic properties. Pushover analysis was conducted by using the soil–pile system model to obtain the equivalent depth of fixity at various frost depths. A simplified FE of the bridge superstructure was constructed by using the depth-of-fixity results and calibrated by using field-monitoring results obtained for the case with 2 feet of frozen soil. The calibrated model was then used to predict the bridge dynamic properties at other conditions.

We found that the pile equivalent length becomes shorter when frost depth increases. When frost depth is 6 feet, the equivalent length is 0.75 pile diameter for a 36-inch pile, compared with 2.8 pile diameter in unfrozen condition. The predicted bridge transverse modal frequency with the simplified bridge model matches well with that obtained from field monitoring. The first transverse modal frequency increased greatly with the increase of frost depth. When frost depth reaches 6 feet, the first transverse modal frequency increases about 230% compared with that at unfrozen condition. This finding is consistent with those from Yang et al. (2007a, 2007b) and Bai (2007).

CHAPTER 5. SIMPLIFIED DESIGN TOOL: FIXITY DEPTH APPROACH

5.1 Introduction

As mentioned in Chapter 2, two reinforced concrete-filled steel-pipe piles were constructed at an outdoor test site in Fairbanks in order to gather large deformation experimental data for validating design tools. Among other models, the equivalent fixed-base cantilever model is often used to analyze the response of laterally loaded piles. Based on the equivalent cantilever concept, the equivalent depth of fixity of a soil–pile system can be derived by equating the lateral stiffness of the cantilever to that of the elastic soil–pile system (Chai 2002). Several parameters, that is, depth-to-maximum moment, depth of fixity, and analytical plastic hinge length, are essential for the simplified design approach. This chapter discusses the approach used to evaluate these parameters. Based on this approach, a set of parameters was obtained based on the Fairbanks test data. Additionally, FE models were employed to predict the change of these parameters at various frost depths.

5.2 Effective Depth to Fixity

Figure 5.1 (a) shows a soil–pile system subjected to lateral load, with deflected shape and bending-moment profile. Figure 5.1 (b) and (c) demonstrate the equivalent fixed-base cantilever model based on the concept of depth-to-maximum moment and the equivalent lateral stiffness.

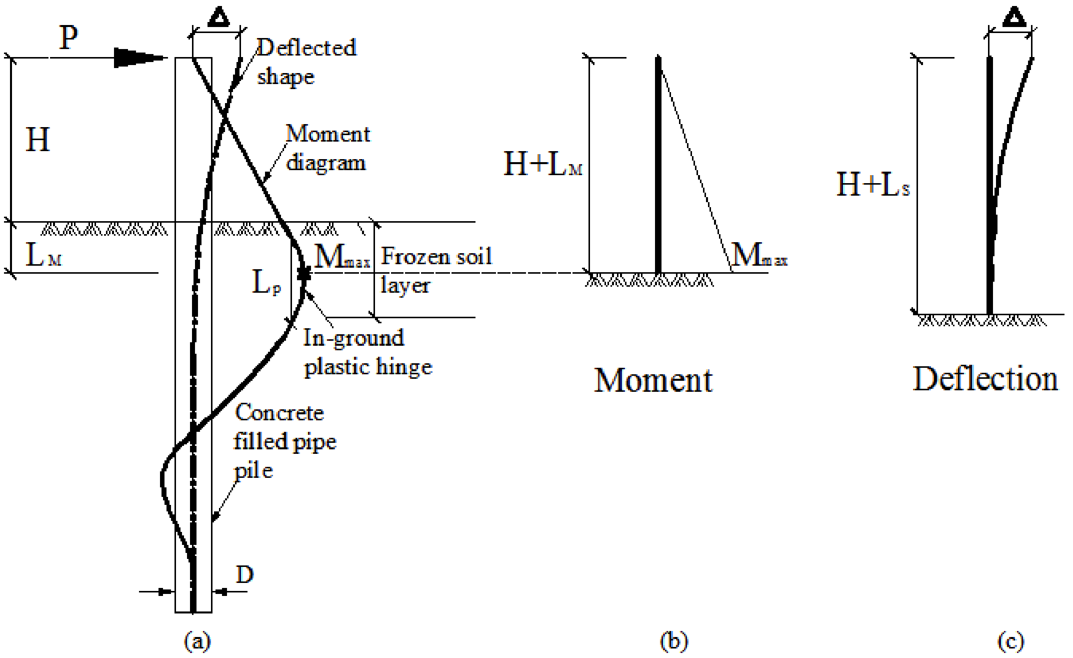

Figure 5.1: Effective depth of fixity.

5.2.1 Depth-to-maximum bending moment

The depth-to-maximum moment of a soil–pile system, L_M, can be computed by equating the maximum bending moment of the cantilever to that of the soil–pile system, as given by Equation (5.1).

$$L_M = \frac{M_{max}}{P_{max}} - H \tag{5.1}$$

where M_{max} is the maximum bending moment of the soil–pile system, P_{max} is the lateral force applied on the pile head, and H is the length of the pile above ground surface.

5.2.2 Equivalent depth of fixity

The lateral stiffness of the soil–pile system and that of the equivalent fixed-base cantilever can be obtained through Equations (5.1) and (5.2) (Chai 2002), respectively.

$$K_s = \frac{P_y}{\Delta_y} \tag{5.2}$$

$$K_c = \frac{3(EI)_{eff}}{(L_s+H)^3} \tag{5.3}$$

where $(EI)_{eff}$ is the effective flexural rigidity of the pile, Δ_y is the yield deflection, and P_y is the idealized yield force. Then, the equivalent depth of fixity, L_S, can be derived by equating the lateral stiffness of the cantilever to that of the elastic soil–pile system, shown in Equation (5.4).

$$\mathrm{L}_s = \sqrt[3]{\frac{3(\mathrm{EI})_{\mathrm{eff}}\Delta_\mathrm{y}}{\mathrm{P_y}}} - \mathrm{H} \tag{5.4}$$

5.3 Determination of Load-Displacement Response

Based on the aforementioned model, the depth of fixity of the test pile can be determined by trial and error until the equivalent system has the same load-displacement response as the actual soil–pile system (Juirnarongrit and Ashford 2005). The load-displacement response of an equivalent cantilever, which follows a bilinear model, can be determined through Equations (5.5) to (5.8) (Priestley et al. 2007).

$$\mathrm{P_y} = \frac{\mathrm{M_y}}{\mathrm{H+L_M}} \tag{5.5}$$

$$\Delta_\mathrm{y} = \frac{\emptyset_\mathrm{y}(\mathrm{H+L_s})^2}{3} \tag{5.6}$$

$$\mathrm{P_u} = \frac{\mathrm{M_u}}{\mathrm{H+L_M}} \tag{5.7}$$

$$\Delta_\mathrm{u} = \Delta_\mathrm{y} + \mathrm{L_p}\left(\emptyset_\mathrm{u} - \emptyset_\mathrm{y}\right)(\mathrm{H} + \mathrm{L_M}) \tag{5.8}$$

where M_y is the yield moment, $\emptyset_y$ is the yield curvature, Δ_y is the yield deflection, M_u is the ultimate moment, P_u is the ultimate force, $\emptyset_u$ is the ultimate curvature, and L_p is the analytical plastic hinge length.

To evaluate the pile section behavior, a moment curvature analysis was conducted on the test pile to evaluate the pile section behavior. The material properties of concrete and steel obtained from laboratory tests at room temperature are summarized in Table 5.1 and Table 5.2, respectively. The moment curvature relationship of the test pile is shown in Figure 5.2. We found that the effective yield curvature $\emptyset_y$ is 0.3×10^{-3} 1/in., the effective yield moment M_y is 7,420 kip-in., the ultimate curvature $\emptyset_u$ is 5.31×10^{-3} when the strain of the extreme tensile rebar is 5%, and the ultimate moment M_u is 8833 kip-in.

Table 5.1: Material Properties of Core Concrete

Material Parameters	68°F (20°C)		14°F (-10° C)	
	Unconfined	Confined	Unconfined	Confined
Compressive Strength at 28 Days (σ_c)	5.176 ksi	13.0 ksi	5.5 ksi	13.3 ksi
Strain at Maximum Strength (ε_{c0})	0.002	0.016	0.002	0.016
Crushing Strength (σ_{cu})	4.0 ksi	9.7 ksi	4.4 ksi/	10.7 ksi
Strain at Crushing Strength (ε_u)	0.004	0.032	0.004	0.032

Table 5.2: Material Properties of Steel

Material Parameters			
Ambient Temperature		68°F (20°C)	14°F (-10°C)
Reinforcing Steel	Yield strength σ_y	76.5 ksi	78.41 ksi
	Initial elastic tangent E_s	30,610 ksi	30,610 ksi
	Yield strain	0.0025	0.0025
	Strain-hardening ratio	0.02	0.02
Steel Pipe	Yield strength σ_y	57.2 ksi	58.63 ksi/
	Initial elastic tangent E_s	28,947 ksi	28,947 ksi
	Yield strain	0.002	0.002
	Strain-hardening ratio	0.02	0.02

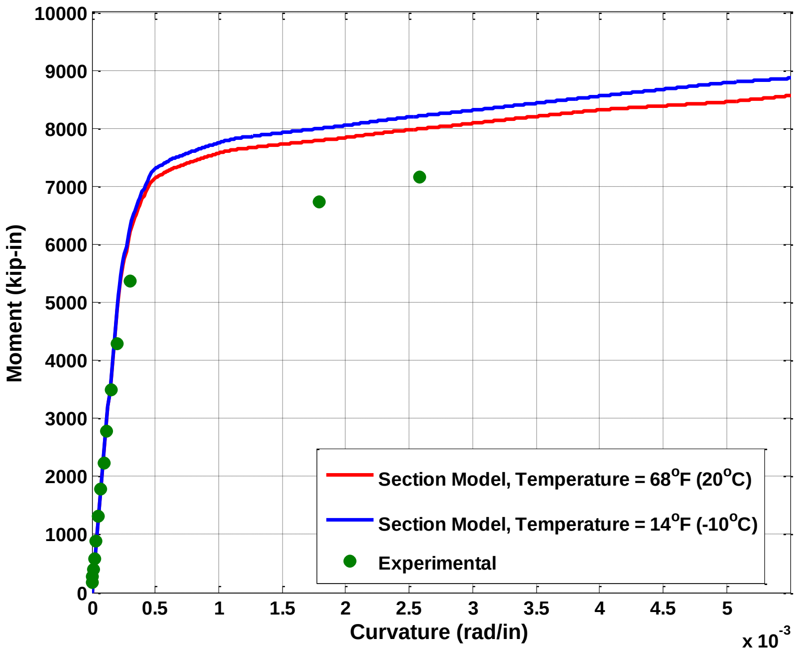

Figure 5.2: Moment-curvature relationship of the reinforced concrete-filled steel pile section.

For comparison purposes, the moment curvature analysis was conducted for the test pile in room temperature, as shown in Figure 5.2. This analysis indicates that the effective yield curvature $\emptyset_y$ is 0.225×10^{-3} 1/in., the effective yield moment M_y is 7,603 kip-in., the ultimate curvature $\emptyset_u$ is 5.55×10^{-3}, and the ultimate moment M_u is 8,571 kip-in. Figure 5.3 illustrates the relationship between flexural stiffness and curvature from the section analysis when the temperature is 14°F (-20°C).

The strain data recorded in the Fairbanks test were processed and used to evaluate the relationship between the bending moment and the curvature, based on the plane-strain assumption. This assumption surmises that the distribution of strain on the cross section of the pile is linear, and no slippage between the components of the pile, such as rebar, concrete, and steel pipe, occurs. As shown in Figure 5.2, the experimental data match well with the analytical results before the pile yielding. After yielding, the experimental data are quite different from the analytical results. This discrepancy is likely due to the distribution of strain on the pile cross section, which was no longer linear after the pile yielding, and to slippage that may have occurred between the steel pipe and concrete in this case.

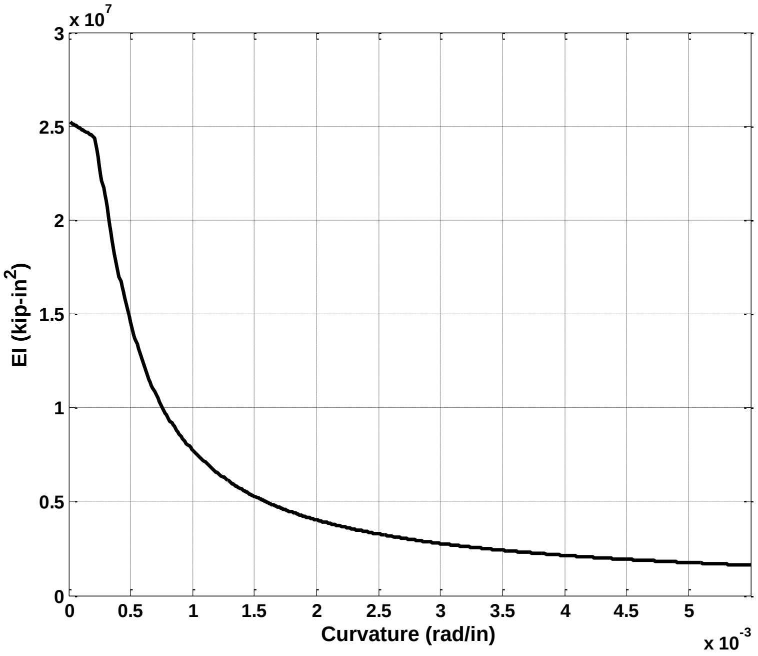

Figure 5.3: Flexural stiffness vs. curvature from section model for 14°F (-10°C).

The trial bilinear behavior of the soil–pile system can be obtained from the moment curvature-analysis results and Equations (5.5) through (5.8). After several iterations, the bilinear response matches well with the experimental results, as shown in Figure 5.4. The experimental data points shown in Figure 5.4 are the displacements at targeted loading cycles. The bilinear model was achieved by using L_M = 0.25D, L_S = 4.0D, and L_P = 2.0D, with D representing the pile diameter. In this prediction, the idealized yield displacement Δ_y = 1.08 in., the idealized yield force P_y = 167.7 kips, the ultimate displacement Δ_u = 8.39 in., and the ultimate load P_u = 199.6 kips.

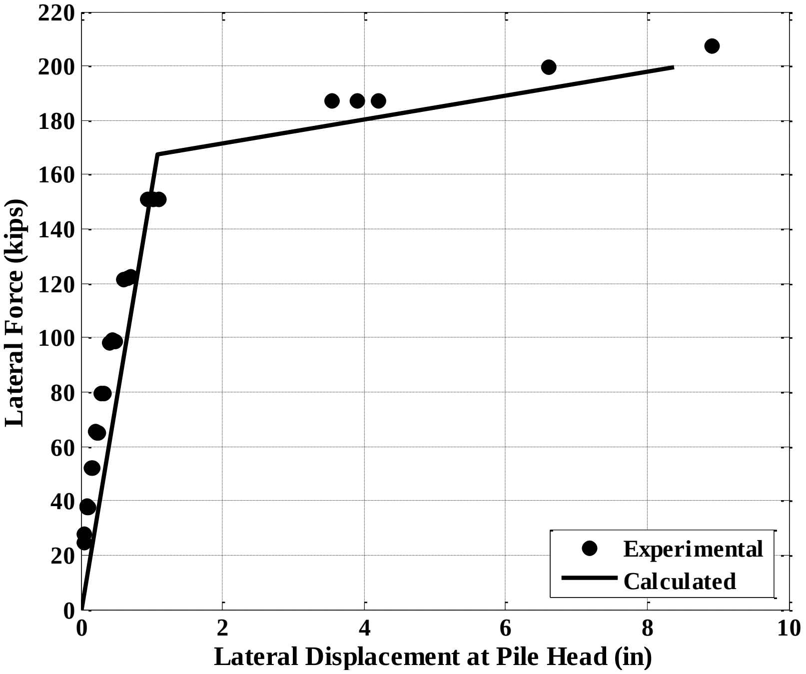

Figure 5.4: Lateral load-displacement response.

5.4 Variation of Load-Displacement Response with Frost Depth

In order to investigate the load-displacement response with different frost depth and obtain parameters for the fixity-depth approach for frozen soil conditions not included in the field test, three-dimensional FE models were constructed by using OpenSees (Mazzoni et al. 2006) and pushover analyses were performed. The test data obtained from 7.8 feet of frozen ground were used to calibrate and validate the FE model.

The shear wave velocity of unfrozen silt has been measured at 400 feet/second (Horazdovsky 2010). No in situ shear-wave velocity data are available for the seasonally frozen condition. The shear-wave velocity was assumed at 3,000 feet/second for the fully frozen silt, based on previous study results (Vinson 1978; LeBlanc et al. 2004). Soil material properties of the test site are listed in Table 5.3. The reference mean confinement, confinement dependence coefficient, and Poisson's ratio for each soil layer is 11.6 psi, 0.5, and 0.3, respectively. Fiber section was used to simulate the concrete-filled pipe pile. An interface layer between the pile and soil was used to model possible pile installation effects. The dimensions of the properties of the piles are presented in Chapter 2.

Table 5.3: Soil Properties of the Test Site in Winter Conditions with 7.8 Feet of Frost.

Depth (ft)	Mass Density (pcf)	Vs (ft/s)	Peak Shear Strain	Friction Angle	Cohesion (psi)
0~0.5	102	2250	3	5	43.5
0.5~1	102	2750	2	5	72.5
1~1.5	102	3000	1	5	58
1.5~2	102	2500	2	5	43.5
2~6	108	2250	2	5	18.125
6~6.5	108	2000	2	5	10.875
6.5~7	108	1500	4	5	7.25
7~7.5	108	1000	6	5	3.625
7.5~8	108	750	8	5	3.625
8~26	114	400	10	20	0.87
Interface	108	2000	3	5	14.5

Error! Reference source not found. compares the lateral load-deflection behavior from the experiment and FE modeling. **Error! Reference source not found.** and **Error! Reference source not found.** compare the rebar strain profiles from the experiment and FE modeling at a lateral load of 150 kips and 200 kips, respectively. In **Error! Reference source not found.**, the strain values at 150 kips lateral load from the experiment were the average value of three repeated loadings; there is large scattering in the strain data at a depth of -7.5 inches. In **Error! Reference source not found.**, the strain value at a depth of -7.5 inches reached the limit of the strain gage, and the strain gage limit of 2.8% was plotted. Results from the experiment and the FE modeling are generally in good agreement. At the lateral load of 207 kips, which is the maximum load applied in the experiment, maximum strain in the rebar reached 5%, as shown in **Error! Reference source not found.**, based on FE modeling. Figure 5.6 shows the bending-moment profile of the pile at a lateral load of 207 kips based on FE modeling.

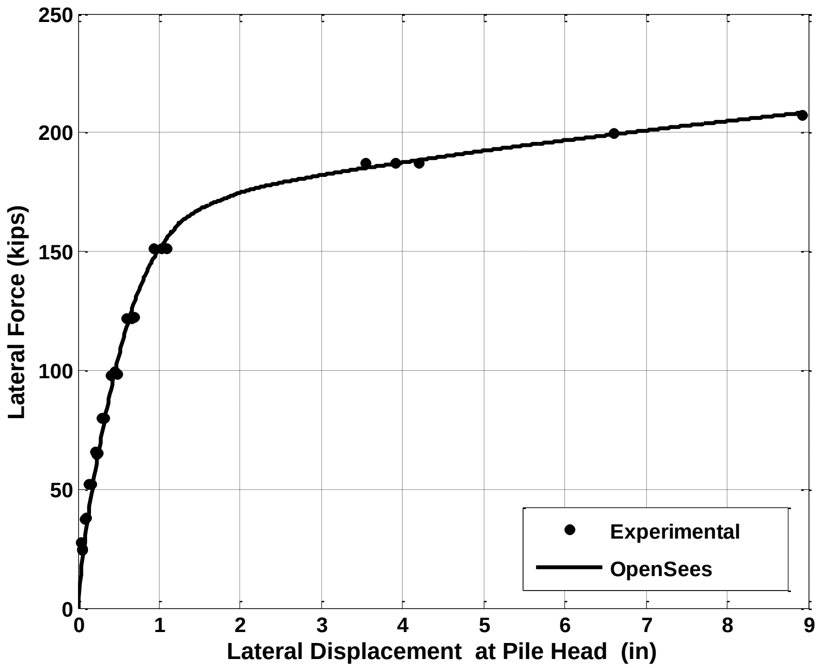

Figure 5.5: Comparison of lateral load-deflection curve.

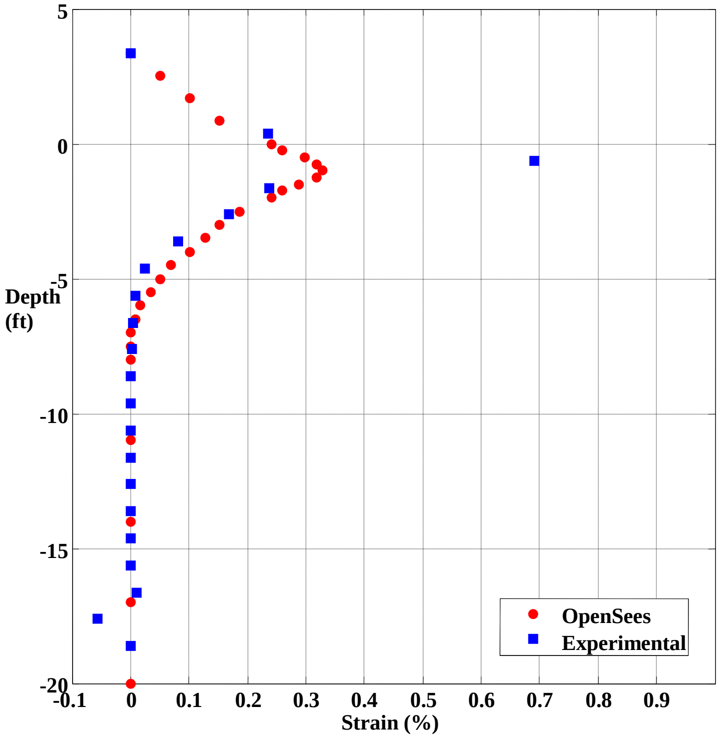

Figure 5.6: Comparison of rebar strain at a lateral load of 150 kips **Error! Reference source not found.**

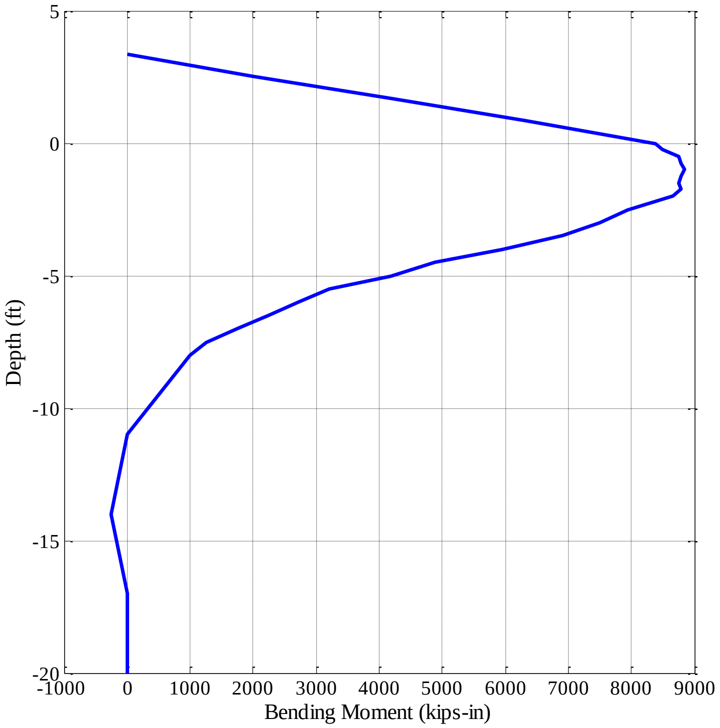

Figure 5.6: Bending-moment profile at a lateral load of 207 kips.

Four more FE models were constructed with frost depths varying from 0 (unfrozen) to 6 feet. The soil properties for each soil layer at various frost depth conditions are summarized in Table 5.4 to Table 5.7.

Table 5.4: Soil Properties When Frost Depth is 6 Feet

Depth (ft)	Mass Density (pcf)	Vs (ft/s)	Peak Shear Strain	Friction Angle	Cohesion (psi)
0~0.5	102	2250	3	5	43.5
0.5~1.0	102	2750	2	5	72.5
1.0~1.5	102	3000	1	5	58
1.5~2.0	102	2500	2	5	43.5
2.0~6.0	108	2250	2	5	18.13
6.0~6.5	108	2000	2	5	10.88
6.5~7.0	108	1500	4	5	7.25
7.0~7.5	108	1000	6	5	3.63
7.5~8.0	108	750	8	5	3.63
8.0~26.0	114	400	10	20	0.87
Interface	108	2000	5	5	14.5

Table 5.5: Soil Properties When Frost Depth is 4 Feet

Depth (ft)	Mass Density (pcf)	Vs (ft/s)	Peak Shear Strain	Friction Angle	Cohesion (psi)
0~0.5	102	2000	3	5	39.88
0.5~1	102	2500	2	5	68.88
1.0~1.5	102	2750	1	5	54.38
1.5~2.0	102	2500	2	5	39.88
2.0~2.5	108	2250	2	5	18.13
2.5~3.0	108	2000	2	5	10.88
3.0~3.5	108	1500	4	5	7.25
3.5~4.0	108	1000	6	5	3.63
4.0~20.0	114	400	10	5	0.87
20.0~26.0	114	400	10	20	0.87
Interface	108	2000	3	5	14.5

Table 5.6: Soil Properties When Frost Depth is 2 Feet

Depth (ft)	Mass Density (pcf)	Vs (ft/s)	Peak Shear Strain	Friction Angle	Cohesion (psi)
0~0.5	102	1750	3	5	29

0.5~1	102	2250	2	5	58
1.0~1.5	102	2500	1	5	43.5
1.5~2.0	102	1500	2	5	14.5
2.0~18.0	114	400	10	20	0.87
18.0~26.0	114	400	10	20	0.87
Interface	108	1500	3	5	14.5

Table 5.7: Soil Properties for Unfrozen Condition

Depth (ft)	Mass Density (pcf)	Vs (ft/s)	Peak Shear Strain	Friction Angle	Cohesion (psi)
0~4	102	330	10	20	0.87
4~8	108	400	10	20	0.87
8~26	114	400	10	20	0.87
Interface	108	400	10	20	0.87

Pushover analysis was performed for each case. For the unfrozen case, unfrozen condition experimental data were not used due to short rigid pile behavior. Instead, in situ soil test data including shear wave velocity and SPT data were used, and pile bottom was fixed in the FE model to simulate the long pile behavior. Figure 5.7 depicts the bending-moment profile for each case at a lateral load of 207 kips, when each pile has yielded. Observe that the maximum bending moment increases from 7,871 kip-inches in the unfrozen case to 8,841 kip-inches in the 7.8-foot frost case. The depth-to-maximum moment decreases from 5 feet (3.75 pile diameter) below the ground surface in the unfrozen case to 1 foot (0.75 pile diameter) below the ground surface in the 7.8-foot frost case. The results show that the shape of the bending-moment profile becomes much narrower when the ground freezes, indicating that the length of the plastic hinge region decreases substantially. This directly results in decreasing of the plastic hinge rotation and plastic deflection capacity of the pile when the ground freezes.

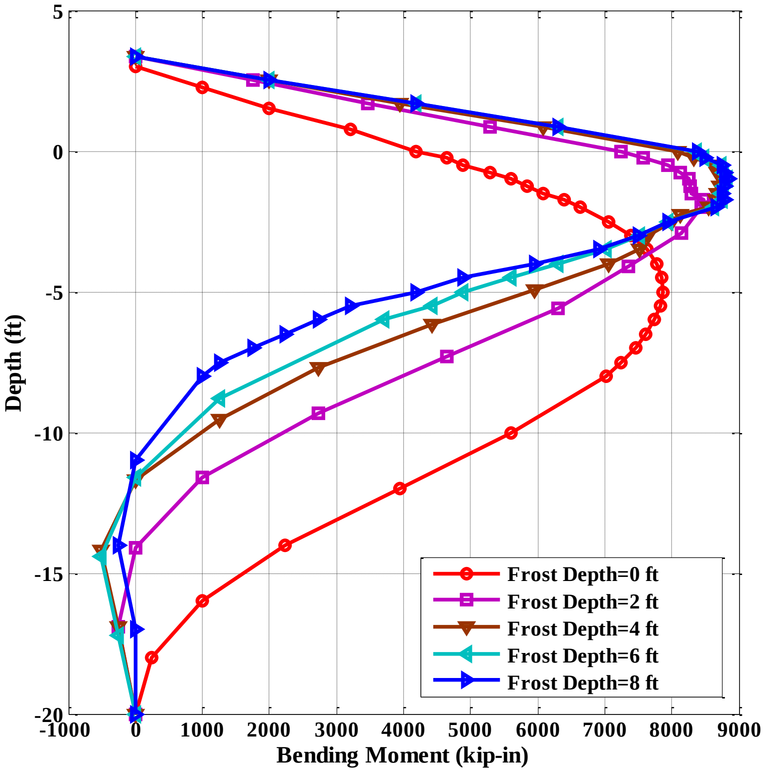

Figure 5.7: Bending-moment profile for each case at a pile head displacement of 8.9 inches.

The lateral load versus pile-head deflection relationship is illustrated in Figure 5.8 through Figure 5.12. The ultimate deflection in this case is defined as the pile deflection measured when the maximum rebar strain reaches 5%. Note that the ultimate load capacity of the soil–pile system increases from 124 kips to 208 kips, or a 68% increase, when the frost depth increases from 0 to 8 feet. However, with deeper frost depth, the displacement capacity of the soil–pile system drops from 27.4 inches to 8.8 inches, or a 68% decrease.

The bilinear load-deflection response was further evaluated by applying Equations (5.5) to (5.8). After several iterations, the bilinear response obtained from these equations matches well with that of the FE models for each case, as shown in Figure 5.8 to Figure 5.12. The values of L_M, L_S, and L_P for all cases are summarized in Table 5.8. As seen in Table 5.8, consistent drops in L_M, L_S, and L_P are observed when frost depth increases from 0 (unfrozen) to 7.8 feet: L_M decreases from 2.0D to 0.25D, L_S decreases from 11.0D to 4.0D, and L_P drops from 3.8D to 2.0D. The parameters for 4-, 6-, and 7.8-foot frost depths are very close, indicating that a 4-foot frost depth may be deemed the threshold separating frozen condition from unfrozen condition. For design purposes, we recommend that the parameters for an 8-foot frozen soil condition be used for Alaska.

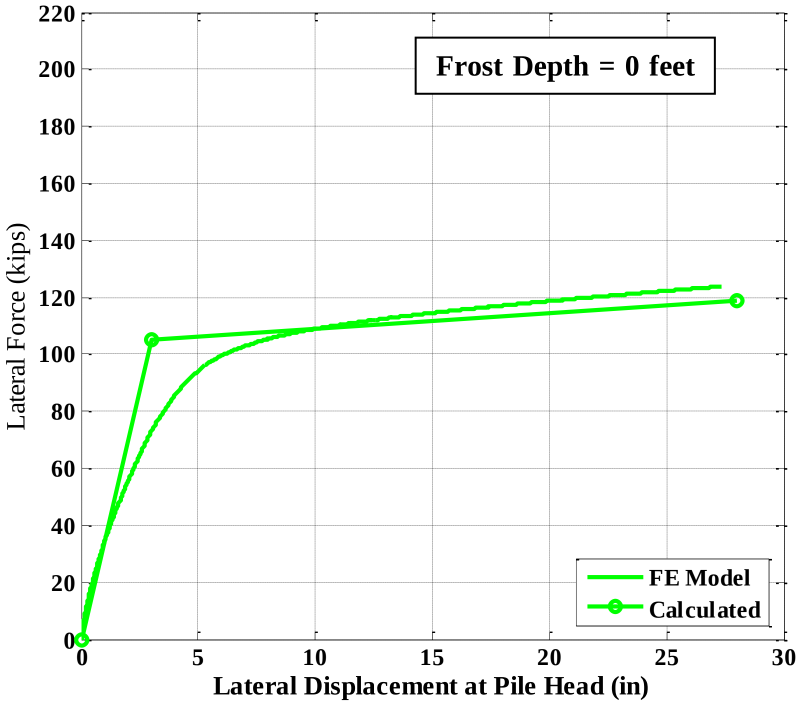

Figure 5.8: Load-displacement response for unfrozen case.

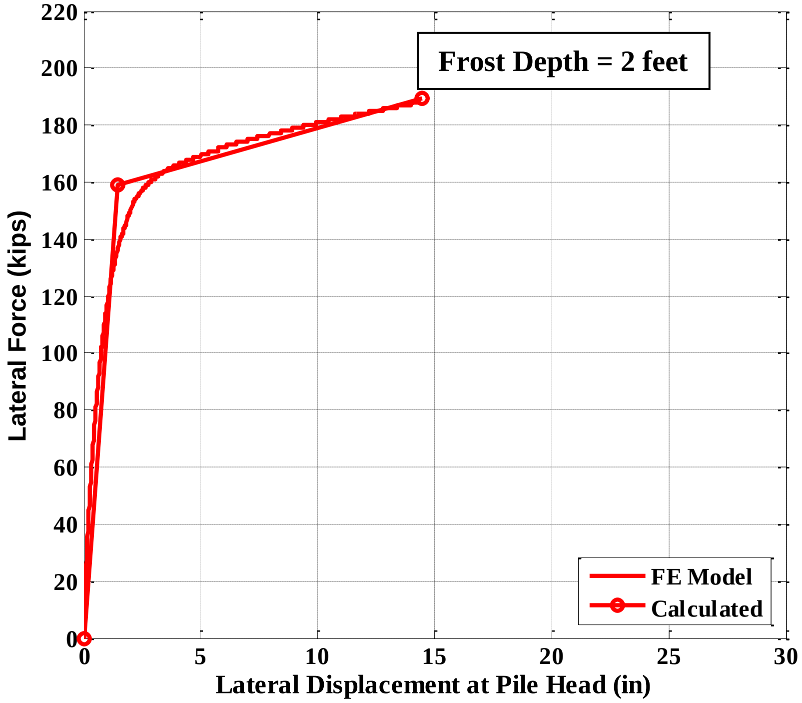

Figure 5.9: Load-displacement response when the frost depth is 2 feet.

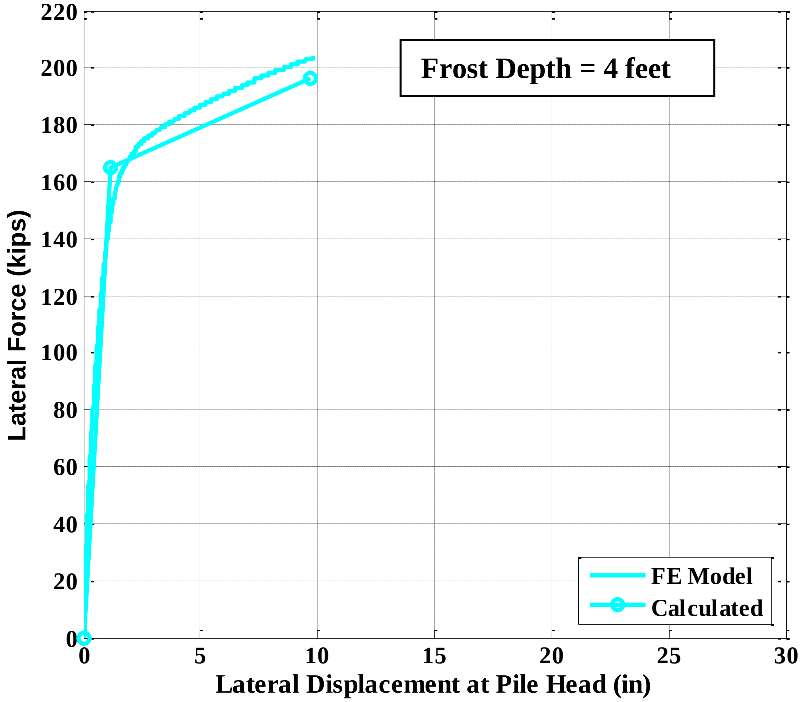

Figure 5.10: Load-displacement response when the frost depth is 4 feet.

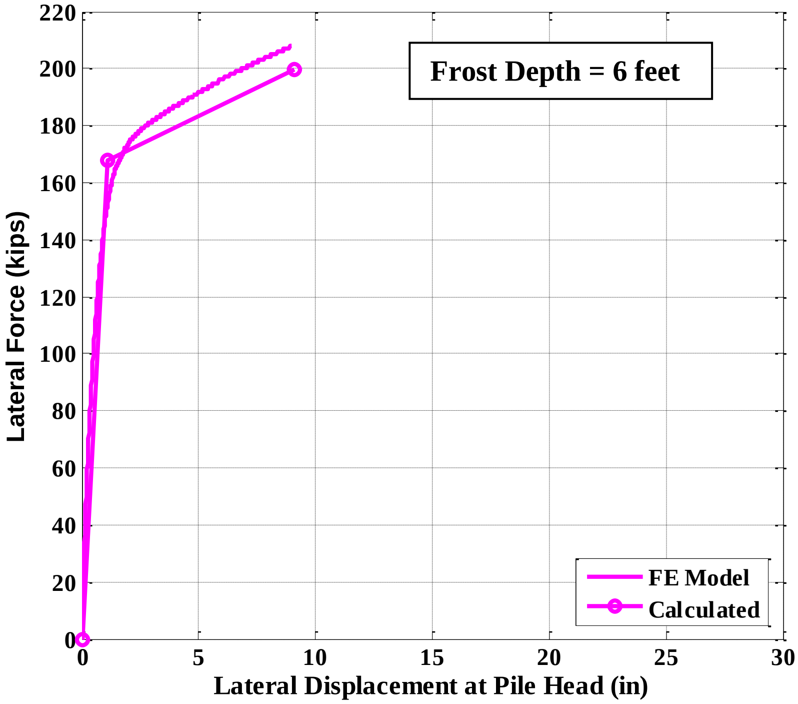

Figure 5.11: Load-displacement response when the frost depth is 6 feet.

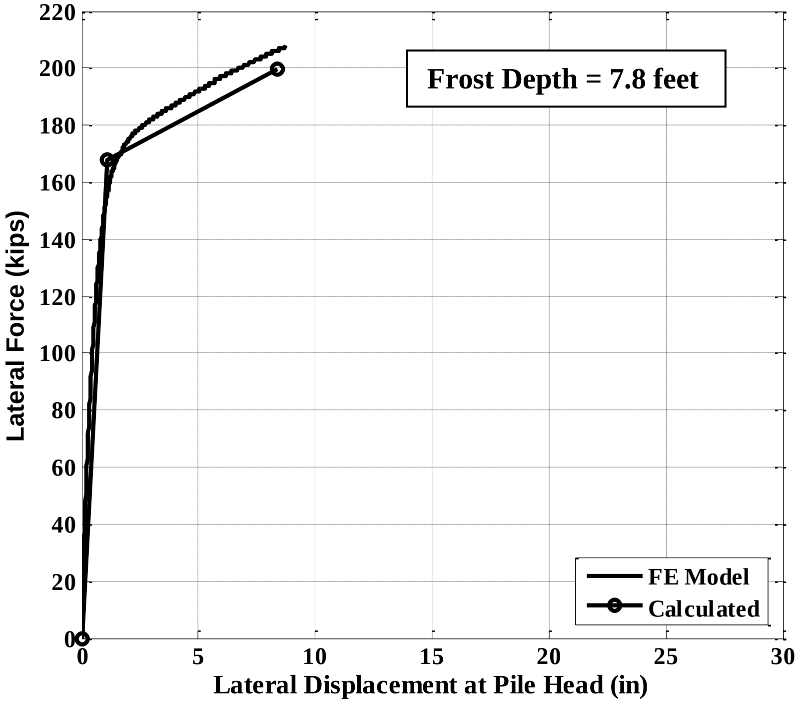

Figure 5.12: Load-displacement response when the frost depth is 7.8 feet.

Table 5.8: Comparison of Pile Behavior at Each Soil Condition

Frost Depth (ft)	L_M (×D*)	L_S (×D)	L_P (×D)
0 (unfrozen)	2.0	11.0	3.8
2	0.40	5.0	3.4
4	0.30	4.25	2.3
6	0.25	4.0	2.2
7.8	0.25	4.0	2.0

*Pile Diameter

5.5 Load-Displacement Response with Different Pile Heights Above Ground Surface

In order to investigate how pile height above ground surface affects depth of fixity, three more FE models were constructed to perform pushover analysis. The pile heights above ground were 4D, 6D, and 8D (D is the diameter of pile). In this study, the frost depth was assumed at 7.8 feet while keeping soil and pile properties consistent with the previous model with 7.8-foot frost. The bilinear model was employed later to study the effective depth of fixity of a pile in frozen soil.

The lateral load-displacement response is shown in Figure 5.13 through Figure 5.15. The strain limit of the extreme tensile rebar, that is, 5%, is used as the criteria to determine the ultimate deflection in an FE analysis. It shows that the ultimate load capacity of the soil–pile system increases from 68.7 to 137 kips, or a 100% increase, when a pile height above ground increases from 64 inches (4D) to 128 inches (8D). However, the displacement capacity of the soil–pile system also drops from 17.5 to 10.9 inches, or a 38% decrease.

The bilinear load-deflection response is also shown in Figure 5.13 through Figure 5.15. The values of L_M, L_S, and L_P for all cases are listed in Table 5.9. In this analysis, we limited L_P to 2.0D according to Chai (2002) and adjusted L_M and L_S to fit the load-deflection curve. The trend of the bilinear models agrees fairly well with the load-deflection response from FE modeling, except that the bilinear models have a larger ultimate deflection than the FE modeling results. This difference is likely because we assumed that the soil–pile system would fail at 5% rebar strain. This failure criterion needs further investigation.

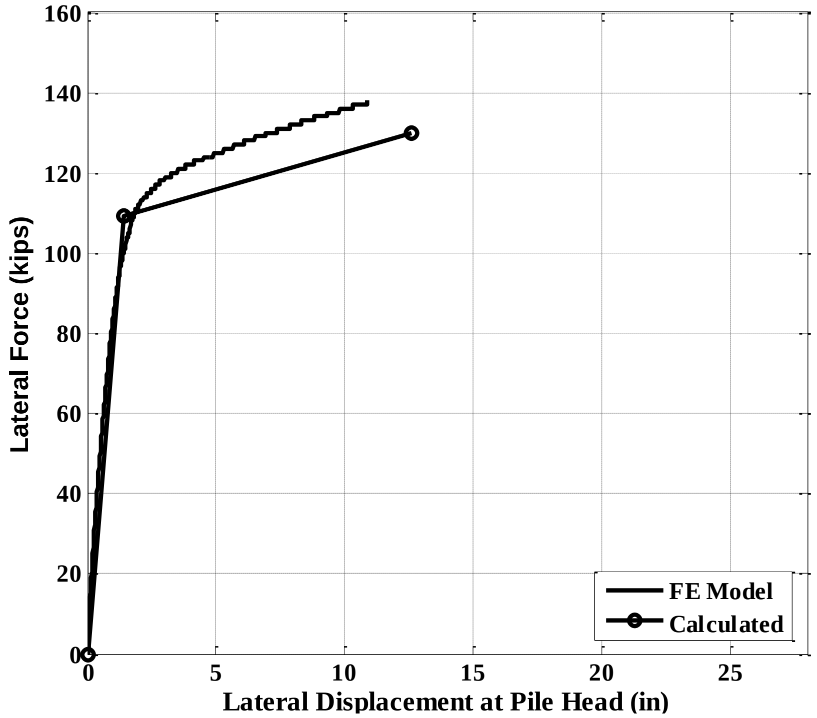

Figure 5.13: Load-displacement response when pile height above ground surface is 4D.

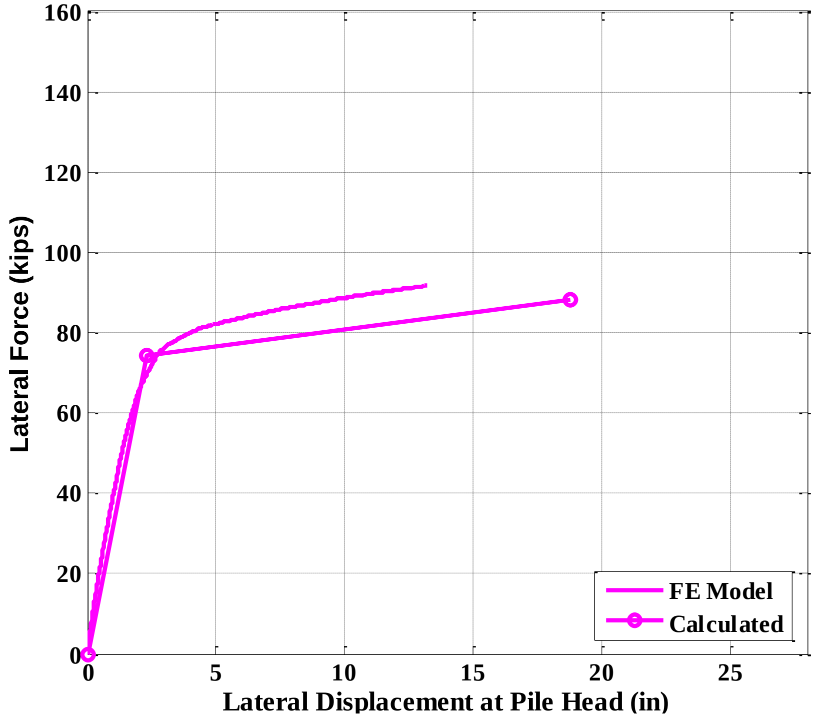

Figure 5.14: Load-displacement response when pile height above ground surface is 6D.

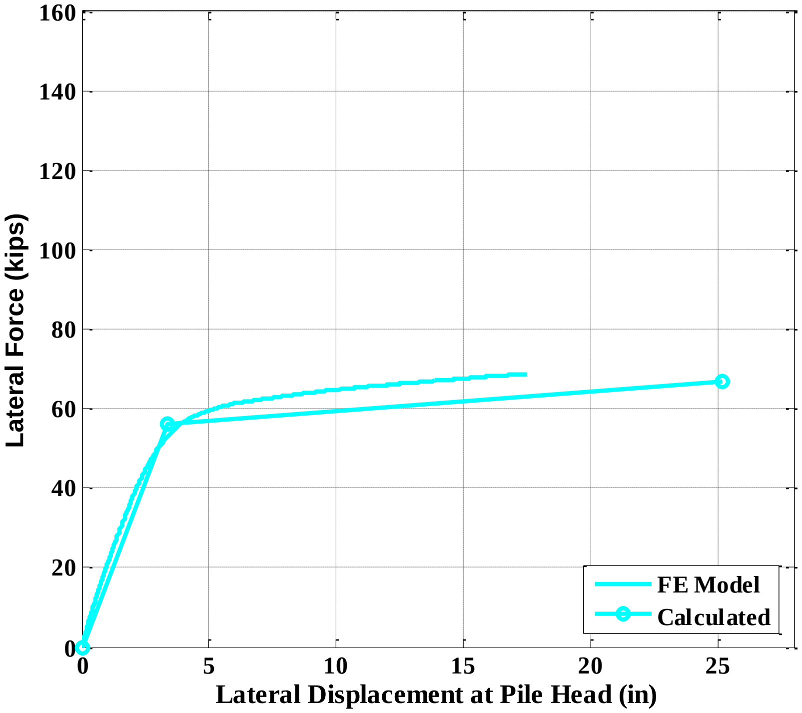

Figure 5.15: Load-displacement response when pile height above ground surface is 8D.

Table 5.9: Comparison of Pile Behavior at Different Pile Heights Above Ground Surface (H).

Pile heights above ground surface (×D*)	L_M (×D)	L_S (×D)	L_P (×D)
2.5 (40.25 inches)	0.25	4.0	2.0
4 (64 inches)	0.25	3.5	2.0
6 (96 inches)	0.25	3.5	2.0
8 (128 inches)	0.25	3.5	2.0

*Pile Diameter

CHAPTER 6. SIMPLIFIED DESIGN TOOL: *P-Y* APPROACH

6.1 Introduction

In this chapter, experimental *p*-*y* values were back-calculated by using the measured lateral response data from the quasi-static lateral load cyclic test that was conducted in March 2010, when the frost depth was 7.8 feet. A general procedure was recommended for constructing a *p*-*y* curve for frozen silt, primarily based on the weak rock model proposed by Reese (1997).

6.2 Back-calculation of *p-y* Values from Experimental Data

In order to evaluate the *p*-*y* values through the test results, soil reaction (p) and the pile deflection (y) need to be evaluated. The soil lateral reaction (p) can be calculated from the recorded bending moment $M(z)$ on a pile when the stiffness of the pile section (EI) is constant, using the following equation:

$$\mathrm{p(z)} = \frac{\mathrm{d}^2}{\mathrm{dx}^2}\mathrm{M(z)} \tag{6.1}$$

where z denotes depth. Bending moment was evaluated from the direct measurement of strain of rebar and the relationship between bending moment and strain of rebar from moment-curvature analysis (Figure 5.2). As shown in Figure 6.1, the maximum bending moment recorded from the test does not exceed the yield bending moment from moment curvature analysis when the lateral load is from 5 kips to 187 kips. However, when the lateral load is 200 kips, the pile is yielded and the bias of calculation of soil reaction may exist.

Since inclinometer data for the pile test were not accurate enough for evaluating pile deflection, the pile deflection recorded by six linear motion transducers above the ground surface and pile deflection predicted by using a FE model were combined to estimate pile deflection (y) at various depths below the ground surface.

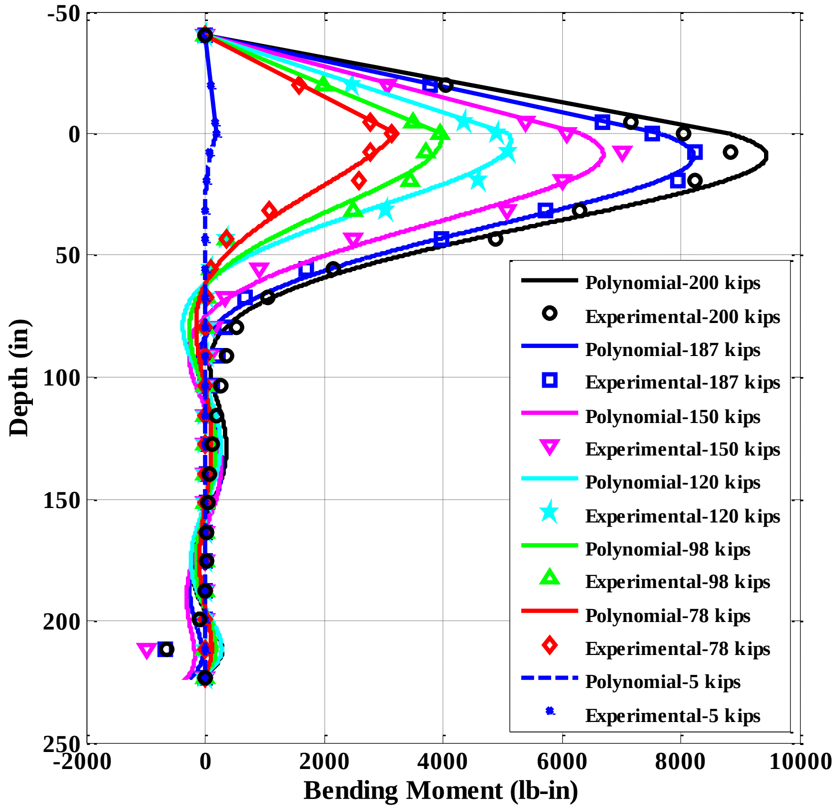

Figure 6.1: Polynomial interpolation of the experimental bending moment data.

6.2.1 Lateral resistance

Due to a limited number of bending moment measurements, a polynomial function was used to fit the discrete moment profile data. The polynomial fitting function has the advantage of resulting in a continuous function for lateral resistance (Wilson 1998). With the assumption that zero lateral resistance exists at the surface, a polynomial containing non-integer fitting terms was proposed by Wilson (1998). In order to have the best fit, a seventh-order polynomial, as shown in Equation (6.2), was employed in this study. The polynomial was fit to the data using a least-squared approach, and Equation (6.3) can be obtained by double differentiation of Equation (6.2) based on Equation (6.1).

$$M(z) = a+bz+cz^{2.5}+dz^{3}+ez^{4}+fz^{5}+gz^{6} \qquad (6.2)$$

$$p(z)=2.5\times1.5cz^{0.5}+3\times2dz^{1}+4\times3ez^{2}+5\times4fz^{3}+6\times5gz^{4} \qquad (6.3)$$

As shown in Figure 6.1, the polynomial interpolation matches well with the experiment data in different lateral load conditions (from 5 kips to 200 kips). Lateral resistance (*p*) was evaluated by using Equation (6.3). Lateral resistance profiles at various lateral loads are illustrated in Figure 6.2.

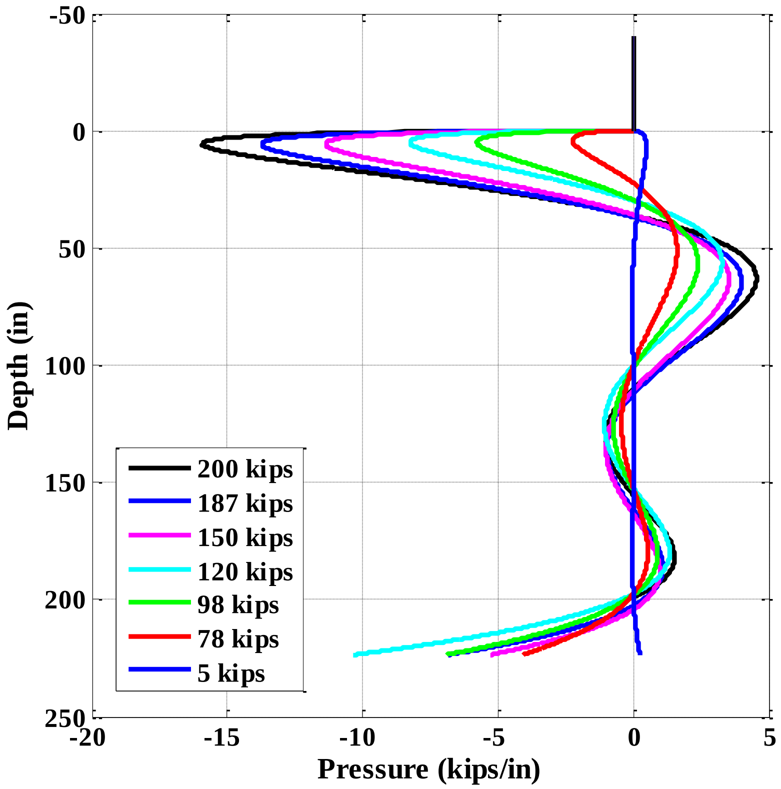

Figure 6.2: Lateral resistance back-calculated from the experimental bending-moment data.

6.2.2 Pile deflection

A FE model of the test pile was constructed to help find the pile deflection by employing OpenSeesPL. The pile dimensions and soil profile in the FE model were based on the test pile configuration and the site exploration report. The seasonally frozen soil properties were based on Haynes and Karalius (1977) and adjusted to match the load-deformation data obtained from the experiment, as shown in Figure 6.3.

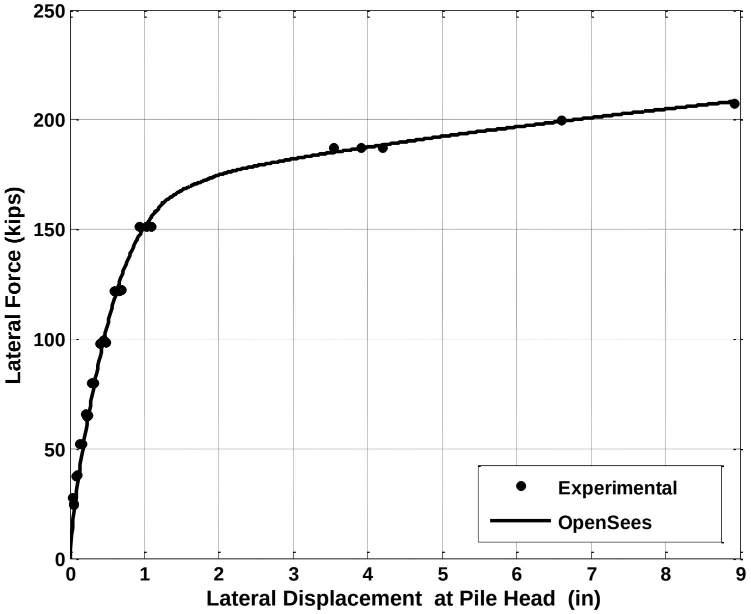

Figure 6.3: Comparison of pile deflection and lateral load behavior from the FE analysis and experiment.

The pile deflection predicted by the FE analysis at different lateral loads is shown in Figure 6.4. For comparison, the pile deflection measured above the ground surface by linear motion transducers is shown in the same graph. Figure 6.4 demonstrates that pile deflection above the ground surface agrees well with the test data. The predicted pile deflection was used to evaluate the *p*-*y* values of frozen silts at various depths. Since pile deflection (*y*) decreases quickly with increasing depth, it is only possible to evaluate *p*-*y* values for the top 20 inches of soil from this test. The *p*-*y* values derived from experimental data are plotted in Figure 6.5. Figure 6.5 shows that the back-calculated *p*-*y* values are not very sensitive to the frozen soil depth.

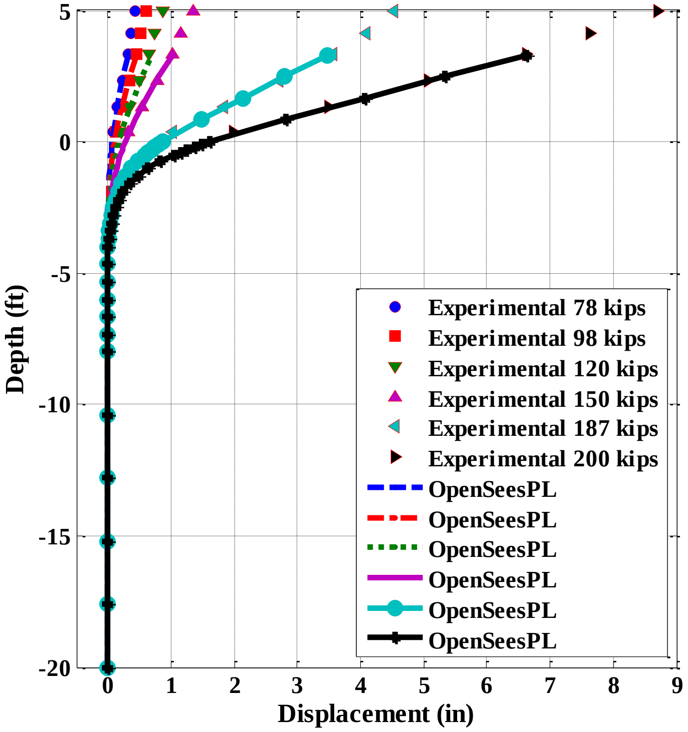

Figure 6.4: Comparison of predicted pile deflection with measurement data.

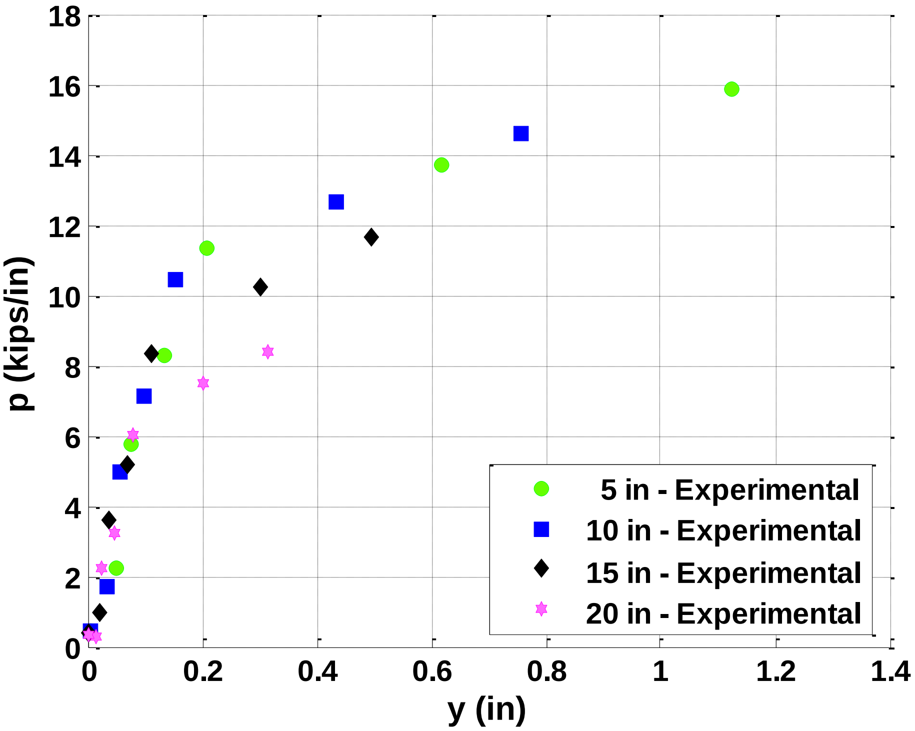

Figure 6.5: *P*-*y* values obtained from experimental data.

6.3 Recommended *p-y* Curve for Frozen Silt

When soil is frozen, the stiffness can change by as much as two orders of magnitude (Stevens 1973). When there is sufficient ice in the voids, cohesion is present in the frozen soil (Arenson and Springman 2005), meaning that the properties of frozen soils are similar to weak rock and clay. Thus, we used the *p-y* models for weak rock (Reese 1997) and clay (Matlock 1970) and modified them to construct a *p-y* curve for frozen soil. Appropriate parameters can be obtained by fitting the *p-y* curve with back-calculated *p-y* values.

As shown in Figure 6.6, the proposed *p-y* curve model of frozen silt has two sections: a cubic section (Equation [6.4]) and a constant section (Equation [6.5]).

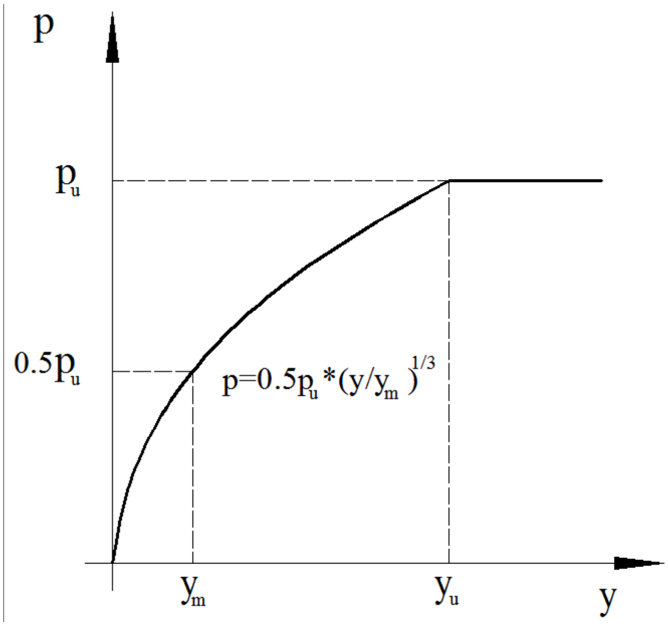

Figure 6.6: Sketch of the recommended *p-y* curve for frozen silt.

$$p = \frac{p_u}{2}\left(\frac{y}{y_m}\right)^{1/3} \qquad \text{for } y \leq y_u \qquad (6.4)$$

$$p = P_u \qquad \text{for } y > y_u \qquad (6.5)$$

where p_u is the ultimate resistance of frozen silt and can be derived through Equations (6.6) and (6.7); and y_m is pile deflection, where the corresponding resistance is half of the ultimate resistance of frozen silt. The formula for evaluating p_u is

$$p_u = 1.5q_u b \tag{6.6}$$

where q_u is the compressive strength of the frozen silt, and b is the diameter or width of the pile.

y_m is related to pile diameter and can be evaluated by using the following equation:

$$y_m = k_m b \tag{6.7}$$

where k_m is a constant and equal to the strain at which 50% of the ultimate strength is developed.

6.4 Comparison of Proposed *p-y* Curve with the Experimental Data

6.4.1 Comparison of the proposed *p-y* curve with back-calculated *p-y* values

No direct measurement of the compressive strength data was available from this project. However, several experimental programs have been carried out on the compressive strength of Fairbanks frozen silt (Zhu and Carbee 1984; Haynes and Karalius 1977). The results obtained by Haynes and Karalius (1977) were used in this study. For a loading rate of 1 inch/minute, the compressive strength of Fairbanks frozen silt q_u (ksi) can be related to soil temperature T (°C) by Equation (6.8). This equation is applicable for soil temperature in the range of 0°C (32°F) to -18°C (-0.4°F).

$$q_u = 0.145\ (2.15\text{-}0.33T\text{+}0.01T^2) \tag{6.8}$$

where T is the frost temperature.

Figure 6.7 shows the ground temperature profile obtained from the pile test site. The soil temperature profile is almost linear and can be expressed by Equation (6.9).

$$T = T_{sur} - \frac{T_{sur}}{Z_f} \tag{6.9}$$

where T_{sur}, the ground surface temperature, is -8°C (17.5°F), and Z_f, the frost depth, is equal to or less than 7.8 feet for this pile test.

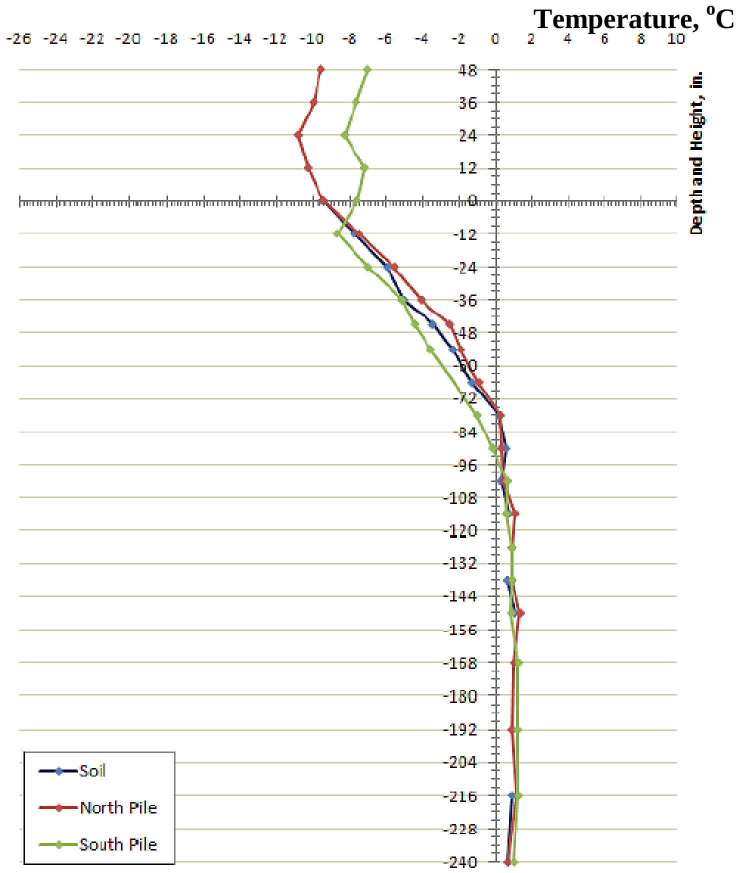

Figure 6.7: Temperatures profiles measured at the pile test site on March 24, 2010 (Davis 2010).

The water content of frozen silt at the test site was around 35%; the soil can be defined as ice-poor soil according to Weaver and Morgenster (1981). k_m was estimated to be 0.01 based on Haynes and Karalius (1977) and Crowther (1990).

As depicted in Figure 6.8, *p-y* curves were evaluated for the Fairbanks pile test at different depths, based on the proposed *p-y* curve. Note that the proposed *p-y* curves match well with the back-calculated *p-y* values. Additional *p-y* curves were produced by using the proposed curve for various depths, as illustrated in Figure 6.9. This figure shows that soil resistance decreases with depth. This is primarily caused by the compressive strength of frozen silts, which decreases almost linearly with depth due to the rising soil temperature. Overburden effects are not prominent. For comparison purposes, a *p-y* curve for unfrozen silt at 10-inch depth (Reese et al. 1974) is plotted in Figure 6.9 (b). By comparing Figure 6.9 (a) with Figure 6.9 (b), one sees that the lateral resistance of frozen silt is much greater than that of unfrozen soil.

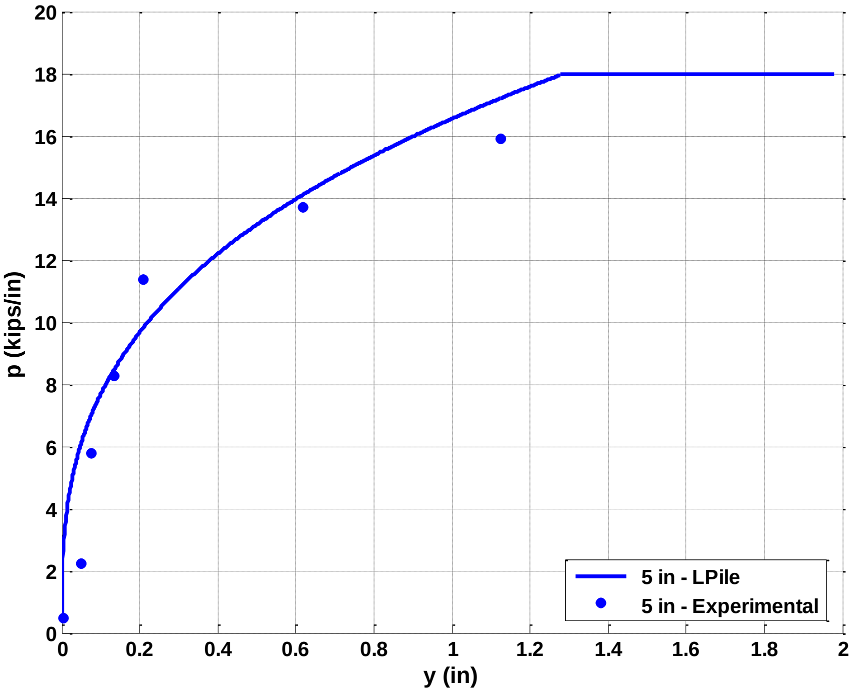
20
18
16
14
12
10
8
6
4
2
0
p (kips/in)
0
0.2
0.4
0.6
0.8
1
1.2
1.4
1.6
1.8
2
y (in)
5 in - LPile
5 in - Experimental

(a)

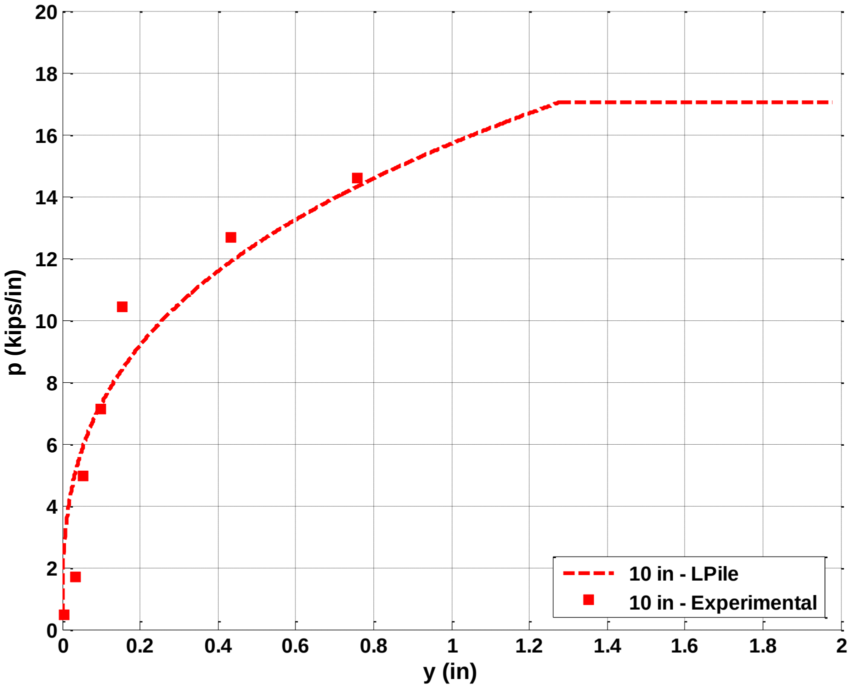
20
18
16
14
12
10
8
6
4
2
0
p (kips/in)
0
0.2
0.4
0.6
0.8
1
1.2
1.4
1.6
1.8
2
y (in)
10 in - LPile
10 in - Experimental

(b)

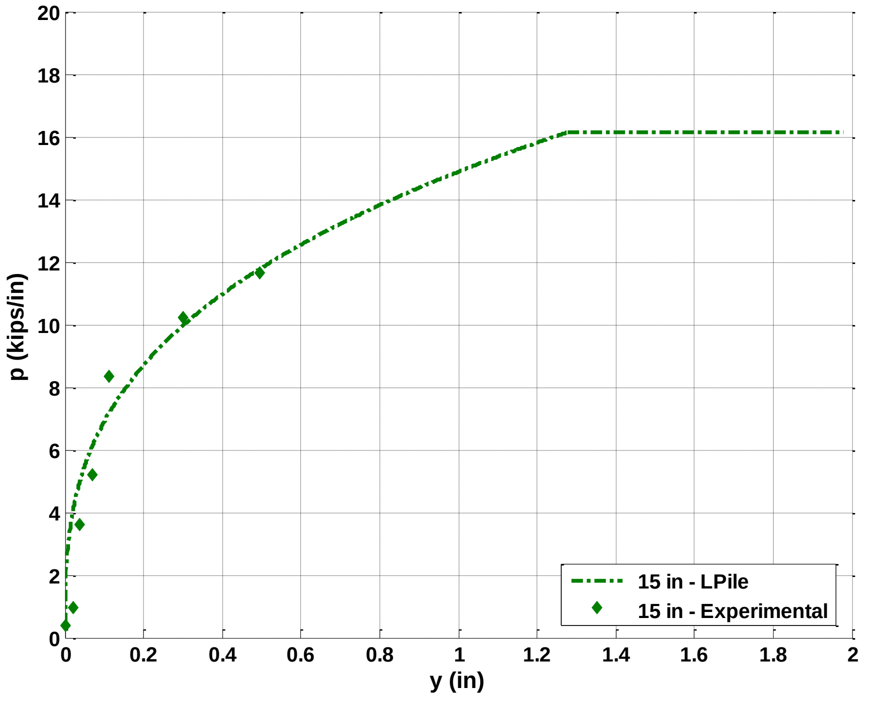

(c)

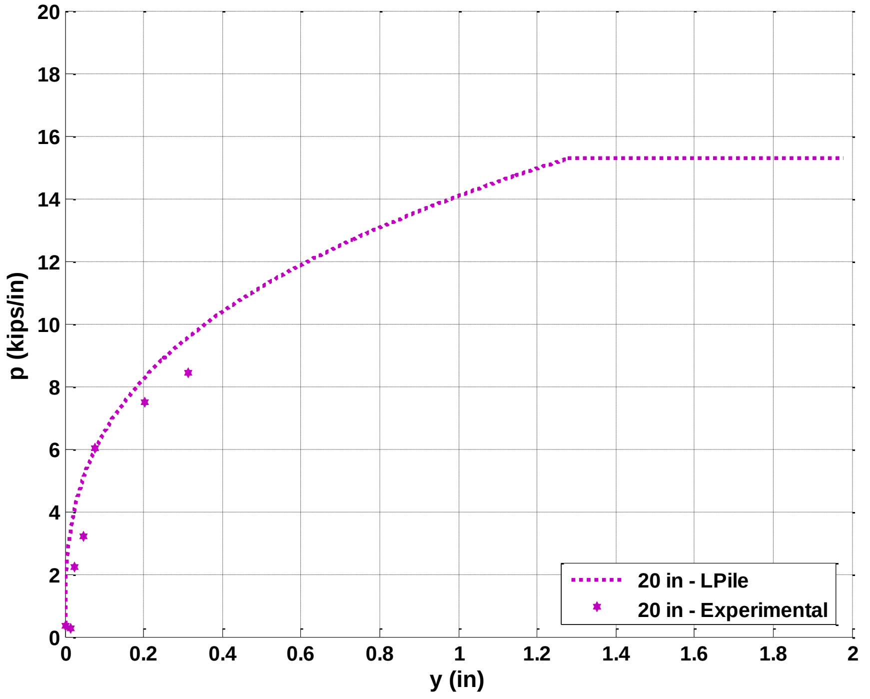

(d)

Figure 6.8: Proposed *p*-*y* curves vs. back-calculated *p*-*y* values at depths of (a) 5 inches, (b) 10 inches, (c) 15 inches, and (d) 20 inches.

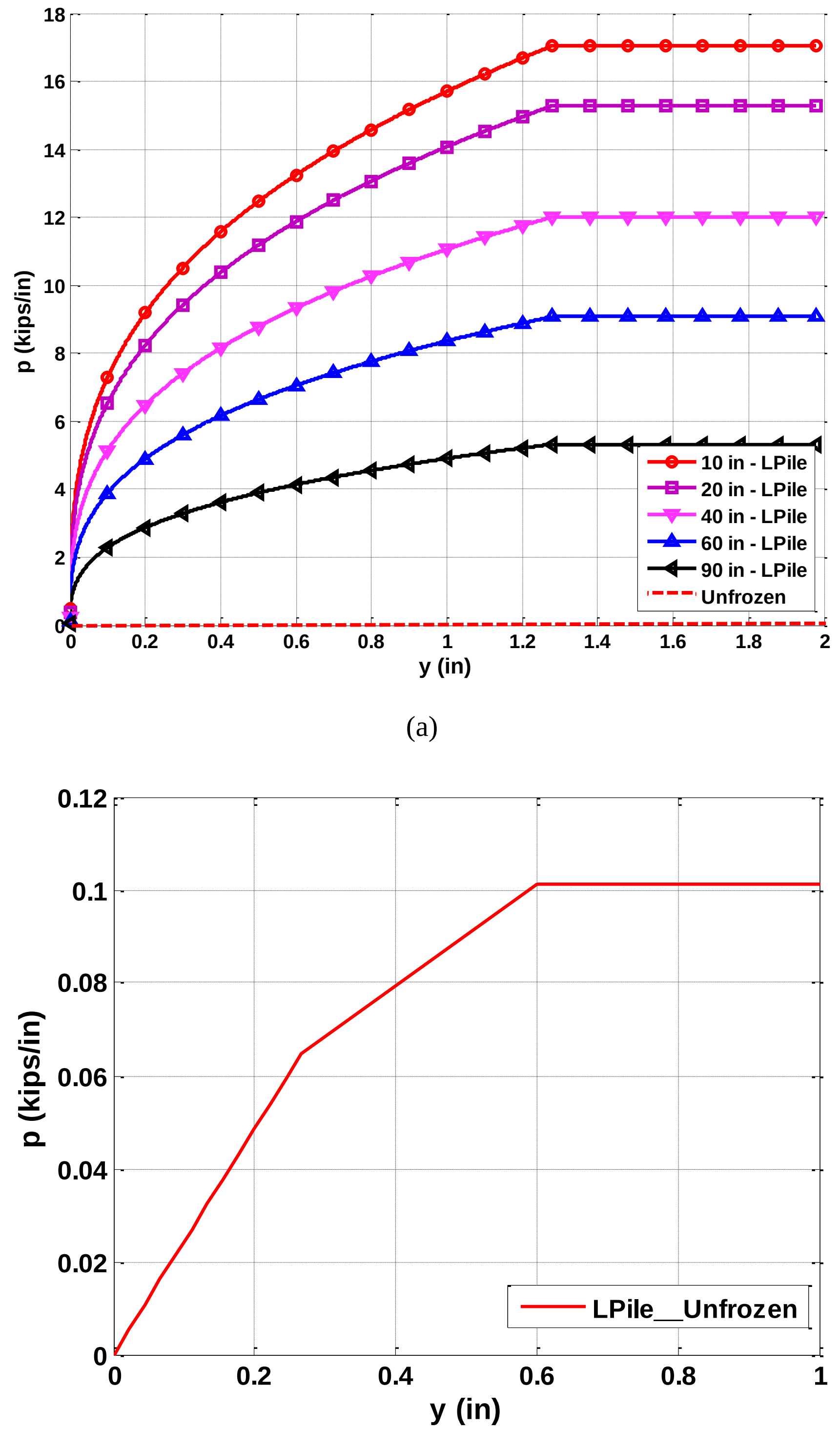

(a)

(b)

Figure 6.9: (a) Proposed *p*-*y* curves for frozen silt at various depths for the test site; (b) close-in of the *p*-*y* curve for unfrozen silt.

6.4.2 Comparison of pile response between the pile test and LPile modeling

LPile is a special-purpose program for the analysis of laterally loaded piles using the *p-y* curve approach (http://www.ensoftinc.com); the program is widely used by practicing engineers. The proposed *p-y* curve was inputted into LPile in order to predict the behavior of the pile, and results were compared with the test results.

In the LPile model, the section type Round Concrete Shaft with Permanent Casing, as shown in Figure 6.10, was used to simulate the reinforced concrete-filled steel-pipe pile that was used in the field test. The pile was divided into 277 one-inch-long segments with soil springs (*p-y* curves) located at each node. The spring stiffness for unfrozen silt was defined by the sand (Reese et al. 1974) *p-y* model in LPile. No built-in soil model was available for frozen silt or other types of frozen soil in LPile, so the proposed *p-y* curve for frozen silts was used in this analysis. In the pushover analysis, lateral displacement was applied at the loading point (referred to as the pile head), which is 40.25 inches above the ground surface.

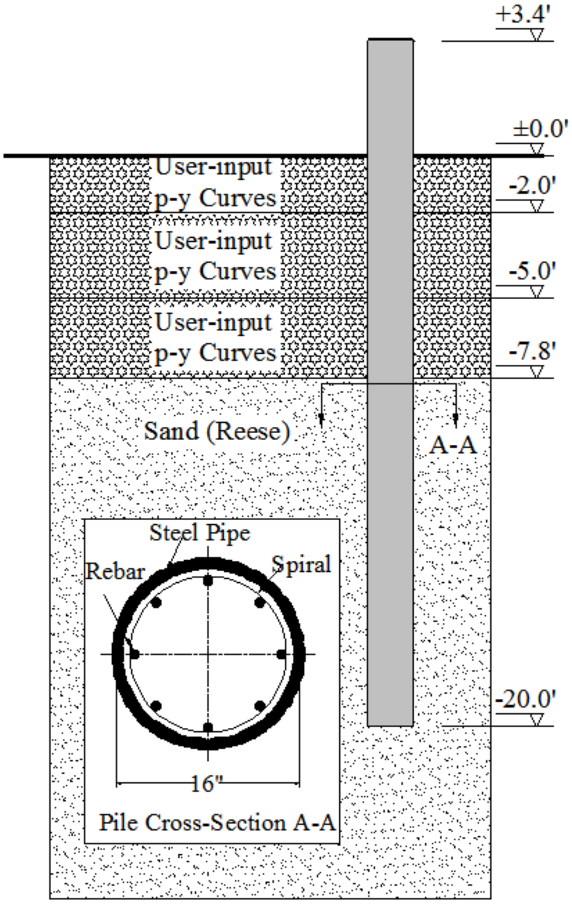

Figure 6.10: LPile model of the test pile.

Figure 6.11 shows lateral load versus deflection at the loading point from LPile modeling and from the experiment. Note that the load-deflection behavior from the LPile model agrees fairly well with the test results up to the pile yielding. After the pile yielding, the LPile model result deviates from the test results, which is likely due to the simplified steel and concrete models used in LPile that are not capable of capturing the strain-hardening behavior of the pile. The bending-moment profile and lateral-resistance profile at an 8.9-inch pile head deflection are shown in Figure 6.12 and Figure 6.13, respectively. The results from the pile test were plotted for comparison. The results from LPile agree well with the results from the pile test. The comparisons presented in this section indicate that the proposed *p*-*y* curve for frozen silt is capable of modeling frozen soil lateral resistance during lateral loading.

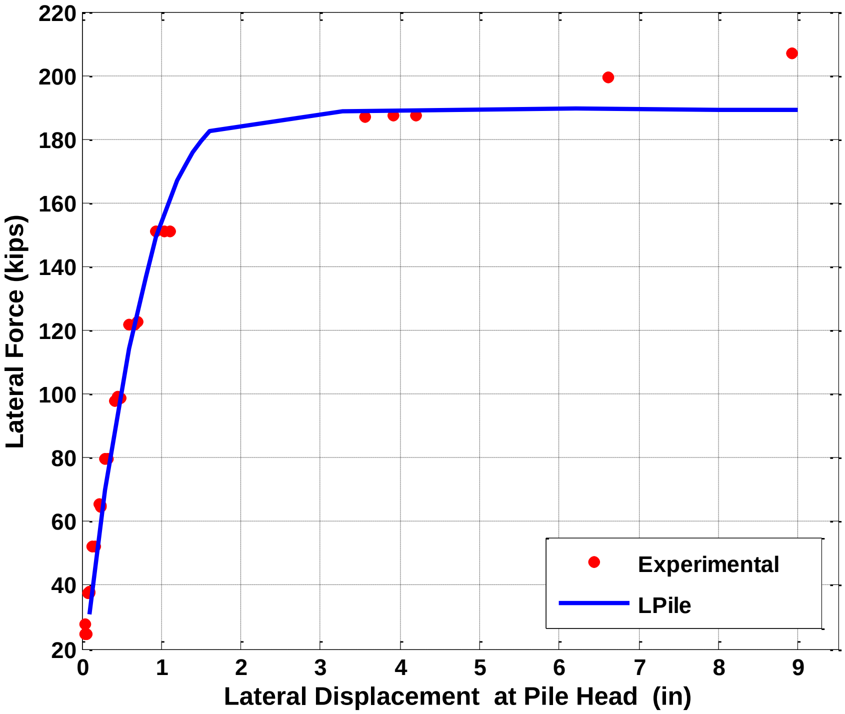

Figure 6.11: Lateral force vs. lateral displacement at the loading point.

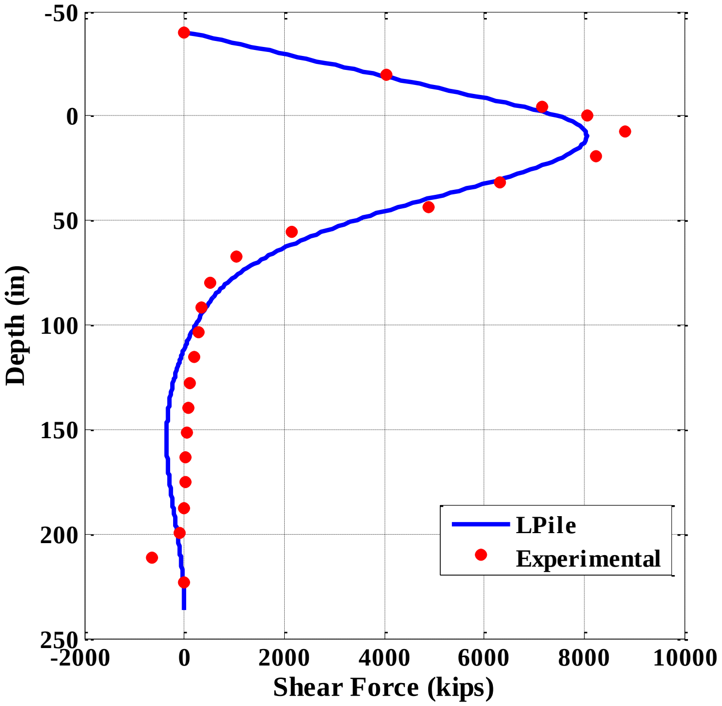

Figure 6.12: Bending-moment profile at an 8.9-inch pile head deflection.

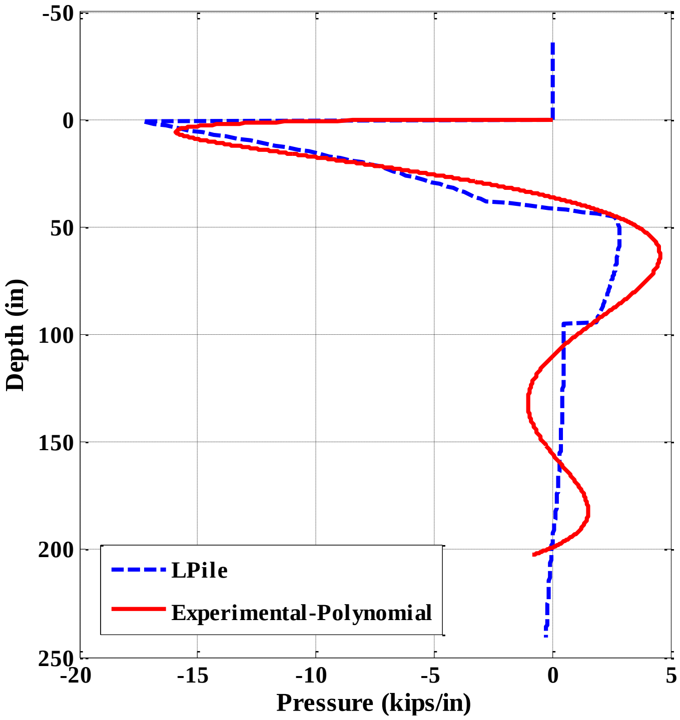

Figure 6.13: Pressure profile at an 8.9-inch pile head deflection.

6.5 Validation of Proposed *p-y* Curve with Additional Field Test Data

6.5.1 Field test in Northwest Territory, Canada

Results from another field test were used to validate the proposed *p-y* curve. A series of lateral load pile tests were conducted north of Inuvik, Northwest Territory, Canada (Rowley et al. 1973). The test piles were embedded in ice-rich silts. Lateral loads were exerted on two timber piles and three steel piles. The temperature profile of the site was uniform, and the average ground temperature for the depth of pile embedment was -1.5°C (29°F). The compressive strength of the frozen silt estimated by Equation (4.9) (Haynes and Karalius 1977) was 413 psi, which is within the range of 317 psi to 418 psi, the compressive strength range reported by laboratory tests on samples collected from the pile test site (Watson et al. 1973). For this ice-rich soil, k_m was estimated to be 0.005, based on Crowther (1990).

A steel-pipe pile (S-4-L) filled with sand was selected for analysis in this study. Basic data for pile S-4-L were as follows: diameter b = 12 inches; wall thickness t = 0.374 inches; embedded length L = 103 inches; and length above ground surface e = 21 inches.

In the LPile model, the section type Round Concrete Shaft with Permanent Casing was employed to simulate the steel-pipe pile used in the test. The compressive strength of the frozen sand inside the pile was assumed at 1.40 ksi, based on Baker (1979). The pile was divided into 103 one-inch-long segments with springs (*p-y* curves) located at each node. The spring values for frozen silt, as shown in Figure 6.14, were computed based on the proposed *p-y* curve. The temperature profile was assumed constant based on field data. Therefore, the soil resistance remains identical at different depths.

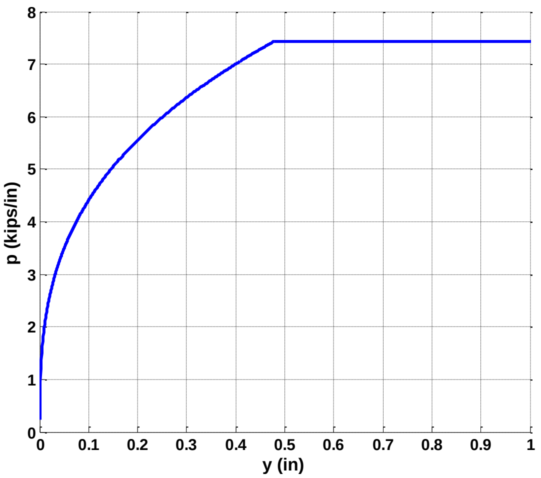

Figure 6.14: *P-y* curves for permafrost.

Figure 6.15 compares the lateral force versus lateral displacement at the loading point between LPile analysis and the pile test. The LPile analysis results closely follow the trend of the experimental data. Figure 6.15 reveals that the load-deflection curve predicted by LPile, using the proposed *p-y* curve, is stiffer than that of the experiment results for deflections larger than 0.15 inch. The reason for this difference is that in the experiment each load was applied on the pile for two to three hours and the experimental data include substantial creep effects. Figure 6.16 and Figure 6.17 show the distribution of shear force and bending moment with depth at a lateral load of 60 kips. Overall, the analysis confirms that the proposed *p-y* curve is capable of modeling frozen silts in the analysis of laterally loaded piles in permafrost.

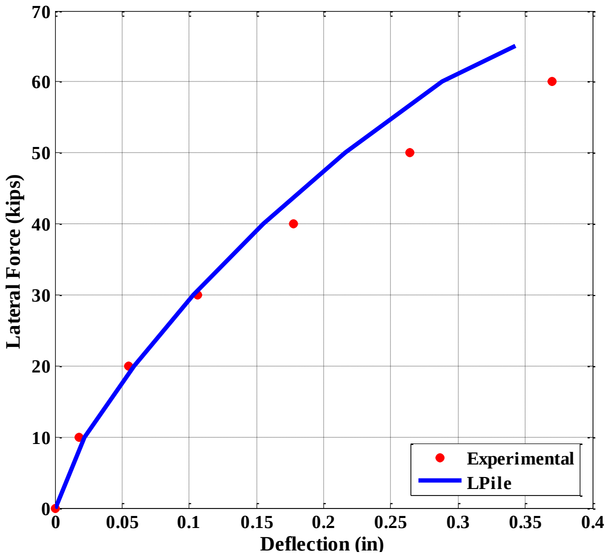

Figure 6.15: Lateral displacement vs. lateral displacement at the loading point.

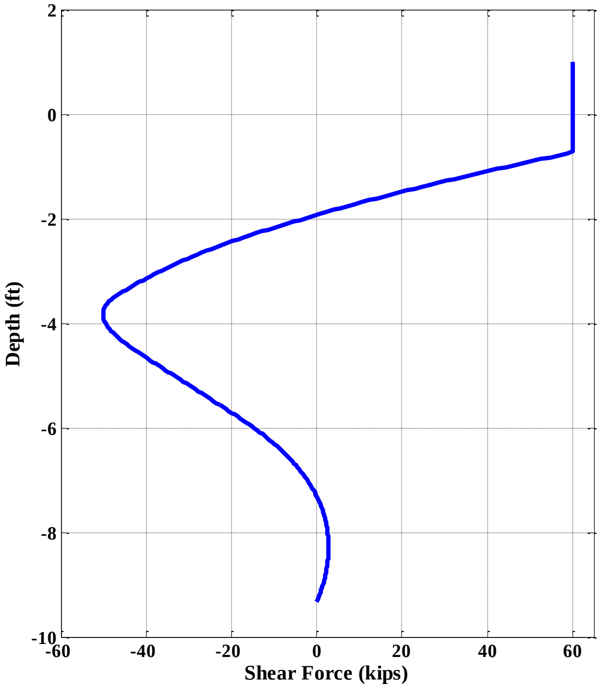

Figure 6.16: Shear force profile at a lateral load of 60 kips.

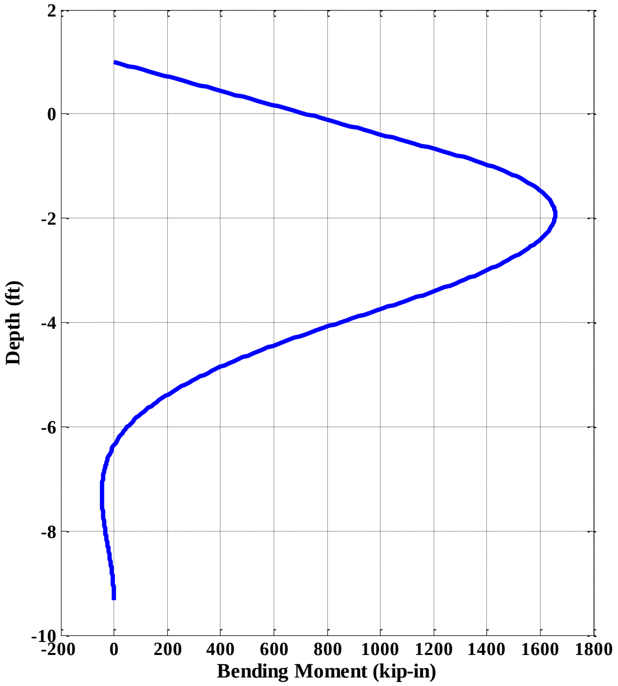

Figure 6.17: Bending-moment profile at a lateral load of 60 kips.

6.5.2 Field test in Northern Quebec, Canada

Another field test (Foriero et al. 2005) conducted in northern Quebec was used to validate the proposed *p-y* curve. A lateral load was applied to a steel pile with an external diameter of 2 inches (51 mm) at a constant rate of displacement of 0.39 inches/day (10 cm/day). The total duration of the test was about 26 hours, and the total displacement was 4.26 inches (10.83 cm). The flexural stiffness (EI) of the test pile is 1.57×10^4 kips•in^2 (45 kN•m^2), the embedded length is 159 inches (4.05 m), and the loading point is 25.6 inches (0.65 m) above the ground surface. From the temperature profile measured during the test, the 32°F (0°C) isotherm lies at a soil depth of 29.5 inches (0.75 m). The soil beneath that was considered warm permafrost with a temperature between 32°F (0°C) and 29.3°F (-1.5°C).

Since no detailed soil properties were presented in Foriero et al. (2005), the seismic cone penetration tests results (Leblanc et al. 2004) obtained in the same site was used to estimate the properties of the soil. With cone resistance (q_c), shear modulus (G) and undrained shear strength (s_u) can be estimated by iteration using the following equations from Kulhawy and Mayne (1990):

$$\mathrm{q_c = N_k s_u + \sigma_{vo}} \tag{6.10}$$

$$\mathrm{N_k = 2.57 + 1.33(\ln\ I_r + 1)} \tag{6.11}$$

$$\mathrm{I_r = G/s_u} \tag{6.12}$$

in which N_k is the cone bearing factor, σ_{vo} is the total overburden stress, and I_r is the rigidity index. The permafrost in the site can be considered ice-rich soil and modeled as cohesive. The unconfined compressive strength can be calculated from the following equation:

$$\mathrm{q_u = 2 \cdot s_u} \tag{6.13}$$

k_m was estimated to be 0.005 based on Crowther (1990). Table 6.1 summarizes the soil properties of the test site. *P-y* curves of the test site at different depths are shown in Figure 6.18, based on the proposed *p-y* curve model.

Table 6.1: Soil Properties of the Test Site.

Depth (in.)		Average Unit Weight (pcf)	s_u (psi)	q_u (psi)	k_m
0	Unfrozen	111	4.35	-	-
29.5		111	7.25	-	-
39.4	Frozen	127	116	232	0.005
157.5	Frozen	127	152	304	0.005

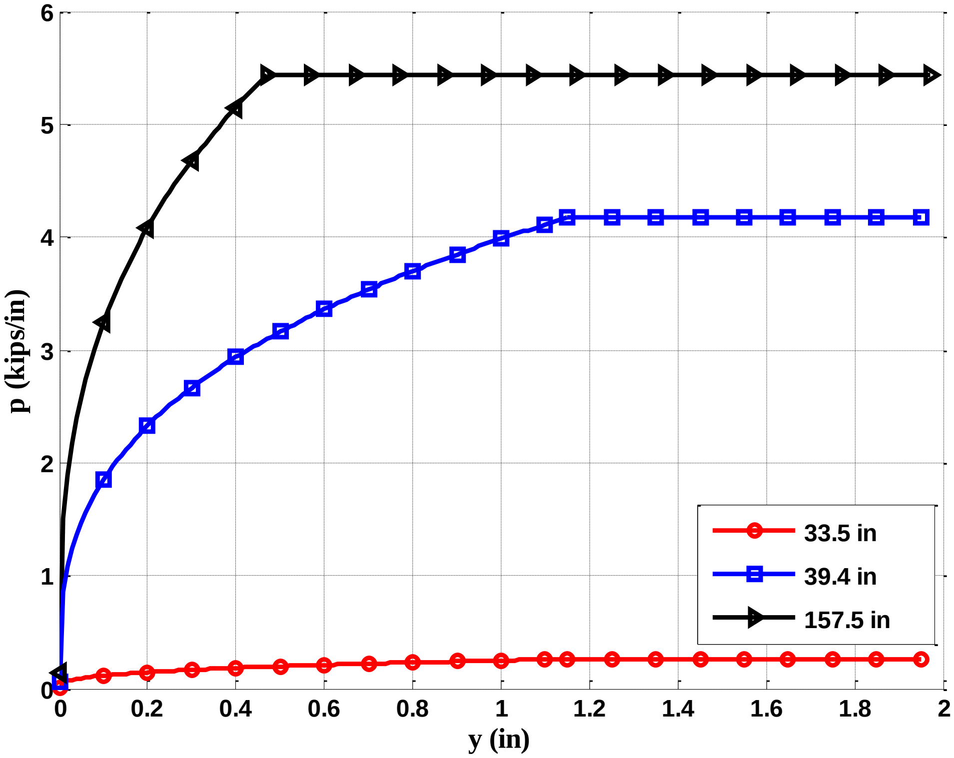

Figure 6.18: *P-y* curves for frozen soil at various depths at the test site.

A LPile model with the section type Steel Pipe Pile was constructed to simulate the field test. The pile was divided into 320 sections with springs (*p-y* curves) located at each node. The spring stiffness for unfrozen silt was defined by the silt (cemented c-phi) *p-y* model in LPile. The proposed *p-y* curve, as shown in Figure 6.18, was used for frozen silts in this site. Lateral displacements were applied on the pile to perform pushover analyses.

Figure 6.19 compares experimental and LPile results for bending moments in a 16-inch-diameter steel-jacketed concrete pile tested at the ASCE CRREL test site at Farmers Loop Road in Fairbanks, Alaska. Figure 6.20 compares load versus deflection for the same 16-inch-diameter steel-jacketed concrete pile for different applied loads. Experimental and LPile results for moment and deflection agree well. Because the lateral load tests were applied at a rate of displacement of 4 inches/day (10 cm/day) and creep displacements occurred during the test, results from the LPile analyses are slightly stiffer than the experimental data.

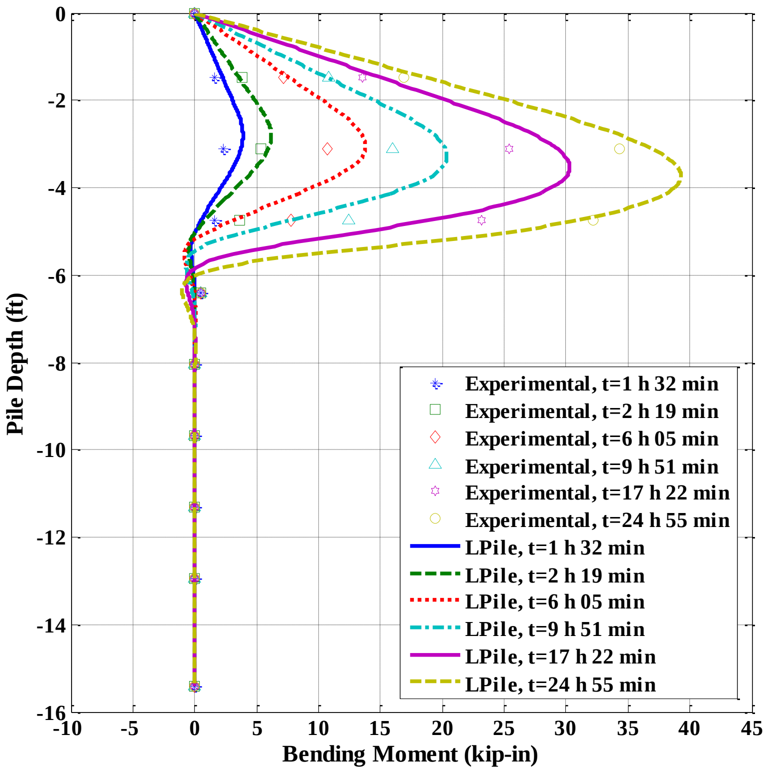

Figure 6.19: Bending moment profiles for a 16-inch-diameter steel-jacketed concrete pile.

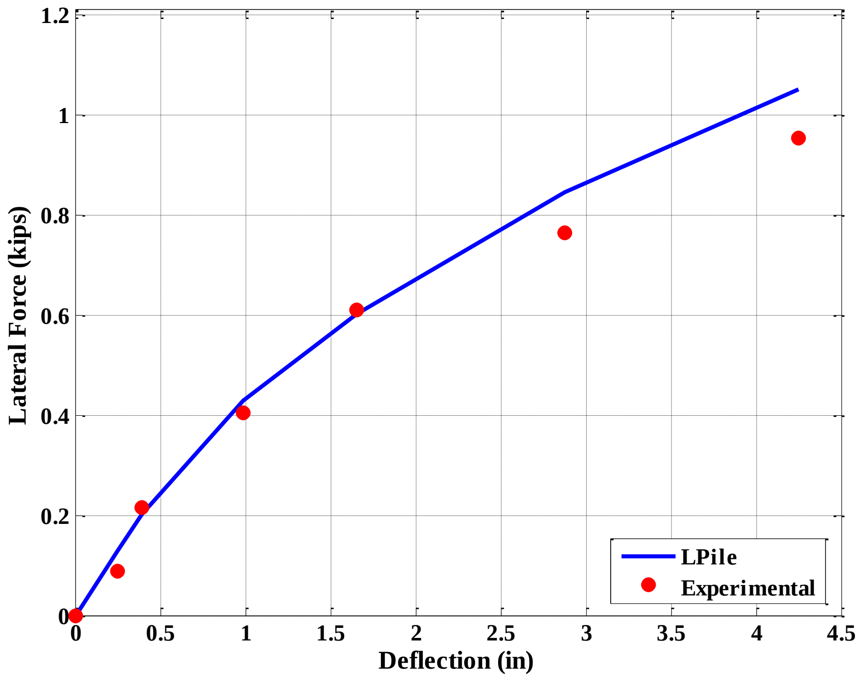

Figure 6.20: Lateral deflection at the point of load vs. applied lateral force.

CHAPTER 7. CONCLUSIONS AND SUGGESTED RESEARCH

7.1 Conclusions

Field experiments and FE analyses of seasonally frozen soil effects on the dynamic properties of a bridge and on the lateral behavior of a soil–pile system have been conducted in this project. A bridge in Anchorage, Alaska, was instrumented to monitor its dynamic/seismic performance for more than a year. Meanwhile, a FE model for the corresponding bridge was built by using the OpenSees simulation platform. After validating this FE model by the field-testing data, modal analysis was performed in different soil conditions to analyze the relationship between the dynamic properties and the frost thickness. Furthermore, large-formation quasi-static cyclic pile tests were conducted to collect data for validating design tools. The pile performance data collected from pile tests were used to evaluate design parameters based on the fixity depth approach, including depth-to-maximum moment, depth of fixity, and analytical plastic hinge length. In addition, a *p-y* curve for frozen silt was proposed based on the back-calculated *p-y* values for analysis of laterally loaded piles. The proposed *p-y* curve for frozen silt was validated by the data obtained from an independent field test conducted in Quebec, Canada.

The conclusions drawn from this research are summarized as follows:

1. The deepest frost penetration at the bridge site occurs around the end of March and reaches about 5 feet.

2. Frost penetration estimation, using the modified Berggren formula, agrees well with field observations. The modified Berggren formula with calibrated parameters can be used to predict frost depth for the bridge site when field measurement is not available.

3. Modal frequency increases with frost penetration. Specifically, when the site is unfrozen, the first transverse modal frequency is 2.5 Hz. As the frost thickness remains around 4 feet, the modal frequency oscillates around 7.5 Hz, representing a 200% increase. This indicates that the bridge is substantially stiffer when frozen than when unfrozen.

4. The three-dimensional FE model of the bridge captures the measured dynamic response of the bridge in terms of the first transverse modal frequency and shape in various thickness of

frozen ground. This model is suitable for predicting fundamental frequency in extreme conditions (e.g., the frost depth reaches 6 feet or more).

5. We found that, for this study, single-pile test data correlated well with a 7.8-foot frost depth for establishing design parameters, using the depth-of-fixity approach. As part of this comparison, depth-to-maximum moment, depth of fixity, and analytical plastic hinge length were evaluated.

6. Where piles are embedded in Alaska silts, we recommend when designing for frozen conditions that an 8-foot depth of frozen soil be used for the depth-of-fixity approach.

7. We found by back-calculation the *p*-*y* values of frozen silts based on the experimental data obtained from the Fairbanks lateral pile test program.

8. We propose a *p*-*y* curve based on back-calculated *p*-*y* values. Comparison of pile behavior predicted by using the proposed *p*-*y* curve agrees well with field test results obtained from Fairbanks and Canada, and can be used for the analysis of laterally loaded piles embedded in frozen silt in design practices.

7.2 Suggested Future Research

The main objectives set forth for this project have been accomplished. In the course of conducting this project, the following topics have been identified as worthy of future research:

1. Monitoring of the seismic behavior of the bridge should be continued for a few more years to cover more freeze/thaw cycles and to obtain the bridge behavior in larger-magnitude earthquakes.

2. In situ tests or high-quality sample laboratory tests should be conducted to obtain soil properties, including small strain shear modulus, shear strength, and strain value at which the shear strength is achieved for frozen soils including organic, cohesive, and cohesionless soils for use in constructing *p*-*y* curves of frozen soils.

3. The failure criterion used in this study—that the frozen soil–steel-pile pile system would fail at 5% rebar strain—needs further investigation.

4. Linear strain distribution was assumed across the reinforced concrete-filled steel-pipe pile section. Moment-curvature data obtained from the experimental data deviate from the predicted moment-curvature data after yielding, and this suggests that further study is needed in this aspect.

5. Other factors including the impact of aboveground pile height on the fixity-depth approach parameters need further investigation.

6. It would be desirable to have more pile test data available for validating and improving the *p*-*y* curve proposed in this study.

References

AASHTO (2010). Guide Specifications for LRFD Bridge Design. American Association of State Highway Transportation Officials, Customary U.S. Units, 1st edition, with 2010 Interim Revisions.

AEIC (Alaska Earthquake Information Center) (2010). General Information. <http://www.aeic.alaska.edu/html_docs/overview.html>

Alampalli, S. (1998). “Influence of in-service environment on modal parameters.” Proc., 16th Int. Modal Analysis Conf., Santa Barbara, California, 111–116.

Al-Hunaidi, M. O., Chen, P. A., Rainer, J. H., and Tremblay, M. (1996). “Shear moduli and damping in frozen and unfrozen clay by resonant column tests.” Canadian Geotechnical Journal, 33(3): 510–514.

Andersland, O. B., and Ladanyi, B. (2004). *Frozen Ground Engineering*, 1st ed. Hoboken, NJ: John Wiley & Sons, Inc.

Arenson L.U., and Springman S.M. (2005). “Mathematical description for the behaviour of ice-rich frozen soils at temperatures close to zero centigrade.” Canadian Geotechnical Journal 42: 431–442.

ASTM (2007). American Society for Testing and Materials, Standard Test Methods for Deep Foundations Under Lateral Load. ASTM International, September 1, 2007, 18 pp.

Bai, F. (2007). “Effects of seasonally frozen ground on dynamic properties of UAA parking garage structure-soil system.” Civil Engineering Graduate Project, University of Alaska Anchorage, Anchorage, Alaska.

Baker, T.H.W. (1979). “Strain rate effect on the compressive strength of frozen sand.” Engineering Geology, 13: 223–231.

BeadedStream LLC (2008). <http://www.beadedstream.com/index.html>

Binonwangan, R. C. (2009). “Seasonal freezing effects on the dynamic response of bridge structures on pile foundation.” Civil Engineering Graduate Project, University of Alaska Anchorage, Anchorage, Alaska.

Brownjohn, J.M.W., Moyo, P., Omenzetter, P., and Lu, Y. (2003). “Assessment of highway bridge upgrading by dynamic testing and finite-element model updating.” Journal of Bridge Engineering, 8: 162–72.

Caltrans (1986). Bridge Design Specifications Manual. Calif. Dept. of Transportation, Sacramento, California.

Campbell Scientific (2010). CR90000x Modular Measurement and Control System. http://www.campbellsci.com/cr9000x (Jan. 2010).

Chai, Y. H. (2002). "Flexural strength and ductility of extended pile-shafts. I: Analytical model." Journal of Structural Engineering, 128(5): 589–594.

Coduto, D. P. (2001). *Foundation Design Principles and Practices*, 2nd ed. Upper Saddle River, NJ: Prentice-Hall, Inc.

Collins, M. P., and Mitchell, D. (1991). *Prestressed Concrete Structures*. Material properties. Englewood Cliffs, NJ: Prentice-Hall, pp. 61-65.

Cox, C. R., Reese, L. C., and Grubbs, B. R. (1974). "Field testing of laterally loaded piles in sand." Proceedings of 6th Annual Offshore Technology Conference, Houston, Texas.

Crowther, S. G. (1990). "Analysis of laterally loaded piles embedded in layered frozen soil." J. Geotech. Engrg., 1167: 1137–1152.

Czajkowski, R. L., and Vinson, T.S. (1980). "Dynamic properties of frozen silt under cyclic loading." J. Geotechnical Engineering Division, 106:GT9, 963–980.

Davis, D. (2010). "Effect of frost depth on the effective length of bridge piles." M.S. thesis, University of Alaska Fairbanks, Fairbanks, Alaska.

DOWL Engineers (2005). "Final geotechnical report Abbott loop extension, Abbott road to Tudor Road." ADOT&PF Project No. 56559.

Dowrick, D. J. (1987). *Earthquake Resistant Design*, 2nd ed. New York: Wiley-Interscience.

Dutta, U., Yang, Z., Xu, G., and Hazirbaba, K. (2008). "Effect of seasonally frozen soil and permafrost on seismic site response." Proceedings of 14th World Conference on Earthquake Engineering, Beijing, China, (Oct 12–17, 2008). CD ROM, Paper #S09-09.

Elgamal, A., Yang, Z., Parra, E., and Ragheb, A. (2003). "Modeling of cyclic mobility in saturated cohesionless soils." International Journal of Plasticity, 19(6): 883–905.

Elgamal, A., Lu, J., and Yan, L. (2008). "Large-scale computational simulation in geotechnical earthquake engineering." The 12th International Conference of International Association for Computer Methods and Advances in Geomechanics (IACMAG), Goa, India.

Elwi, A. A., and Murray, D. W. (1979). "A 3D hypoelastic concrete constitutive relationship." J. Engrg. Mech., ASCE, 105(4): 623–41.

EPRI (1990). Electric Power Research Institute, Manual on Estimating Soil Properties for Foundation Design. Elastic deforming. Ithaca, NY: Cornell University, pp. 1–26.

FHWA (2004). U.S. Department of Transportation, Federal Highway Administration, "Recommendations for Seismic Performance Testing of Bridge Piers," 1st ed. (Draft), December. Mclean, Vermont.

Filiatrault, A., and Holleran, M. (2001). "Stress-strain behavior of reinforcing steel and concrete under seismic strain rates and low temperatures." Material Structure, 34(5): 235–239.

Foriero, A., St-Laurent, N., and Ladanyi, B. (2005). “Laterally loaded pile study in permafrost of Northern Quebec, Canada.” J. of Cold Regions Engineering, 19(3): 61–84.

Geodaq (2006). Geodaq INC300 series inclinometer data sheet. www.geodaq.com (March 2006).

Geodaq (2010). Geodaq Automated Instrumentation and Data Acquisition Services. http://www.geodaq.com/ (accessed May 5, 2010).

Google. Google Maps. http://maps.google.com/ (accessed July 3, 2010).

Google Earth (2009). Version 4.1.x. Google Inc.

Haynes, F. D., and Karalius, J. A. (1977). “Effect of temperature on the strength of frozen silt.” CRREL Report 77-3, Cold Regions Research and Engineering Laboratory. Hanover, New Hampshire.

Horazdovsky, J. E. (2010). “Seasonal effects of frozen soil on the stiffness of bridge piles.” Master’s thesis, University of Alaska Fairbanks, Fairbanks, Alaska.

Iwan, W. D. (1967). “On a class of models for the yielding behavior of continuous and composite systems.” J. Appl. Mech., ASME, 34: 612–617.

Juirnarongrit, T., and Ashford, S. A., (2005). “Effect of pile diameter on the modulus of subgrade reaction.” Structural Systems Research Project, Report No. SSRR-2001/22, University of California, Department of Structural Engineering, San Diego.

Kinemetrics, Inc. (2010). Products. <www.kinemetrics.com>

Kondner, R. L. (1963). “Hyperbolic stress-strain response: Cohesive soils.” Journal of the Soil Mechanics and Foundations Division, 89(SM1), 115–143.

Kramer, S. L. (1996). “Geotechnical earthquake engineering.” *Stress-Strain Behavior of Cyclicality Loaded Soils.* Upper Saddle River, NJ: Prentice-Hall., pp. 232–233.

Kulhawy, F. and Mayne, P. (1990). "Manual on estimating soil properties for foundation design." Report No. EL-6800 Electric Power Research Institute,. Cornell Univ.Ithaca, N.Y.,

LeBlanc, A. M., Fortier, R., Allard, M., Cosma, C., and Buteau, S. (2004). “Seismic cone penetration test and seismic tomography in permafrost.” Can. Geotech. J., 41: 769–813.

Lee, G. C., Shih, T. S., and Chang, K. C. (1988a). “Mechanical properties of concrete at low temperature.” J. Cold Reg. Eng., 2(1): 13–24.

Lee, G. C., Shih, T. S., and Chang, K. C. (1988b). “Mechanical properties of high-strength concrete at low temperature.” J. Cold Reg. Eng., 2(4): 169–178.

Lu J., Yang Z., and Elgamal A. (2006). “Openseespl three-dimensional lateral pile-ground interaction version 1.00 user's manual.” Report No. SSRP-06/03, Department of Structural Engineering, University of California, San Diego.

Mander, J. B., Priestley, M. J. N., and Park, R. (1988a). "Theoretical stress-strain model for confined concrete." Jour. Struct. Div., ASCE, 114: 1804–1826.

Mander, J. B., Priestley, M. J. N., and Park, R. (1988b). "Observed stress-strain behavior of confined concrete." Jour. Struct. Div., ASCE, 114: 1827–1849.

Matlock, H. (1970). "Correlations of design of laterally loaded piles in soft clay." Proc., Offshore Technology Conf., Houston, Vol. 1, 577–594.

Mazzoni, S., McKenna, F., and Fenves, G. L. (2006). Open System for Earthquake Engineering Simulation User Manual. Pacific Earthquake Engineering Research Center, University of California, Berkeley. <http://opensees.berkeley.edu>

Miranda, R. (2007). "Frozen ground effects on the dynamic response of a 14-story office building in Anchorage, Alaska." Civil Engineering Graduate Project, University of Alaska Anchorage, Anchorage, Alaska.

Mohamed, H. H. (2006). "Axial stress–strain relationship for FRP confined circular and rectangular concrete columns." Cement & Concrete Composites, 28: 938–948.

Montejo, L. A., Sloan, J. E., Kowalsky, M. J., and Hassan, T. (2008). "Cyclic response of reinforced concrete members at low temperatures." Journal of Cold Regions Engineering, ASCE, 22: 79–102.

Mroz, Z. (1967). "On the description of anisotropic work hardening." Journal of Mechanics and Physics of Solids, 15: 163–175.

Nicholson, F. H., and Granberg, H. B. (1973). "Permafrost and snowcover relations near Schefferville." In: Permafrost, 2nd International Conference North American Contribution Washington, D.C.: National Academy of Sciences, pp. 151–158.

Nidowicz, B. (1981). "Consolidation and shear strength characteristics of Fairbanks silt." Master's thesis, University of Alaska Fairbanks, Fairbanks, Alaska.

Palm, W. J. (2007). *Mechanical Vibration*. Hoboken, NJ: John Wiley & Sons, Inc.

Parra, E. (1996). "Numerical modeling of liquefaction and lateral ground deformation including cyclic mobility and dilation response in soil systems," Ph.D thesis, Department of Civil Engineering, Rensselaer Polytechnic Institute, Troy, New York.

Peeters, B., and De Roeck, G. (2001). "One-year monitoring of the Z24-bridge: Environmental effects versus damage events." Earthquake Eng. Struct. Dyn., 30: 149–171.

Prevost, J. H. (1985). "A simple plasticity theory for frictional cohesionless soils." Int. J. Soil Dynamics and Earthquake Engineering, 4(1): 9–17.

Priestley, M. J. N., Seible, F., and Calvi, G. M. (1996). *Seismic Design and Retrofit of Bridges*. New York: John Wiley & Sons.

Priestley, M. J. N., Calvi, G. M., and Kawalsky, M. J. (2007). *Displacement-Based Seismic Design of Structures*. IUSS PRESS, Pavia, Italy.

Reese, L. C. (1997). “Analysis of laterally loaded piles in weak rock.” Journal of Geotechnical and Geoenvironmental Engineering, ASCE, 123(11): 1010–1017.

Reese, L. C., and Welch, M. (1975). “Lateral loading of deep foundations in stiff clay.” Journal of the Geotechnical Engineering Division, 101(GT7): 633–649.

Reese, L. C., Cox, W. R., and Koop, F. D. (1974). “Analysis of laterally loaded piles in sand.” 6th Annual Offshore Technology Conf., Houston, Texas.

Reese, L. C., Wang, S. T., Isenhower, W. M., and Arrellaga, J. A. (2004). Computer Program LPile Plus, version 5.0. Ensoft Inc., Austin, Texas.

Rowley, R. K., Watson, G. H., and Ladanyi, B. (1973). “Vertical and lateral pile load tests in permafrost.” Proc. of 2nd Int. Conference on Permafrost, Yakutsk, USSR, 712–721.

Seed, H. B., and Idriss, I. M. (1970). “Soil moduli and damping factors for dynamic response analysis.” Report EERC 70-10, University of California, Earthquake Engineering Research Center, Berkeley.

Sohn, H., Dzwonczyk, M., Straser, E., Kiremidjian, A., and Law, K. (1999). “An experimental study of temperature effect on modal parameters of the Alamosa Canyon Bridge.” Earthquake Eng. Struct. Dyn., 28: 879–897.

Sritharan, S., White, D. J., and Suleiman, M. T. (2004). “Bridge column foundation-soil interaction under earthquake loads in frozen conditions.” 13th World Conference on Earthquake Engineering, Paper No. 3425. Vancouver, B.C., Canada, August 1–6, 2004.

Sritharan, S., Suleiman, M. T., and White, D. J. (2007). “Effects of seasonal freezing on bridge column-foundation-soil interaction and their implications.” Earthquake Spectra, 23(1): 199–222.

Stevens, H. W. (1973). “Viscoelastic properties of frozen soils under vibratory loads.” North American Contribution to the Second International Conf. on Permafrost, 400–409. Yakutsk, U.S.S.R.

Suleiman, M. T., Sritharan, S., and White, D. J. (2006). “Cyclic lateral load response of bridge column-foundation-soil systems in freezing conditions.” Journal of Structural Engineering, 132(11): 1745–1754.

Tsytovich, N. A. (1975). *The Mechanics of Frozen Ground*. McGraw-Hill, Inc., New York.

University of Washington (2008). Modified Berggren Formula for Estimating Freeze/Thaw Depth. < http://training.ce.washington.edu/>

USACE (1987). U.S. Army Corps of Engineers, Departments of the Army and the Air Force Technical Manual. “Concrete Floor Slabs on Grade Subjected to Heavy Loads.” TM5-809-12 4-2.

Vesic, A. S. (1961). “Beams on elastic subgrade and the Winkler hypothesis.” Proceedings of the 5th International Conference on Soil Mechanics and Foundation Engineering, Vol. 1, Paris, 845–850.

Vinson, T. S. (1978). “Response of frozen ground to dynamic loading.” In *Geotechnical Engineering for Cold Regions*. Edited by O. B. Andersland and D. M. Anderson. New York: McGraw-Hill Book Company, Chapt. 8, pp. 405–458.

Watson, G. H., Slusarchuk, W. A., and Rowley, R. K., (1973). “Determination of some frozen and thawed properties of permafrost soils.” Can. Geotech. J., 10 (4): 592–606.

Weaver, J. S., and Morgenster, N. R. (1981). “Pile design in permafrost.” Canadian Geotech. J., 18: 357–370.

Wilson, D. W. (1998). “Soil-pile-superstructure interaction in liquefying sand and soft clay.” Ph.D. dissertation, Univ. of California, Davis.

Xiong, F., and Yang, Z. (2008). “Effects of seasonally frozen soil on the seismic behavior of a bridge bent-foundation-soil system.” Cold Regions Science and Technology. In press.

Xu, G. (2009). “Effects of frozen soils on site response and lateral behavior of concrete-filled steel pipe pile.” Master’s thesis, University of Alaska Anchorage, Anchorage, Alaska.

Yang, Z. (2000). “Numerical modeling of earthquake site response including dilation and liquefaction.” PhD thesis, Department of Civil Engineering and Engineering Mechanics, Columbia University, New York.

Yang, Z., and Elgamal, A. (2002). “Influence of permeability on liquefaction-induced shear deformation.” Journal of Engineering Mechanics, 128(7): 720–729.

Yang, Z., and Jeremic, B. (2005). “Study of soil layering effects on lateral loading behavior of piles.” J. Geotech. Geoenviron. Eng., 131(6): 762–770.

Yang, Z., Elgamal, A., and Parra, E. (2003). “A computational model for cyclic mobility and associated shear deformation.” Journal of Geotechnical and Geoenvironmental Engineering, 129(12): 1119–1127.

Yang, Z., Dutta, U., Liu, H., Pratt, R., Marx, E., Biswas, N., and Zhu, D. (2005). “Strong-motion instrumentation and structural health monitoring of the port access bridge, Anchorage, Alaska.” Proc., 2005 Joint ASME/ASCE/SES Conference on Mechanics and Materials (CD-Rom), Baton Rouge, Louisiana, USA, June 1–3, 2005.

Yang, Z., Dutta, U., Xiong, F., Zhu, D., Marx, E., and Biswas, N. (2007a). “Seasonal frost effects on the soil-foundation-structure interaction system.” ASCE Journal of Cold Regions Engineering, 21(4): 108–120.

Yang, Z., Dutta, U., Xiong, F., Biswas, N., and Benz, H. (2007b). “Seasonal frost effects on the dynamic behavior of a twenty-story office building.” International Journal of Cold Regions Science and Engineering, 51(1): 76–84.

Yang, Z., Xiong, F., Xu, G., Hulsey, J. L., and Marx, E. (2008). “Seasonal freezing effects on the lateral behavior of steel pipe piles.” 14th World Conference on Earthquake Engineering. Beijing, China.

Yang, Z., Li, Q., Xu, G., and Hulsey, J. L. (2010). “Seasonal freezing effects on the dynamic behavior of highway bridges.” Proc., GeoShanghai 2010, Shanghai, China.

Zhu, Y., and Carbee, D. L. (1984). “Uniaxial compressive strength of frozen silt under constant deformation rates.” Cold Regions Science and Technology, 9: 3–15.

Zhu, Y., and Carbee, D. L. (1987). “Creep and Strength Behavior of Frozen Silt in Uniaxial Compression.” CRREL Report 87-10. Hanover, NH: Cold Regions Research and Engineering Laboratory.

Appendices

Appendix A

The log of boring 59 is shown in Figure A.0.1 (DOWL Engineers 2005).

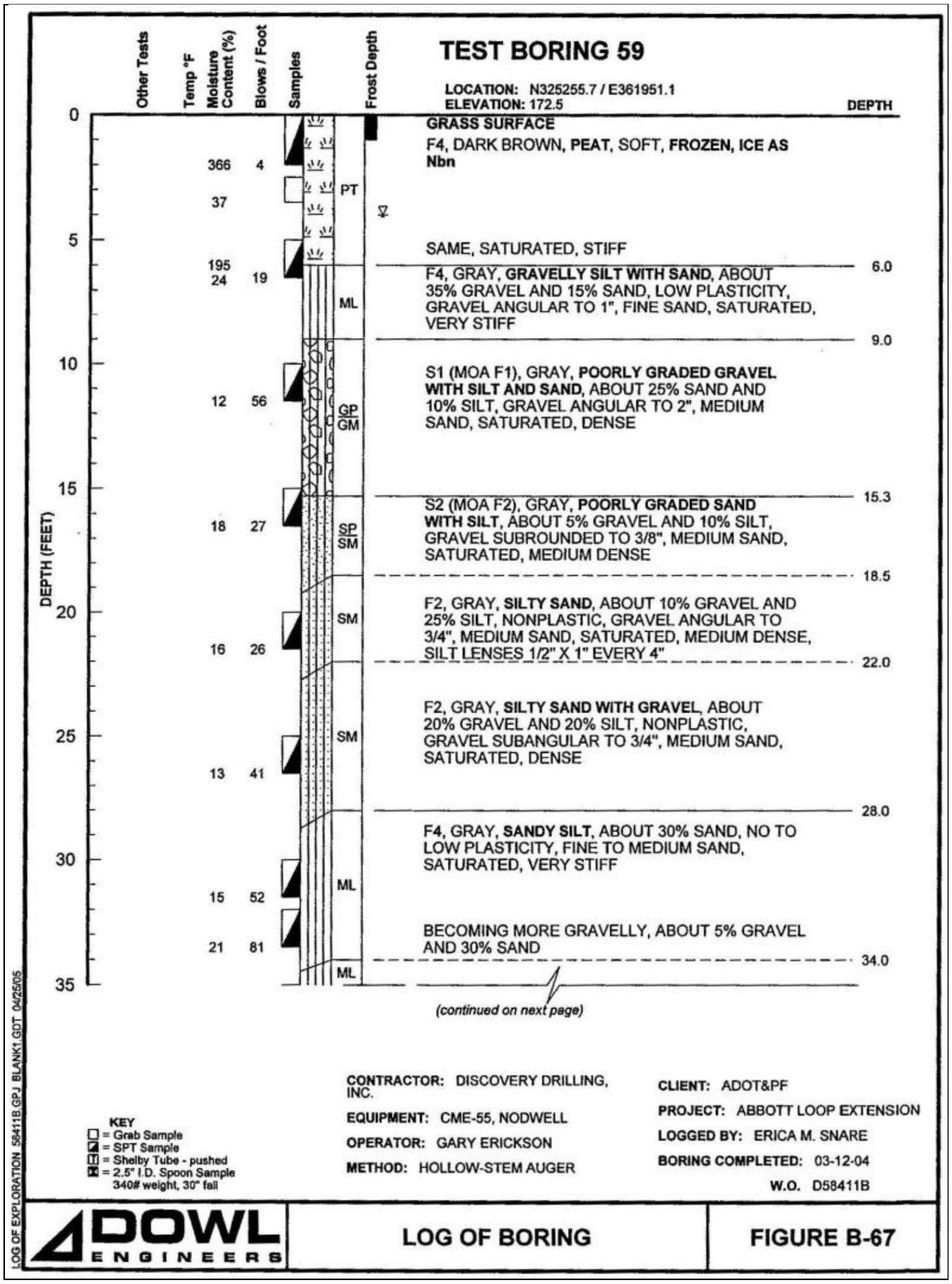

TEST BORING 59

LOCATION: N325255.7 / E361951.1
ELEVATION: 172.5

	DEPTH
GRASS SURFACE F4, DARK BROWN, **PEAT**, SOFT, **FROZEN, ICE AS Nbn** SAME, SATURATED, STIFF	6.0
F4, GRAY, **GRAVELLY SILT WITH SAND**, ABOUT 35% GRAVEL AND 15% SAND, LOW PLASTICITY, GRAVEL ANGULAR TO 1", FINE SAND, SATURATED, VERY STIFF	9.0
S1 (MOA F1), GRAY, **POORLY GRADED GRAVEL WITH SILT AND SAND**, ABOUT 25% SAND AND 10% SILT, GRAVEL ANGULAR TO 2", MEDIUM SAND, SATURATED, DENSE	15.3
S2 (MOA F2), GRAY, **POORLY GRADED SAND WITH SILT**, ABOUT 5% GRAVEL AND 10% SILT, GRAVEL SUBROUNDED TO 3/8", MEDIUM SAND, SATURATED, MEDIUM DENSE	18.5
F2, GRAY, **SILTY SAND**, ABOUT 10% GRAVEL AND 25% SILT, NONPLASTIC, GRAVEL ANGULAR TO 3/4", MEDIUM SAND, SATURATED, MEDIUM DENSE, SILT LENSES 1/2" X 1" EVERY 4"	22.0
F2, GRAY, **SILTY SAND WITH GRAVEL**, ABOUT 20% GRAVEL AND 20% SILT, NONPLASTIC, GRAVEL SUBANGULAR TO 3/4", MEDIUM SAND, SATURATED, DENSE	28.0
F4, GRAY, **SANDY SILT**, ABOUT 30% SAND, NO TO LOW PLASTICITY, FINE TO MEDIUM SAND, SATURATED, VERY STIFF BECOMING MORE GRAVELLY, ABOUT 5% GRAVEL AND 30% SAND	34.0

(continued on next page)

KEY
☐ = Grab Sample
◪ = SPT Sample
◫ = Shelby Tube - pushed
▣ = 2.5" I.D. Spoon Sample
340# weight, 30" fall

CONTRACTOR: DISCOVERY DRILLING, INC.
EQUIPMENT: CME-55, NODWELL
OPERATOR: GARY ERICKSON
METHOD: HOLLOW-STEM AUGER

CLIENT: ADOT&PF
PROJECT: ABBOTT LOOP EXTENSION
LOGGED BY: ERICA M. SNARE
BORING COMPLETED: 03-12-04
W.O. D58411B

LOG OF BORING

FIGURE B-67

(a)

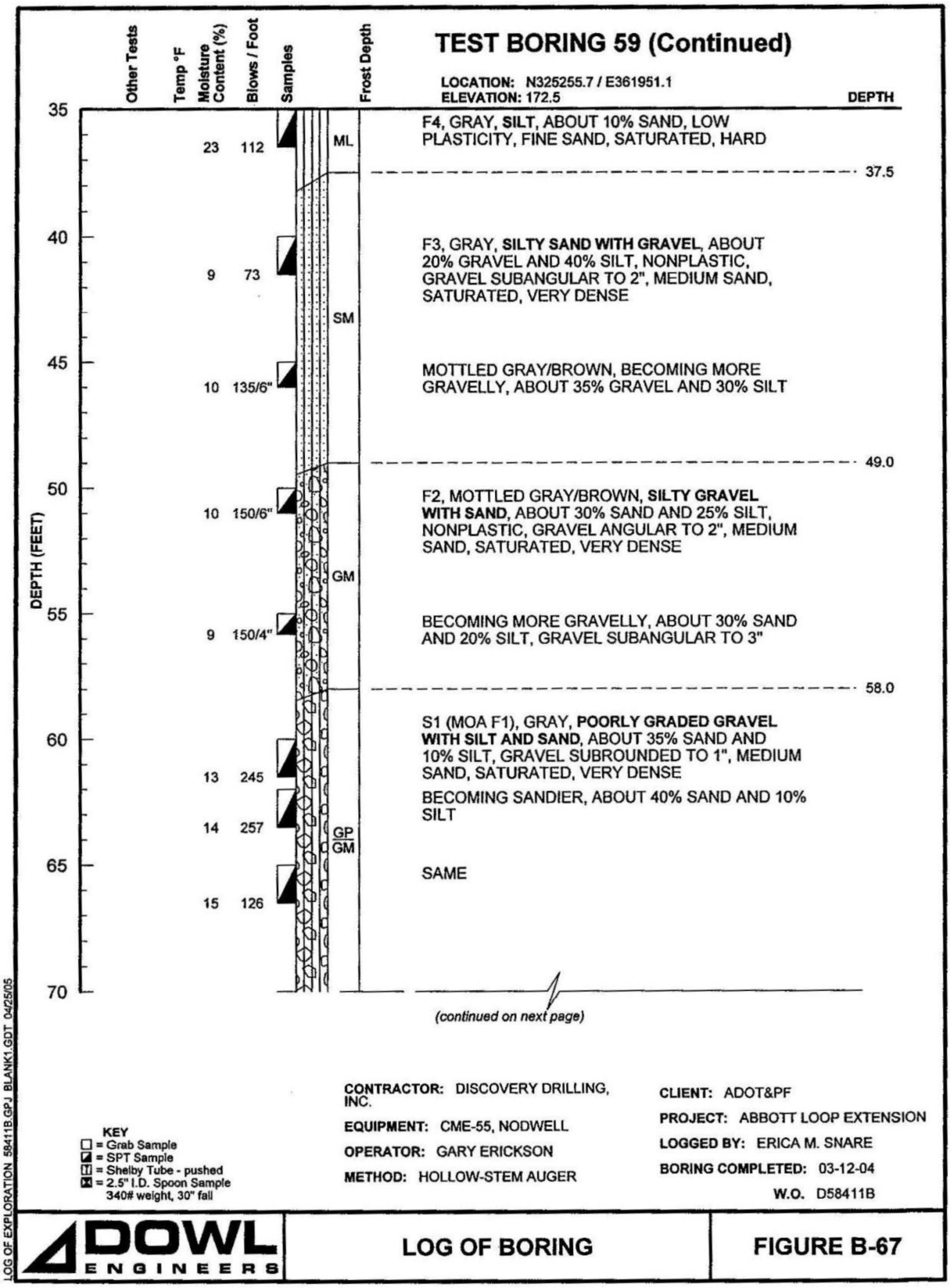

TEST BORING 59 (Continued)

LOCATION: N325255.7 / E361951.1
ELEVATION: 172.5

Other Tests	Temp °F	Moisture Content (%)	Blows / Foot	Samples	Frost Depth
		23	112		
		9	73		
		10	135/6"		
		10	150/6"		
		9	150/4"		
		13	245		
		14	257		
		15	126		

DEPTH

ML — F4, GRAY, **SILT**, ABOUT 10% SAND, LOW PLASTICITY, FINE SAND, SATURATED, HARD

37.5

SM — F3, GRAY, **SILTY SAND WITH GRAVEL**, ABOUT 20% GRAVEL AND 40% SILT, NONPLASTIC, GRAVEL SUBANGULAR TO 2", MEDIUM SAND, SATURATED, VERY DENSE

MOTTLED GRAY/BROWN, BECOMING MORE GRAVELLY, ABOUT 35% GRAVEL AND 30% SILT

49.0

GM — F2, MOTTLED GRAY/BROWN, **SILTY GRAVEL WITH SAND**, ABOUT 30% SAND AND 25% SILT, NONPLASTIC, GRAVEL ANGULAR TO 2", MEDIUM SAND, SATURATED, VERY DENSE

BECOMING MORE GRAVELLY, ABOUT 30% SAND AND 20% SILT, GRAVEL SUBANGULAR TO 3"

58.0

GP/GM — S1 (MOA F1), GRAY, **POORLY GRADED GRAVEL WITH SILT AND SAND**, ABOUT 35% SAND AND 10% SILT, GRAVEL SUBROUNDED TO 1", MEDIUM SAND, SATURATED, VERY DENSE

BECOMING SANDIER, ABOUT 40% SAND AND 10% SILT

SAME

(continued on next page)

KEY
☐ = Grab Sample
◪ = SPT Sample
◫ = Shelby Tube - pushed
☒ = 2.5" I.D. Spoon Sample
340# weight, 30" fall

CONTRACTOR: DISCOVERY DRILLING, INC.
EQUIPMENT: CME-55, NODWELL
OPERATOR: GARY ERICKSON
METHOD: HOLLOW-STEM AUGER

CLIENT: ADOT&PF
PROJECT: ABBOTT LOOP EXTENSION
LOGGED BY: ERICA M. SNARE
BORING COMPLETED: 03-12-04
W.O. D58411B

DOWL ENGINEERS

LOG OF BORING

FIGURE B-67

LOG OF EXPLORATION 58411B.GPJ BLANK1.GDT 04/25/05

(b)

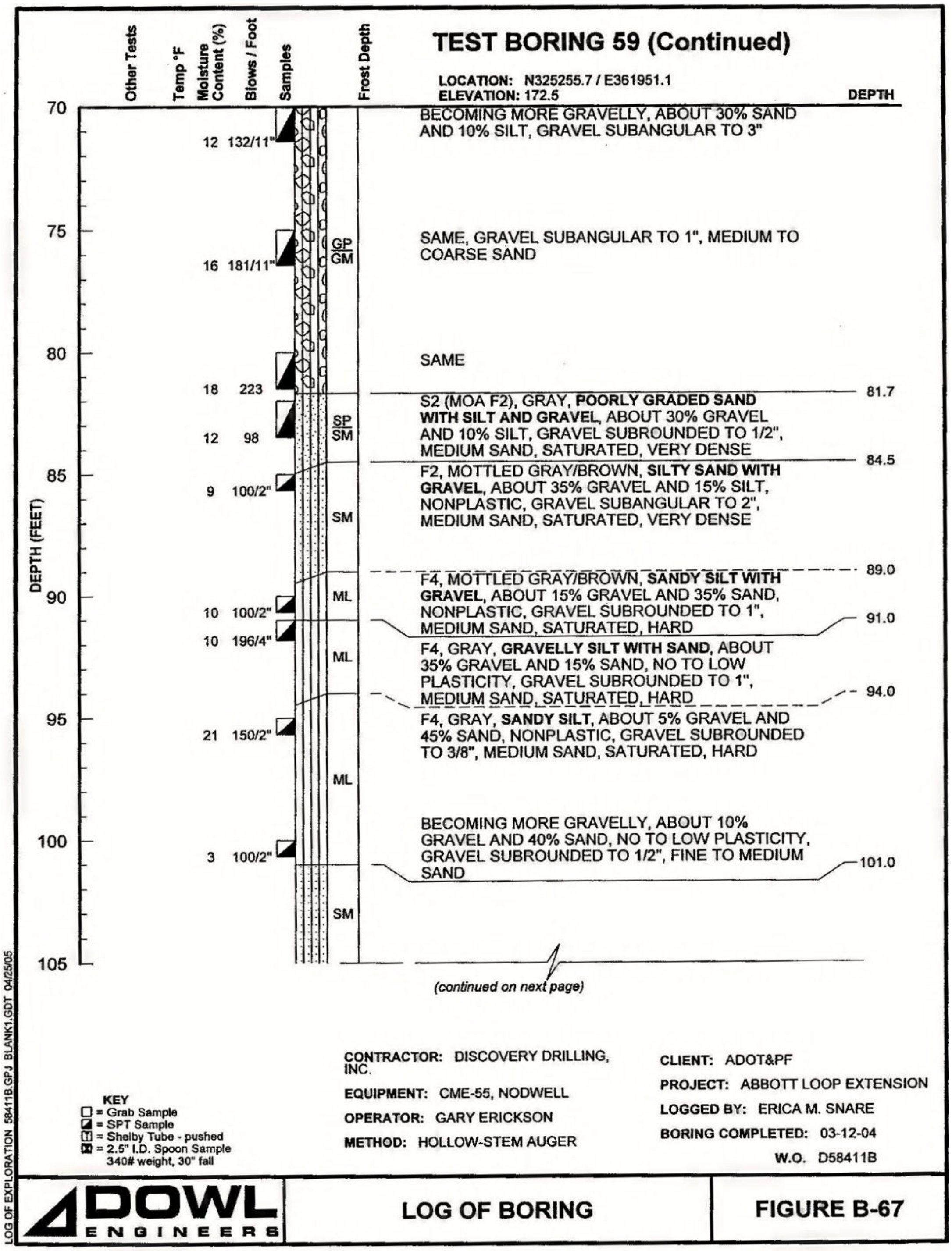

TEST BORING 59 (Continued)

LOCATION: N325255.7 / E361951.1
ELEVATION: 172.5

BECOMING MORE GRAVELLY, ABOUT 30% SAND AND 10% SILT, GRAVEL SUBANGULAR TO 3"

SAME, GRAVEL SUBANGULAR TO 1", MEDIUM TO COARSE SAND

SAME

S2 (MOA F2), GRAY, **POORLY GRADED SAND WITH SILT AND GRAVEL**, ABOUT 30% GRAVEL AND 10% SILT, GRAVEL SUBROUNDED TO 1/2", MEDIUM SAND, SATURATED, VERY DENSE

F2, MOTTLED GRAY/BROWN, **SILTY SAND WITH GRAVEL**, ABOUT 35% GRAVEL AND 15% SILT, NONPLASTIC, GRAVEL SUBANGULAR TO 2", MEDIUM SAND, SATURATED, VERY DENSE

F4, MOTTLED GRAY/BROWN, **SANDY SILT WITH GRAVEL**, ABOUT 15% GRAVEL AND 35% SAND, NONPLASTIC, GRAVEL SUBROUNDED TO 1", MEDIUM SAND, SATURATED, HARD

F4, GRAY, **GRAVELLY SILT WITH SAND**, ABOUT 35% GRAVEL AND 15% SAND, NO TO LOW PLASTICITY, GRAVEL SUBROUNDED TO 1", MEDIUM SAND, SATURATED, HARD

F4, GRAY, **SANDY SILT**, ABOUT 5% GRAVEL AND 45% SAND, NONPLASTIC, GRAVEL SUBROUNDED TO 3/8", MEDIUM SAND, SATURATED, HARD

BECOMING MORE GRAVELLY, ABOUT 10% GRAVEL AND 40% SAND, NO TO LOW PLASTICITY, GRAVEL SUBROUNDED TO 1/2", FINE TO MEDIUM SAND

(continued on next page)

KEY
☐ = Grab Sample
◪ = SPT Sample
◫ = Shelby Tube - pushed
☒ = 2.5" I.D. Spoon Sample 340# weight, 30" fall

CONTRACTOR: DISCOVERY DRILLING, INC.
EQUIPMENT: CME-55, NODWELL
OPERATOR: GARY ERICKSON
METHOD: HOLLOW-STEM AUGER

CLIENT: ADOT&PF
PROJECT: ABBOTT LOOP EXTENSION
LOGGED BY: ERICA M. SNARE
BORING COMPLETED: 03-12-04
W.O. D58411B

LOG OF BORING

FIGURE B-67

(c)

Figure A.0.1: Log of boring (DOWL Engineers 2005)

Appendix B

The downhole shear wave analysis for Test Boring 59 is shown in Figure B.0.2 (DOWL Engineers 2005).

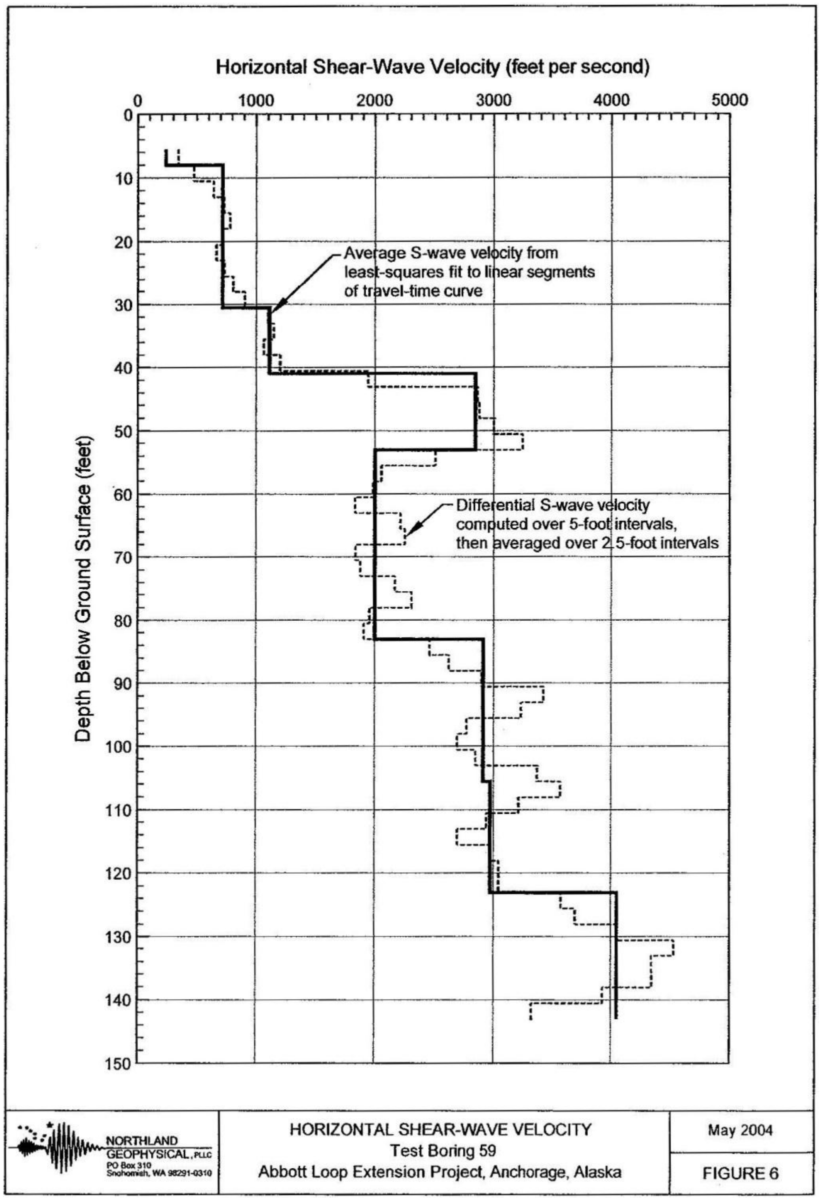

Figure B.0.2: Profile of shear-wave velocity from 6 feet to 150 feet below ground surface (DOWL Engineers 2005).